

POLITECNICO DI TORINO

MASTER's Degree in BIOMEDICAL ENGINEERING



MASTER's Degree Thesis

Evaluation of the effect of curvature on a fibre-optic sensor for temperature monitoring during mini-invasive body contouring treatments

Supervisors

Prof. Guido PERRONE

Prof. Gianni COPPA

Prof. Alberto VALLAN

Candidate

Elena DE SANTIS

July 2023

*To my grandmother,
I hope that one day
I can be strong
and kind like her.*

Summary

Obesity has been recognised as one of the main factors responsible for increasing the risk of various potentially deadly diseases. Obesity can be cured, but regardless of treatment, rapid weight loss often results in certain irregularities in body contours.

These imperfections can be corrected by body contouring techniques. Currently, the laser lipolysis technique has become the elective approach for this type of treatment, as it guarantees good results with reduced recovery times and risks.

In laser lipolysis, light is delivered using an optical fibre inserted through the cannula under the skin. During the operation, the physician must move the cannula under the skin to properly heat the entire target area. This movement is crucial: if the physician moves the cannula too slowly, it may cause an overaccumulation of energy and burn the tissues; otherwise, if the cannula is moved too fast, the treatment may be ineffective.

This thesis is part of a larger project aimed at developing a laser applicator for thermal treatments that integrates a temperature sensor system to optimize the outcomes and help reducing the risk of burns. Fibre optic sensors (FOSs) are the best solution for this application because they do not produce artefacts when exposed to the laser beam; moreover, they are biocompatible, and their small size minimizes the invasive impact. FOSs, however, suffer from cross-sensitivity between temperature and strain. This is particularly detrimental for the considered application because the movement of the cannula during lipolysis treatment causes an error in FOS temperature estimation.

The aim of this thesis is to design an all-fibre sensor configuration to discriminate the strain and temperature effects, devise a compensation algorithm and validate its feasibility through experiments. The selected configuration is based on a combination of Fibre Bragg Grating (FBG) sensors positioned to produce different strain readings depending on their orientation but a common temperature reading.

For an initial analysis, the sensitivity to a two-dimensional strain was assessed. For this purpose, an applicator embedding two FBGs respectively positioned on

the top and on the bottom of a miniaturised cantilever was realised. In order to accurately characterise the sensor to strain, a set of grooves with constant curvature and custom design was fabricated using a 3D printer. A specific code was written in Matlab to analyse the data and build the relationship between FBG wavelength shift and the applicator curvature. Subsequently, the sensor was characterised in a climatic chamber to assess its behaviour with respect to temperature. The relationships obtained from the two characterisations were then used in a Matlab code, which allows the sensor to be used to measure temperature even when bent.

The validity demonstrated by preliminary experimental tests for the proposed solution made it possible to extend the analysis to the three-dimensional case. For this purpose, the applicator design was modified to incorporate four FBGs and to simulate the appearance of a laser lipolysis cannula. Once the prototype was built, the new sensor was subjected to experimental tests to verify the correct discrimination of direction changes in three-dimensional space. Finally, a Matlab code was developed to estimate the sensor direction of movement.

Through an accurate characterisation of the sensor, it will be possible to obtain a more detailed evaluation of the sensor motion.

Acknowledgements

I would like to thank Professor Guido Perrone for giving me the opportunity to work on this project, for always supporting me and helping me throughout this journey. I also want to express my gratitude to Professor Alberto Vallan for his availability and all his valuable advice. I would like to thank Professor Gianni Coppa for giving me the opportunity to be part of this project and for the attention he has given me over these months.

I am immensely grateful to Aurora, Matteo, and Chiara for their endless assistance, availability, and above all, for making this journey so enjoyable.

I want to thank all my friends in Turin who have gone through a similar path and have made this experience full of wonderful memories. I sincerely thank my lifelong friends who have always stood by me despite the distance. In particular, I am grateful to my friends from CNT, with whom I have shared unforgettable moments and who have stood by me even in difficult situations. A simple thank you is not enough for them. They will always be like a second family to me.

The biggest thanks go to my family. To my parents, I appreciate all the love and infinite patience they have shown me. I still wonder how they managed to tolerate me even during the most stressful moments. And to my siblings, I am grateful for always being there for me, for their constant advice and support. No one has brothers like mine.

Table of Contents

List of Tables	XII
List of Figures	XIV
Acronyms	XIX
1 Introduction	1
2 Body contouring techniques	4
2.1 Invasive techniques	4
2.1.1 Liposuction	4
2.1.2 Laser Lipolysis	5
2.2 Non-invasive techniques	9
2.2.1 Cryolipolysis	9
2.2.2 Hyperthermic Laser Lipolysis	10
2.2.3 Radio Frequency	11
2.2.4 Focused Ultrasound	12
2.2.5 High-Intensity Focused Electromagnetic Technology	14
3 Temperature monitoring	15
3.1 Introduction	15
3.2 Non-invasive thermometry	16

3.2.1	CT-based thermometry	16
3.2.2	MRI-based thermometry	16
3.2.3	Ultrasound-based thermometry	17
3.3	Invasive thermometry	17
3.3.1	Thermocouples	18
3.3.2	Thermoresistances	18
3.3.3	Fibre Optic Sensors	19
4	Introduction to the instrumentation	24
4.1	Optical Fibres	24
4.1.1	Structure	24
4.1.2	Physical principle	25
4.1.3	Optical fibre types and modes	26
4.2	Fibre Bragg Gratings	28
4.2.1	Physical principle	28
4.2.2	Manufacturing methods	29
4.2.3	Types of FBGs	31
4.3	Optical Interrogators	32
4.3.1	MICRON OPTICS HYPERION si155	34
4.3.2	Matlab interface	35
4.4	3D printers	36
4.4.1	ANYCUBIC MEGA X	37
5	Separation of temperature and strain effects in FOSs	40
5.1	Seven-Core Fibre sensor for curvature and temperature measurements	40
5.2	Shape and temperature sensor based on Bragg Grating Waveguides	43
5.3	Temperature, bending and torsion separation with a triangular FBG sensors array	45

6	Strain and associated curvature detection with optical fibres	49
6.1	Characterisation of Bragg gratings with respect to strain	50
6.1.1	First characterization test	51
6.1.2	Construction of the calibration board	52
6.1.3	Characterisation with the calibration board	55
6.2	Characterisation of the sensor with respect to strain	60
6.2.1	Construction of the two-dimensional sensor	60
6.2.2	Setup and instrumentation	61
6.2.3	Results	62
6.2.4	Observations	63
6.3	Use of the sensor for two-dimensional deformation measurements . .	66
6.3.1	Setup and instrumentation	66
6.3.2	Results	66
6.3.3	Observations	67
7	Temperature detection with optical fibres	69
7.1	Characterisation of Bragg gratings with respect to temperature . .	69
7.1.1	Setup and instrumentation	70
7.1.2	Results	72
7.1.3	Observations	77
7.2	Characterisation of the sensor with respect to temperature	78
7.2.1	Setup and instrumentation	78
7.2.2	Results	80
7.2.3	Observations	83
7.3	Temperature measurement when the sensor is bent	83
7.3.1	Separation of temperature and strain	84
7.3.2	Setup and instrumentation	85
7.3.3	Results	87

7.3.4	Observations	89
8	The first steps towards three-dimensional strain detection	91
8.1	Sensor prototyping	91
8.1.1	First attempt: fixing only the ends of the gratings to the substrate	91
8.1.2	Second attempt: embedding the gratings in the silicone substrate	94
8.1.3	Third attempt: attachment of the gratings to a substrate along their entire length	95
8.2	Sensor sensitivity evaluation	96
8.2.1	Setup and instrumentation	96
8.2.2	Results and observations	97
8.3	Detection of sensor movement direction	98
8.3.1	Observations	98
8.4	Graphic representation of sensor movement	99
9	Conclusions	101
	Bibliography	104

List of Tables

2.1	Laser lipolysis device [10].	7
2.2	Effect of temperature on tissues [12].	8
6.1	Radius of the curves in the calibration board.	53
6.2	Strain associated with the curvatures in the model.	57
6.3	Average wavelength of the two FBGs for each trial.	57
6.4	Parameters of the FBG A calibration line.	58
6.5	Parameters of the FBG B calibration line.	59
6.6	Parameters of the FBG A calibration line.	63
6.7	Parameters of the FBG B calibration line.	64
6.8	Estimation of the bending radius with the grating A.	67
6.9	Estimation of the bending radius with the grating B.	67
7.1	Set and real temperature during the trial.	73
7.2	Set temperature and average Bragg wavelength in the seven steps.	73
7.3	Parameters of the FBG B calibration line.	74
7.4	Set and real temperature during the trial.	75
7.5	Set temperature and average Bragg wavelength in the seven steps.	76
7.6	Parameters of the FBG A calibration line.	76
7.7	Set and real temperature during the trial.	80
7.8	Set temperature and average Bragg wavelengths in the six steps.	81

7.9	Parameters of the FBG A calibration line.	82
7.10	Parameters of the FBG B calibration line.	83
7.11	Estimation errors.	89
8.1	The average wavelength values assumed by the sensor gratings when it is bent.	97
8.2	The average wavelength values assumed by the sensor gratings when it is bent.	98

List of Figures

1.1	Number of deaths worldwide by risk factor,2019 [5].	2
2.1	Laser lipolysis in the lateral abdominal region with evidenced the guide light from the microcannula tip [9].	6
2.2	Optical absorption curves of fat and water [9].	7
2.3	Skin contraction effect. (A) Before and (B) at 6 month follow-up [8].	9
2.4	Various cannulae used for (A) lipos aspiration, (B) liposculpture and (C) laser lipolysis [8].	9
2.5	Fat reduction of the left flank after 3 months following a single treatment [14].	11
2.6	Thermage CPT (Solta Medical,Hayward, CA, USA) [15].	12
2.7	Ultrasounds used to ablate adipose tissue [16].	13
3.1	(a) <i>extrinsic</i> and (b) <i>intrinsic</i> fibre optic sensor [19].	19
3.2	(A) Exponential decay of phosphor sensor, (B) Decay time, τ , as a function of temperature [17].	21
3.3	Sensors based on Fabry-Perot interferometry [21].	22
3.4	Working principle of FBG sensors [21].	23
4.1	Fibre optic structure [22].	25
4.2	The Snell's law [23].	26
4.3	Representation of the acceptance angle, 2θ [24].	26
4.4	Examples of single mode and multimode fibres [24].	27

4.5	Some cross-sections of fibres: step-index, graded-index and multi-core [25].	28
4.6	Point-by-point manufacturing.	30
4.7	Phase mask manufacturing [27].	30
4.8	Interference lithography [28].	31
4.9	FBGs with different spatial periodicity.	32
4.10	FBGs with different refractive index profiles [29].	32
4.11	Schematic representation of a tunable laser optical interrogator [30].	34
4.12	MICRON OPTICS HYPERION si155.	34
4.13	ENLIGHT <i>Sensing Analysis Software</i> user interface.	35
4.14	Schematisation of the phases of the peak detection algorithm [31]. .	36
4.15	Anycubic Mega X 3D printer [33].	38
4.16	The main components of a 3D printer FDM [32].	39
5.1	SCF cross-section [34].	41
5.2	(a) Scheme of the sensor based on BGWs; (b) and (c) microscope images of its cross-section, highlighting the positioning of the three waveguides [35].	43
5.3	Scheme of the sensor structure according to the paper in Ref. [37]. .	45
5.4	(a) Distribution of the FBGs in the same cross-section; (b) The bending effect on one FBG in the sensor.	46
5.5	FBG sensor packaging diagram.	47
6.1	Diagram of a FBG sensor portion under pure bending; it also represents the <i>neutral layer</i> , O_1O_2 , that is the locus of the fibre points that are unstressed during its bending [38].	51
6.2	Strain characterization of the FBG using the grooves of a bottle. . .	52
6.3	Top view of the calibration board.	53
6.4	Side view of the calibration board.	54
6.5	The final design of the calibration board.	54
6.6	The realised calibration board in white PLA.	55

6.7	The setup used for the FBG characterization: A) optical fibre bent in one of the grooves, B)the calibration board.	56
6.8	The interpolation lines and the average wavelengths of the various trials for both FBGs.	58
6.9	Picture of the sensor built to study the case of a two-dimensional strain.	61
6.10	Picture of the sensor bent in one of the grooves of the calibration board.	61
6.11	Sensor bent to the right.	63
6.12	Sensor bent to the left.	63
6.13	The interpolation lines and the average wavelengths of the various trials for both FBGs.	64
7.1	PTC1/M Temperature-Controlled Breadboard by THORLABS. . .	70
7.2	The setup used for the trial.	71
7.3	The temperature profile set on the THORLABS breadboard in blue and the temperature profile measured with the reference sensor in red.	72
7.4	The Bragg wavelength profile of the grating B during the trial. . .	73
7.5	FBG B calibration line.	74
7.6	The linearity error of the FBG B calibration line.	74
7.7	The temperature profile set on the THORLABS breadboard in blue and the temperature profile measured with the reference sensor in red.	75
7.8	The Bragg wavelength profile of the grating A during the trial. . .	76
7.9	FBG A calibration line.	77
7.10	The linearity error of the FBG A calibration line.	77
7.11	The setup for the trial.	78
7.12	The temperature profile measured with the thermocouple. The stars indicate the start and end points of the six selected windows.	80

7.13	The Bragg wavelength variation for the grating A (red) and B (blue) during the test. The stars indicate the start and end points of the six selected windows.	81
7.14	The temperature profile measured with the thermocouple (black), with the grating A (red) and the gratings B (blue).	82
7.15	The linearity error of the FBG B (above) and of the FBG A (below) calibration lines.	82
7.16	A) the two-dimensional sensor; B) the thermocouple.	86
7.17	The temperature profile measured with the thermocouple.	87
7.18	The Bragg wavelength changes for the gratings B (above) and A (below).	88
7.19	Comparison of the temperature profile measured with the thermocouple (red) and with the two-dimensional sensor (blue).	88
7.20	The temperature estimation error of the two-dimensional sensor. . .	89
7.21	Comparison of the curvature profile measured with the two-dimensional sensor (red) with the real curvature (blue).	89
7.22	The curvature estimation error of the two-dimensional sensor. . . .	90
8.1	The gratings are bonded only at the ends.	92
8.2	The final sensor, coated with red heat-shrink tubing.	93
8.3	Effect of traction on one of the sensor gratings.	94
8.4	Effect of compression on one of the sensor gratings.	94
8.5	Silicone prototype.	95
8.6	The sensor obtained pasting the gratings to the substrate along their entire length.	96
8.7	setup for sensor curvature sensitivity evaluation tests.	96
8.8	Graphic representation of sensor movement in different instants of time.	99
8.9	The graph obtained by moving the sensor along the profile of a circle in the air.	100

Acronyms

BMI

Body Mass Index

WHO

World Health Organization

LL

Laser Lipolysis

LLLT

Low-Level Laser Therapy

RF

Radio Frequency

HIFU

High-Intensity Focused Ultrasound

HIFEM

High-Intensity Focused Electromagnetic Technology

HLL

Hyperthermic Laser Lipolysis

Nd:YAG

Neodymium-doped Yttrium Aluminium Garnet

FDA

US Food and Drug Administration

CT

Computed Tomography

MRI

Magnetic Resonance Imaging

PRF

Proton Resonance Frequency

FBG

Fibre Bragg Grating

FOS

Fibre Optic Sensor

DTS

Distributed Temperature Sensing

FDM

Fusion Deposition Modelling

PLA

Poly Lactic Acid

SMF

Single Mode Fibre

MCF

Multi-Core Fibre

SCF

Seven-Core Fibre

BGW

Bragg Grating Waveguide

Chapter 1

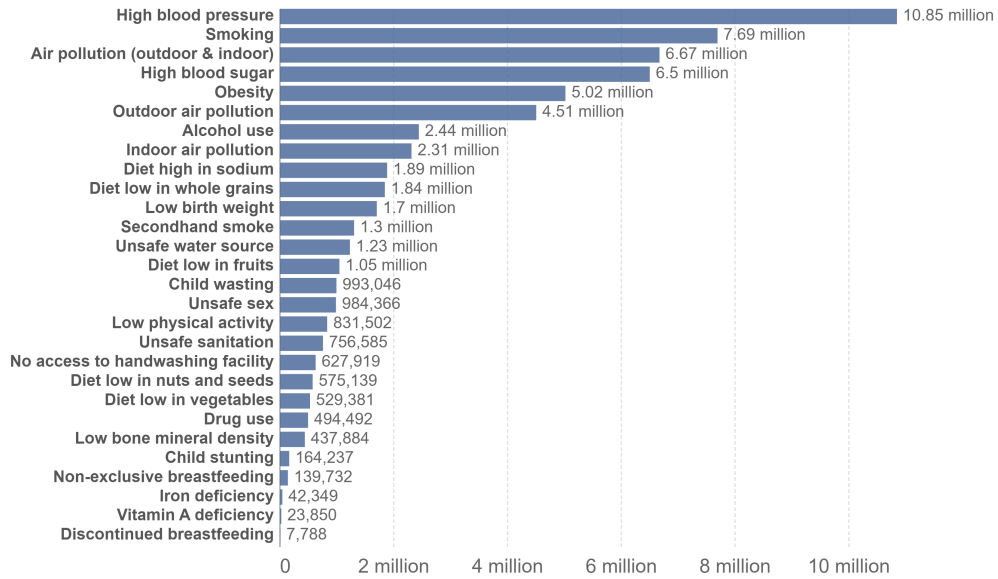
Introduction

Body contouring, or body sculpting, is an aesthetic medical treatment that aims to reshape the body to treat and resolve dysmorphia affecting the neck, chin, upper and lower limbs, back, belly and flanks [1]. Localized subcutaneous adipose tissue and tissue laxity are of growing concern among the population [2]. In addition to the cultural ideals of beauty and attractiveness, the increasing percentage of the obese population is also one of the reasons why the demand for body contouring is sharply rising.

Obesity is a disease characterized by a pathological accumulation of body fat generally caused by an imbalance between energy intake and expenditure. Obesity is determined using a measurement scheme called Body Mass Index (BMI), which calculates the percentage of body fat mass in relation to the individual's height. According to the World Health Organization (WHO), a person with a BMI from 25 to 29.99 is overweight, while a BMI of 30 or higher constitutes obesity.

Based on the latest estimate published by WHO more than 1 billion people worldwide are obese: 650 million adults, 340 million adolescents, and 39 million children [3]. The document also shows that in Europe 59% of adults and almost 1 in 3 children (29% of males and 27% of females) are overweight or suffer from obesity [4]. For this reason, obesity is now considered a real disease. Moreover, obesity can result in serious health issues like type II diabetes mellitus, hypertension, some cardiovascular disease and various types of cancer, so it can be considered as an indirect cause of death. Indeed, Fig. 1.1 shows the total annual number of deaths by risk factor, measured across all age groups and both sexes. According to the graph, obesity is one of the leading risk factors for death globally [5].

Obesity is curable starting with a proper combination of diet and exercise. To this, the physician may also decide to add specific pharmacological treatment to help



Source: IHME, Global Burden of Disease (2019)

OurWorldInData.org/causes-of-death • CC BY

Figure 1.1: Number of deaths worldwide by risk factor, 2019 [5].

the patient lose weight. In more severe cases, bariatric surgery, such as gastric bypass, can be used to radically reduce the stomach volume [6].

However, whatever therapy is followed, after rapid weight loss, it is rare for the body to assume a harmonious or toned shape. More often, instead, the body of an ex-obese still has some imperfections that leave the patient dissatisfied with his appearance [7]. The most common aesthetic defects in ex-obese people are the persistence of localised fat areas, poor muscle tone and the presence of areas of loose and redundant skin.

Anyway, when this occurs, the most effective and rapid way to restore the subject's normal silhouette is to resort to surgical body contouring techniques.

The body contouring techniques used in these cases are different and can be invasive, such as liposuction and Laser Lipolysis, or non-invasive, such as cryolipolysis, Hyperthermic Laser Lipolysis and techniques based on electromagnetic waves, radio waves and ultrasounds.

Among these techniques, laser lipolysis has attracted the greatest interest in recent times because, besides for effectively reducing the fat layer, it is able to promote skin contraction, giving a more toned appearance. Moreover, being a minimally invasive procedure, it is generally painless, with short recovery times and relatively low risks. The most common risk associated with the laser lipolysis technique is the

potential damage to surrounding tissues if the amount of heat released during the operation is not carefully controlled. Therefore, the development of a temperature control system could make this technique safer and more efficient.

The most promising solution is the use of fibre optic temperature sensors. Fibre Optic Sensors (FOSs) are flexible, small, and do not cause artefacts due to the absorption of laser light. These characteristics make them suitable for integration with the laser cannula and direct temperature monitoring at the source level. However, FOSs are also sensitive to strain. Therefore, the movement of the laser cannula within tissues can generate artefacts that can compromise the accuracy of the temperature reading.

The aim of this thesis is to evaluate and correct this error caused by strain. The proposed solution is based on the use of a combination of Fibre Bragg Grating (FBG) sensors which, due to their arrangement, detect the same temperature value but different strain values.

In this thesis, the case of a two-dimensional movement of the laser cannula has been studied first, where the sensor is subjected only to bending strain. To this end, a sensor has been fabricated by bonding two FBG sensors to a miniaturised cantilever. Subsequently, the sensor has been characterised with respect to temperature and bending strain. For the bending characterisation, a ‘calibration board’ with a customised design has been manufactured using the 3D printing technique. To conclude the two-dimensional motion analysis, tests have been carried out where the sensor has been used to simultaneously monitor temperature and curvature.

At this point in the thesis, the analysis of the case of motion in three-dimensional space has been initiated. Several attempts were made to prototype a sensor suitable for this purpose. The new sensor has a similar appearance to that of the laser cannula, but with a square cross-section, having a FBG sensor pasted on each face. Finally, a Matlab code was written and validated to obtain an initial graphical representation of the real-time sensor motion.

Chapter 2

Body contouring techniques

2.1 Invasive techniques

2.1.1 Liposuction

Liposuction is the most common cosmetic surgery, with 1,394,588 procedures performed worldwide in 2015 [2].

During a liposuction operation, a blunt-tipped cannula is inserted into the subcutaneous fat layer through a small incision. The cannula is connected to a suction system that, generating a negative pressure, allows safe and sterile aspiration of excess fat cells [8]. Simplicity and speed are the characteristics for which this technique has achieved great success. However, there are several complications related to liposuction. One of these is the long recovery time. Indeed, after the operation, compression garments and absorptive pads are applied to the wounds and the patient has to wear them for one month or more. Regardless, the patient cannot work for at least one week. Other complications are associated with some postoperative risks like infection, oedema, ecchymosis and haematoma. Consequently, different solutions that could reduce these risks have been evaluated. One of these is the introduction of the tumescent solution, described by Klein, which makes fat 'tumescent', facilitating its removal. This has proved to be an advantageous solution because it reduces the risk of bleeding and ecchymosis and speeds up post-operative recovery. Another modification was introduced by Zocchi in 1992. Zocchi applied ultrasound before aspiration to emulsify the fat. However, side effects such as damage to peripheral nerves and the appearance of large seromas discouraged the use of this technique [9].

Anyway, the greatest limitation of liposuction is the quasi-absence of skin retraction

which leads to contour irregularity after the procedure. This is why interest in laser lipolysis techniques, which instead promote skin retraction, is increasing.

2.1.2 Laser Lipolysis

The first study of Laser Lipolysis was conducted and published by Apfelberg in 1996. In it, Apfelberg described the results obtained using the Neodymium-doped Yttrium Aluminium Garnet (Nd:YAG) laser inside the liposuction cannula [9]. However, it was not approved by the FDA because there was still no concrete evidence of its benefits compared to liposuction.

In 2002, Goldman and others treated more than 1,700 patients with a 1,064 nm Nd:YAG pulsed laser. With this study, the team demonstrated the effect of laser energy on fat and surrounding tissues.

In the same years, Badin conducted a study to evaluate laser-induced histological changes. He found that the membranes of adipocytes were disrupted, blood vessels were coagulated and collagen was reorganized. Badin noted that there was a correlation between the histological changes he found and the clinical observations (decrease in local adiposity, ecchymoses and blood loss, improved skin tightening). For this reason, Badin decided to support Goldman's work. These two papers succeeded in demonstrating the less traumatic nature of the laser technique, due to the smaller size of the cannula, and its effect in improving skin retraction, due to the tissue response to the Nd:YAG system.

This allowed, in October 2006, the use of the laser 1,064 nm Nd:YAG to be approved by the US Food and Drug Administration as a laser lipolysis device [10].

The Technique

Laser lipolysis is a procedure performed in an outpatient clinic that does not require the patient to be hospitalised.

A 1 mm microcannula containing the laser optical fibre is inserted into the subcutaneous tissue under local anaesthesia. During the procedure, the microcannula is moved at an average speed of 5 cm s^{-1} , back and forth, parallel to the surface, for 10 or 15 times in each area. The tip of the microcannula usually also emits a visible low power beam, which is useful as a guide during the procedure (Fig. 2.1).

After the use of the laser, the liquefied fat is removed by manual drainage or using a cannula that aspirates it out, under negative pressure. During the postoperative phase, compression bands are applied to the treated areas and the patient has to wear them for 15 - 30 days. Patients are usually able to return to normal daily activity after 1 or 2 days.



Figure 2.1: Laser lipolysis in the lateral abdominal region with evidenced the guide light from the microcannula tip [9].

Laser lipolysis principle

Laser lipolysis is based on the principle of selective photothermolysis. The laser is able to preferentially heat adipose tissue, based on the different absorption characteristics of chromophores in skin tissues. In the skin, light is mainly absorbed by melanin, haemoglobin, fat and water. Fat and water mainly absorb light in the near-infrared band, while melanin and haemoglobin absorb ultraviolet and visible light. Adipose tissue has a lower water content but a higher fat content than other tissues. This means that to achieve the selective effect, it is necessary to find a band in which the absorption coefficient of fat is greater than that of water. Fig. 2.2 shows the curves of optical absorption of human fat and water. Observing it, it can be seen that the peak wavelengths of the two curves are different [11].

Over the years, several lasers have been developed to find the most specific wavelength for targeting fat. Tab. 2.1 reports a summary of the various types of lasers used in laser lipolysis. However, none of these has proven to be better than the others in removing adipose tissue.

In 2008, Mordon and colleagues described a mathematical model for laser lipolysis based on 980 nm diode laser and 1,064 nm Nd:YAG [9]. The study suggests that the result of laser lipolysis depends more on the total energy accumulated in the treated area than on the wavelength used. According to this study, the internal temperature must reach 48 °C to 50 °C, while the external one must remain between

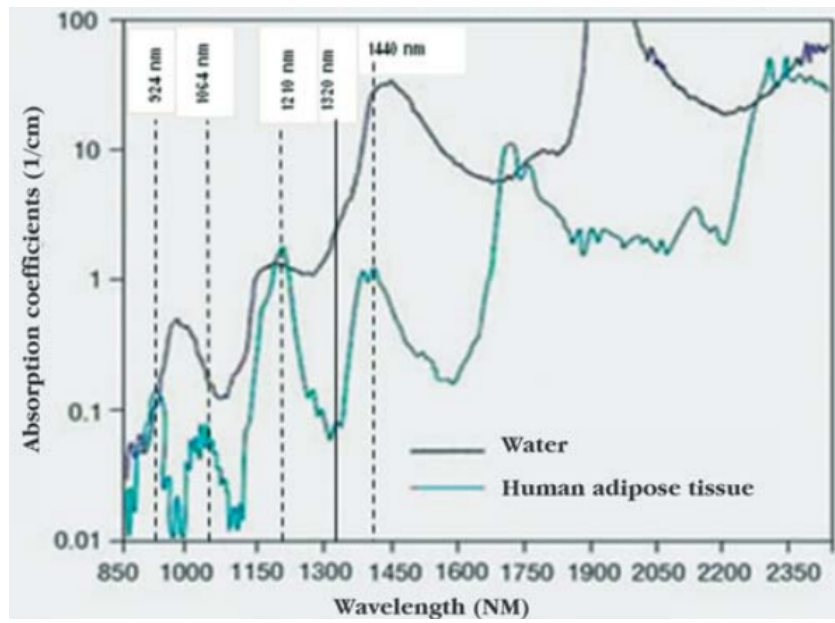


Figure 2.2: Optical absorption curves of fat and water [9].

Table 2.1: Laser lipolysis device [10].

LASER	SYSTEM	WAVELENGTH nm
SmartLipo: Cynosure	Nd:Yag	1064nm
CoolLipo: CoolTouch	Nd:Yag	1320nm
ProLipo: Sciton	Nd:Yag	1064nm/1319nm
LipoLite: Syneron	Nd:Yag	1064nm
Lipotherme: Osyris	Diode	980nm
SlimLipo: Palomar	Diode	924nm/975nm
SmoothLipo: Eleme	Diode	920nm
SmartLipo MPX: Cynosure	Nd:Yag	1064nm/1320nm
SmartLipo Triplex: Cynosure	Nd:Yag	1064nm/1320nm/1440nm

40 °C and 42 °C. In this way, irreversible adipocytolysis is obtained without any damage to the skin. This is important because, if the internal temperature is not high enough, the accumulated energy is not sufficient to achieve a satisfactory result. On the other hand, if the outside temperature is too high, it can cause dermal-epidermal burns (Tab. 2.2).

Table 2.2: Effect of temperature on tissues [12].

Temperature range (°C)	Time requirements	Physical effects	Biological effects
< - 50	> 10 min	Freezing	Complete cellular destruction
0 - 25		Decreased permeability	Decreased blood perfusion, decreased cellular metabolism, hypothermic killing
30 - 39	No time limit	No change	Growth
40 - 46	30 - 60 min	Changes in the optical properties of tissue	Increased perfusion, thermotolerance induction, hyperthermic killing
47 - 50	> 10 min	Necrosis, coagulation	Protein denaturation, not subtle effects
> 50	After ~ 2 min	Necrosis, coagulation	Cell death
60 - 140	Seconds	Coagulation, ablation	Protein denaturation, membrane rupture, cell shrinkage
100 - 300	Seconds	Vaporisation	Cell shrinkage and extracellular steam vacuole
> 300	Fraction of a second	Carbonisation, smoke generation	Carbonisation

The efficacy of laser lipolysis

The greatest benefit of laser lipolysis is its ability to promote skin retraction. Indeed, it appears that the wavelengths used to selectively heat fat also tend to stimulate the thermal denaturation of collagen. This laser-induced collagen denaturation acts as a pro-inflammatory stimulus that induces collagen neosynthesis and vascular proliferation, resulting in skin contraction (Fig. 2.3).

Moreover, laser lipolysis appears to be safer than liposuction. Intraoperative bleeding is reduced due to small vessels coagulation induced by laser light. The small cannula diameter allows a more restricted trauma and, as a result, less discomfort and pain for the patient (Fig. 2.4). These characteristics are also responsible for reducing the effects of ecchymosis and swelling and, consequently, to shorten the postoperative period. The operation requires less effort from the



Figure 2.3: Skin contraction effect. (A) Before and (B) at 6 month follow-up [8].

surgeon because the laser causes fat liquefaction, making its aspiration easier.

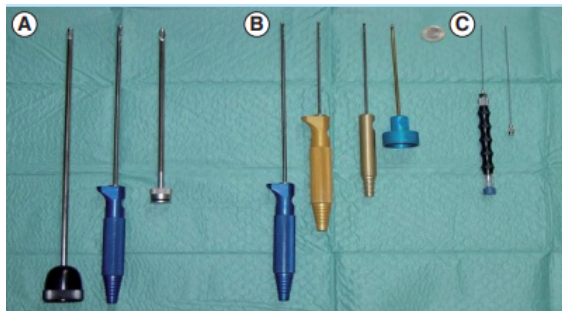


Figure 2.4: Various cannulae used for (A) lipos aspiration, (B) liposculpture and (C) laser lipolysis [8].

In general, in laser lipolysis, there is a minor risk of oedema, neural damage and adipose embolism. However, laser lipolysis can cause some local complications like infections and burns.

Laser lipolysis is used for body contouring in different areas like the abdomen, submental area, hips, thighs and upper arms. Small and fibrous areas are more suitable for this technique. Meanwhile, larger areas of the body can still be treated, but usually, they required more than one procedure.

2.2 Non-invasive techniques

2.2.1 Cryolipolysis

Cryolipolysis is a non-invasive body contouring procedure approved by FDA in 2010. The technique involves the use of an applicator which, using vacuum, sucks the skin in correspondence with the target adipose tissue area. The fat is frozen using controlled cooling at about -10°C . Heat-induced stress triggers panniculitis,

which causes apoptosis of adipocytes without damaging the surrounding tissue. The inflammatory response is activated and macrophages swallow and digest the destroyed fat. This process takes time. In fact, immediately after the procedure, there will not be any change in the subcutaneous fat. The peak of the inflammatory process occurs after about two weeks and continues for three months, during which a continuous reduction of the fat layer can be observed. Being a non-invasive technique, the side effects are reduced compared to other techniques such as liposuction. After a cryolipolysis session, patients may experience pain, sensory disturbances, redness or swelling of the skin, which usually resolve within a few days [13].

2.2.2 Hyperthermic Laser Lipolysis

Over the years, several studies have been conducted to evaluate the effectiveness of non-invasive laser therapy in order to reduce the side effects of the procedure.

In 2010, the use of the 635 nm wavelength laser for (Low-Level Laser Therapy) obtained the FDA approval. In this case, the laser is not used to stimulate the apoptosis of adipocytes, but to create an opening in their cell membrane, from which lipids can leak out [13]. Its different working principle is the reason why the effectiveness of this technique in significantly reducing fat layer thickness is still a matter of debate.

After that, the use of a 1,060 nm diode laser for non-invasive body contouring was approved by FDA. The wavelength of this laser seems to have a good affinity for adipocytes, thus allowing these cells to be selectively damaged in the target area. The target tissue temperature must be kept between 42 °C and 47 °C. Indeed, at this hyperthermic temperature, the structure of adipocytes is altered, leading them to cell death. After the procedure, adipocytes are naturally eliminated from the body. Fat reduction becomes appreciable after 6 - 12 weeks. In particular, studies conducted by Katz show a 13% reduction in the flanks fat thickness, while Bass and Doherty found a 16% reduction in abdominal fat thickness 12 weeks after treatment (Fig. 2.5). For best results, patients can undergo multiple treatment sessions.

The treatment has a good safety profile, in fact, only minor side effects have been reported such as mild tenderness, swelling and induration. Furthermore, to avoid any damage to the skin, the laser device is combined with a cooling system. The latter is placed in direct contact with the skin during treatment to ensure a lower skin surface temperature, while that of the target tissue will still reach hyperthermic values.

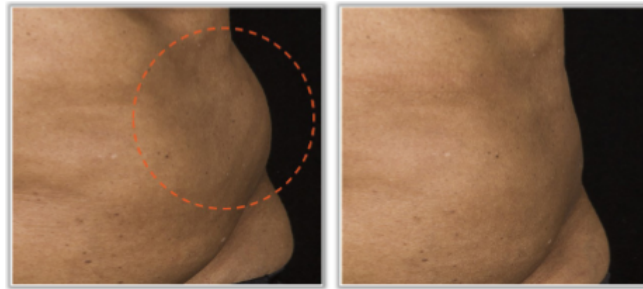


Figure 2.5: Fat reduction of the left flank after 3 months following a single treatment [14].

2.2.3 Radio Frequency

Radio waves generate heat in different tissues according to their impedance. This is why Radio Frequency devices can be used to selectively heat collagen-rich tissues. This causes collagen denaturation in the tissues, thus activating an inflammatory response that, in turn, stimulates the production of new collagen. Indeed, the first effect of these devices is skin tightening. However, they are also able to stimulate apoptosis in adipocytes, thus achieving a second fat-reducing effect.

Commercially available Radio Frequency devices are monopolar or bipolar. Typically, these devices are used to heat the target area up to 43 °C to 45 °C for about 20 min to 30 min. Cooling sprays are used before, after and/or during a treatment session to avoid skin damage. The major complications of these instruments are, in fact, burns, skin infections or pigmentation changes. This is why there are now also some models with a built-in temperature sensor. Although it is possible to see improvements in the skin already after one treatment, in clinical practice it is most common to subject the patient to several treatments, thus achieving a gradual improvement over the next 2 - 6 months.

One of the most used Radio Frequency devices is the Thermage CPT (Solta Medical, Hayward, CA, USA), which was FDA approved in 2002. The Thermage CPT system is a monopolar Radio Frequency device made up of three components: a generator, a handpiece connected to a disposable treatment tip and a cryogen unit (Fig. 2.6). In this device, the generator produces an alternating electric current that propagates from the handpiece into the tissue. The heat produced depends on the tissue's resistance to this current. Finally, the cryogen unit delivers a cryogen spray on the surface of the skin to prevent the temperature in the epidermis from rising excessively [15].



Figure 2.6: Thermage CPT (Solta Medical, Hayward, CA, USA) [15].

2.2.4 Focused Ultrasound

Ultrasound devices use acoustic energy to sculpt the body in a non-invasive and safe manner. Indeed, the only side effects reported are erythema, swelling and mild bruising. The interest in this technology is mainly due to its selectivity, which allows the physician to operate even on narrower target areas (Fig. 2.7). However, the results obtainable with these devices are not comparable to those of laser lipolysis or liposuction techniques. In order to achieve noticeable results, multiple treatments are necessary and the improvement is gradual and can last from 2 to 6 months. Ultrasound devices are divided into two categories: high-intensity (thermal) focused ultrasound and low-intensity, low-frequency (mechanical) focused ultrasound.

High-Intensity Focused Ultrasound (HIFU)

In 2011, the Liposonix device (Liposonix system; Medicis Technologies Corporation, Bothell, WA, USA) was FDA approved for non-invasive waist circumference reduction [16]. This device uses high frequencies (2 MHz) and high intensity (greater

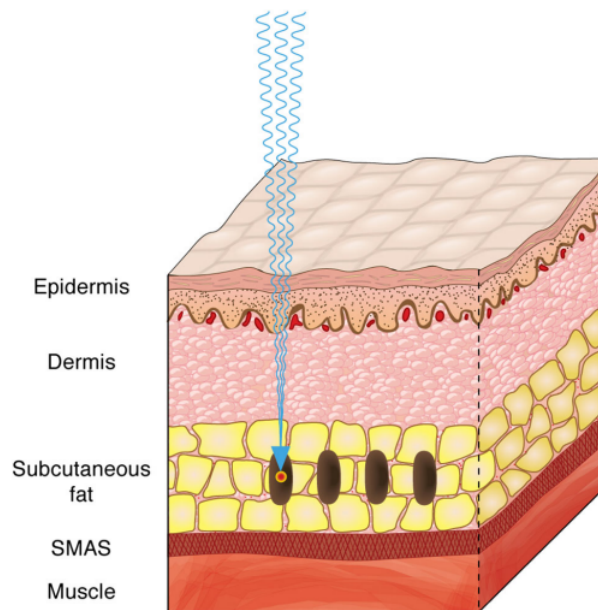


Figure 2.7: Ultrasounds used to ablate adipose tissue [16].

than $1,000 \text{ W cm}^{-2}$) to heat the target tissue to 58°C , inducing adipocyte necrosis and collagen remodelling. The effect produced is localised to a very narrow target area, thus preventing damage to the surrounding nerves and blood vessels. Despite this, some rare side effects due to the effect of high-frequency ultrasound on local nerves have been reported, such as temporary muscle weakness, numbness and tingling.

Low-intensity, low-frequency focused ultrasound

These devices generate a pulse wave that carries a smaller amount of energy: from 0.5 to 10 J cm^{-2} , while for HIFU is about 100 J cm^{-2} .

The Contour I device (UltraShape Ltd., Tel Aviv, Israel) was the first non-invasive ultrasound developed for body contouring [16]. This device uses low-frequency ($(200 \pm 30) \text{ kHz}$), low-intensity (17.5 W cm^{-2}) pulse waves. In this case, fat reduction is due to the mechanical stress induced in adipocytes, which leads them to disruption. The skin, nerves and blood vessels near the target area are not damaged due to their different susceptibility to mechanical stress. Furthermore, using a non-thermal mechanism makes this therapy more tolerable for patients.

2.2.5 High-Intensity Focused Electromagnetic Technology

High-intensity focused electromagnetic field was FDA approved in 2018 for contouring of the buttocks and abdomen [13].

The electromagnetic energy generated by these devices is used to activate supra-maximal contractions of the muscles of approximately 20,000 pulses within one 30 min session. This allows, on the one hand, thickening the muscle layer and, on the other, reducing the fat layer. The mechanism induced at a physiological level by these devices, which leads to these benefits, is still not entirely clear. It appears, however, that the muscle contraction generated induces intense lipolysis in fat cells, causing tissue cell damage that finally leads them to apoptosis. Typically in clinical practice, a minimum of 4 sessions of 30 minutes are spread over approximately 2 weeks. Improvements begin to be noticeable 4 weeks after the last treatment. The treatment is safe and painless: only a few subjects experienced some muscle pain or brief electric shocks. Side effects are also minimal: only mild muscle soreness has been reported.

Chapter 3

Temperature monitoring

3.1 Introduction

From the analysis of the literature, it can be seen that temperature monitoring plays a key role in many body contouring techniques.

In non-invasive techniques, good temperature control is essential to ensure the effectiveness of the treatment. While in invasive techniques, such as Laser Lipolysis, it is important to control the temperature to avoid risks of burns and other tissue damage. Indeed, if too much energy is stored in an area, the risk is causing ecchymoses or small burns. The amount of accumulated energy depends on the movement imposed by the physician: if the physician moves the cannula too slowly or returns it to a site he has already treated, the accumulated energy may be excessive and cause tissue damage [8].

The crucial importance of temperature monitoring in thermal therapies has resulted in a growing interest in the development of new temperature sensors. In the biomedical field, the sensors already on the market turn out to be complex and sometimes inconvenient for such applications. There is, therefore, a search for a solution that will ensure accurate temperature measurement that is practical and easy for the physician to use and that is not harmful to the patient.

Temperature sensors used in the biomedical field are mainly classified into two macro-categories: invasive and non-invasive sensors.

3.2 Non-invasive thermometry

This category of sensors allows obtaining a map of the temperature distribution around the applicator with the added advantage of not having to introduce the sensor into the patient's body. The most widely used non-invasive technologies in the biomedical field are:

- Computed Tomography;
- ultrasound imaging;
- Magnetic Resonance Imaging;

3.2.1 CT-based thermometry

To obtain an image by CT, the subject is hit by an X-ray beam. The transmitted rays reach the detectors with a different intensity, which depends on the attenuation coefficient of the tissues passed through. The value of each pixel of the obtained image is given by the following formula:

$$CT(x, y) = 1000 \cdot \frac{\mu(x, y) - \mu_w}{\mu_w} \quad (3.1)$$

where μ_w is the attenuation coefficient of water, and $\mu(x, y)$ is the average linear attenuation coefficient in the (x, y) pixel [17]. A change in temperature in tissues causes a change in their properties and also in their attenuation coefficient. This connection is the principle on which TC thermometry is based. With CT thermometry, it is possible to reconstruct accurate temperature maps in a short time. However, the dose absorbed by the tissue during X-ray exposure must be taken into account.

3.2.2 MRI-based thermometry

During an MRI scan, a fixed magnetic field and radiofrequency pulses are used. The pulses change the orientation of the protons in the tissue. Between one pulse and the next, however, the protons return to their initial position, emitting the energy previously absorbed (this phase is called '*relaxation*'). The relaxation phase is described by two time parameters, T_1 and T_2 , which are characteristic of the tissue. It was then discovered that these two parameters, together with the Proton Resonance Frequency (PRF), vary as the temperature of the tissue changes. T_2 is not widely used because it has a lower temperature dependency than the other two parameters. The relationship between T_1 and temperature is highly dependent on tissue type and the presence of lipids can cause artefacts. On the

other hand, the relationship of PRF with temperature does not depend on tissue type, but is affected by motion artefacts due to the subject's breathing [17]. Finally, MRI thermometry has a high cost compared to the other temperature monitoring techniques and can only be used in rooms prepared for the use of a magnetic field.

3.2.3 Ultrasound-based thermometry

An ultrasound probe is used to transmit a high-frequency sound wave (typically between 2 MHz and 15 MHz) into tissues. After interacting with the tissue, an amount of energy from the wave is reflected back to the probe.

The time delay between the emitted wave and the reflected wave (called 'echo') depends on the characteristics of the targeted tissue. The time of echo in a homogeneous medium is:

$$t(T_0) = \frac{2 \cdot z}{v_s(T_0)} \quad (3.2)$$

where $t(T_0)$ is the time delay of echo at temperature T_0 and at position z , and $v_s(T_0)$ is the speed of sound in the tissue at the same temperature T_0 [17]. A temperature change in the tissue causes a time shift, Δt , in the ultrasound signal, mainly due to a change in the sound speed in the tissue.

Ultrasound thermometry is a non-invasive technique that is safer than others because it does not use ionising or electromagnetic radiation. On the other hand, this technique is subject to various motion artefacts caused by the breathing or by the heartbeat of the patient.

3.3 Invasive thermometry

This category includes all sensors that require the sensing element to be introduced into the tissue in order to take a measurement. The measurement area covered by these sensors is smaller than that of non-invasive sensors. The most widely used non-invasive technologies in the biomedical field are:

- Thermocouples;
- Thermoresistances;
- Fibre Optic Sensors.

3.3.1 Thermocouples

A thermocouple is a sensor consisting of two wires of different conducting material joined in two joints: the hot joint and the cold joint. The hot junction is positioned close to the point where the temperature is to be measured, the cold junction, on the other hand, has a known temperature. The temperature gradient between the two joints generates a potential difference in the thermocouple, due to the *Seebeck effect*. Therefore, by using a voltmeter, it is possible to measure the voltage of the thermocouple and, knowing the temperature of the cold junction, trace the temperature of the hot junction. Thermocouples have small dimensions that make them suitable for localised temperature monitoring. In addition, they are inexpensive sensors that provide precise measurements, fast response and a wide measuring range. However, they are made of metallic materials, which tends to absorb the laser radiation, with a subsequent increase in temperature that causes an error in the measurement estimate. For this reason, their use in therapies such as Laser Lipolysis or Hyperthermic Laser Lipolysis becomes problematic [17].

3.3.2 Thermoresistances

Thermoresistances, also called *resistance thermometers*, are temperature sensors based on the physical principle that the resistance of a metal changes with temperature.

Therefore, by supplying the sensor with a constant current and reading the voltage drop on it, it is possible to calculate, using *Ohm's law*, the value of its resistance and from it to determine the temperature.

These sensors can be manufactured in different ways. The most common methods involve winding a metal wire around a core or coil made of a non-conductive material (*wire wound* or *spiral*) or the deposition of a thin film of metal on a non-conductive material (*thin film*).

Thermoresistances are identified by the abbreviation of the metal they are made of, followed by the value of their nominal resistance (i.e., that at 0°C). The metals mainly used to make thermoresistances are platinum and nickel. These metals have good stability and resistivity, which makes them suitable for thermal detection. Platinum thermoresistances are more widely used because, although more expensive than nickel ones, they have greater resistance to corrosion and wear. The main platinum thermoresistances are Pt100, Pt500 and Pt1,000.

In the case of platinum thermoresistances, the relationship between their resistance and temperature is described by the *Callendar-Van Dusen equation* (EN 60751), which for $T > 0^\circ\text{C}$, is:

$$R_T = R_0 \cdot [1 + A \cdot T + B \cdot T^2] \quad (3.3)$$

in which the parameters A and B are defined according to the (European) standard IEC 75 [18].

Thermoresistances are advantageous because they have good accuracy and are stable over a wide temperature range (the range of their industrial use is between -200°C and 850°C , as stated in EN 60751). These sensors, however, suffer from self-heating problems, are sensitive to vibration and require a power supply.

3.3.3 Fibre Optic Sensors

Optical fibres are commonly known for their use in telecommunications but are also widely used in the field of sensor technology.

‘Fibre Optic Sensors’ refers to any sensor that exploits the interaction between a measurand and light in an optical fibre to transduce its value or to transmit it to an external transducer.

Fibre optic sensors are classified into *extrinsic* and *intrinsic* (Fig. 3.1):

- in the *extrinsic sensors*, optical fibre is used to convey light to and from an external transducer;
- in the *intrinsic sensors*, is the optical fibre itself that is used as the transducer of the measurand.

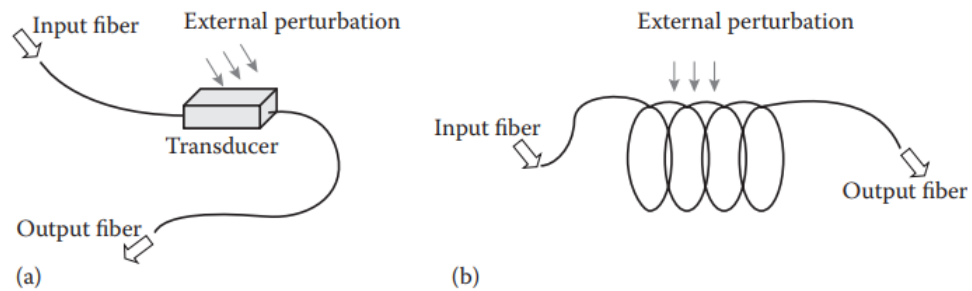


Figure 3.1: (a) *extrinsic* and (b) *intrinsic* fibre optic sensor [19].

Fibre optic sensors can be used to measure various quantities such as:

- strain;
- pressure;

- acceleration and rotation;
- vibration;
- liquid flow and level;
- electric and magnetic fields;
- temperature;
- pH;
- humidity;
- Bio-sensing: detection of single molecules and chemicals.

Fibre optic sensors have numerous advantages:

- resistance in corrosive environments;
- immune to electromagnetic interference
- very low losses during signal transport;
- remote sensing possibility;
- multiplexing capability;
- multifunctional sensing.

In addition, being flexible, lightweight and small in size, these sensors are widely used in the biomedical field. Despite this, even fibre-optic sensors have some disadvantages, including the high cost and the complexity of the necessary instrumentation.

The main fibre-optic sensors used for temperature monitoring are:

- *Fluorescence sensors*

These sensors exploit the link between temperature and the decay of a phosphor. The fluorescent materials used in this sensor are ruby, thulium, alexandrite, or rare-earth materials [20].

The phosphor is placed at the tip of the fibre or even inside it. A pulsating light is used to excite the phosphor, which re-emits a signal that propagates along the fibre and is read by the optical interrogator. The response signal emitted by the phosphor decays exponentially, with a decay time that depends on the temperature (Fig. 3.2). The higher the temperature, the faster the decay. Therefore, using this relationship, it is possible to measure temperature.

These temperature sensors are widely used because of their small size, good

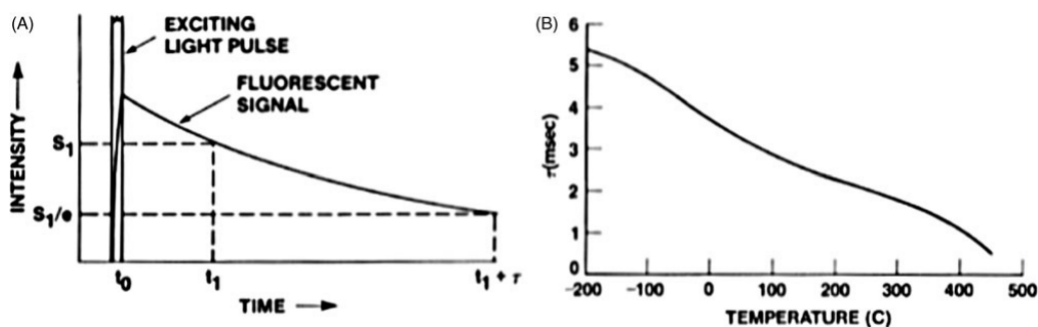


Figure 3.2: (A) Exponential decay of phosphor sensor, (B) Decay time, τ , as a function of temperature [17].

accuracy and wide measuring range (from $-25\text{ }^{\circ}\text{C}$ to $30\text{ }^{\circ}\text{C}$). Unfortunately, however, these sensors have an error in temperature estimation due to their self-heating.

- *Distributed or Rayleigh backscattering sensors*

These sensors rely on the Rayleigh backscattering, which is an elastic scattering occurring in presence of particles much smaller than the wavelength of the incident radiation.

These sensors use a portion of standard single-mode fibres, the same used in optical communications, without requiring any modification because they measure the variation of the Rayleigh backscattering along the fibre, which is proportional to the local temperature, hence the name of ‘Distributed Temperature Sensing’ (DTS) [20].

The advantage of this solution is that it makes possible to measure the temperature profile with a spatial resolution well below 0.1 mm . However, it requires optical reflectometers for the interrogation, which are very expensive (especially those capable of sub-millimetre spatial resolution) and moreover quite slow due to the typically long integration time. Rayleigh backscattering versus the position along the fibre can be evaluated either integrating the signal generated by short pulses in time (ODTR) or in frequency (ODFR).

- *Sensors based on Fabry-Perot interferometry*

In these sensors, a continuous light passes through the optical fibre until it reaches the tip, where a miniaturised Fabry-Pèrot interferometer is located. This consists of two parallel semi-reflecting mirrors placed at a certain distance. The light, which hits one of the two mirrors, is reflected multiple times between these two and then back into the optical fibre until it reaches the

optical interrogator (Fig. 3.3). The output signal from the interferometer is a combination of the interfering signals generated between the two mirrors. Part of these signals will be in phase (*constructive interference*), and the remainder will be in phase opposition (*destructive interference*). Which signals will generate destructive interference and which constructive interference depends strictly on the gap between the two mirrors. This distance changes as a function of temperature, resulting in a variation of the spectral response.

These interferometers are also used to measure other quantities such as pressure and strain.

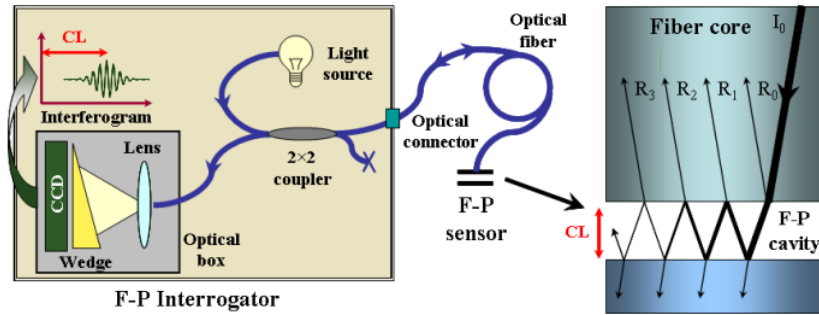


Figure 3.3: Sensors based on Fabry-Perot interferometry [21].

- *Fibre Bragg Gratings*

Unlike the previous ones, these sensors are an integral part of the optical fibre. Bragg gratings, typically a few millimetres long, are realised by inscribing them into the core of a single-mode optical fibre. They can be realised by various techniques, but the final result is always a periodic change in the refractive index of the fibre. In this way, the sensor works as a notch filter centred around a specific wavelength, called the Bragg wavelength that changes with temperature and strain (Fig. 3.4). This opens for their use as sensors.

Bragg gratings are widely used in the biomedical field because they are small, biocompatible and non-toxic [17]. Furthermore, multiple Bragg gratings can be inscribed in a single fibre, allowing multi-point measurements.

Fiber Bragg gratings are the most widespread type of FOS; however, they have also some disadvantages, the most relevant being the quite expensive and complicated interrogation instrumentation required to measure small wavelength variations and the marked strain cross-sensitivity that causes errors in temperature measurements.

Bragg gratings are the sensors analysed in this thesis.

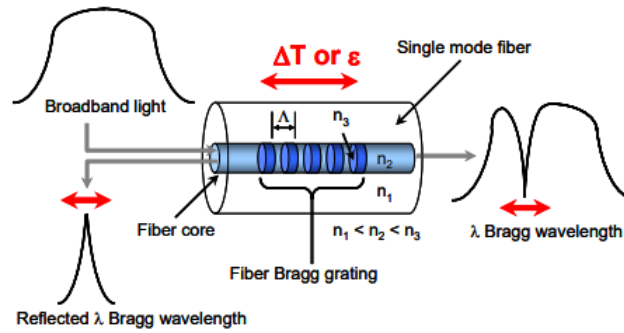


Figure 3.4: Working principle of FBG sensors [21].

Chapter 4

Introduction to the instrumentation

4.1 Optical Fibres

An optical fibre is a filament made of glass or polymer material that allows the guided propagation of photons of light within it, with minimal energy loss.

4.1.1 Structure

The optical fibre consists of concentric cylindrical filaments (Fig. 4.1). Typically, optical fibres consist of four concentric layers:

- *Core*;
- *Cladding*;
- *Coating*;
- *Jacket*.

The *core* is the innermost layer; for the fibres used in this thesis, the core is made of extremely pure silica, with a dopant to slightly increase the refractive index and has a diameter between 10 μm and 50 μm , respectively for single-mode and multi-mode fibres. The *cladding* is made of undoped extremely pure silica to allow total internal reflection at the core-cladding boundary. The typical cladding diameter is 125 μm . The *coating* and the *jacket* are plastic external layers. Their function is to protect the fibre from the external environment. They can consist of different layers and materials depending on the mechanical stress resistance to be provided to the fibre.

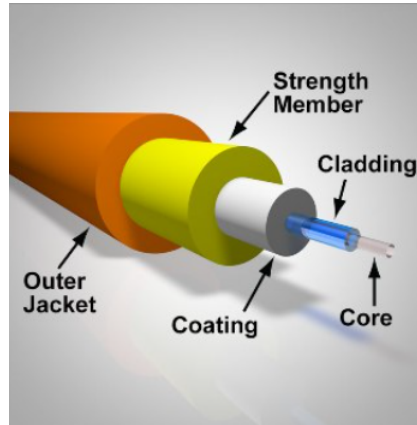


Figure 4.1: Fibre optic structure [22].

4.1.2 Physical principle

Optical fibres confine light by exploiting the refractive index variation between the core and the cladding.

The *refractive index*, n , of a material is defined as the ratio of the speed of light in a vacuum to the speed of light in the material. When a beam of light passes through materials with different refractive indexes, the beam is bent at the interface. This phenomenon is described by the *Snell's law*:

$$n_1 \cdot \sin \theta_1 = n_2 \cdot \sin \theta_2 \quad (4.1)$$

At the core (refractive index n_1)- cladding (refractive index $n_{1=2}$) interface, a light beam propagating in the core is partly reflected and partly transmitted in the cladding with an angle, θ_2 , determined by the Snell's law (Fig. 4.2).

If the angle of refraction, θ_2 , reaches 90° , the light beam can no longer cross the interface. This situation is defined as *total internal reflection* and the Snell's law becomes:

$$\sin \theta_L = \frac{n_2}{n_1} \quad (4.2)$$

where the angle of incidence θ_L is called the *critical angle*.

Any light beam in the fibre that hits the interface with an angle θ_1 greater than the critical angle, will be totally reflected back into the core. This is a fundamental condition to ensure the confinement of light in the core and, together with a phase

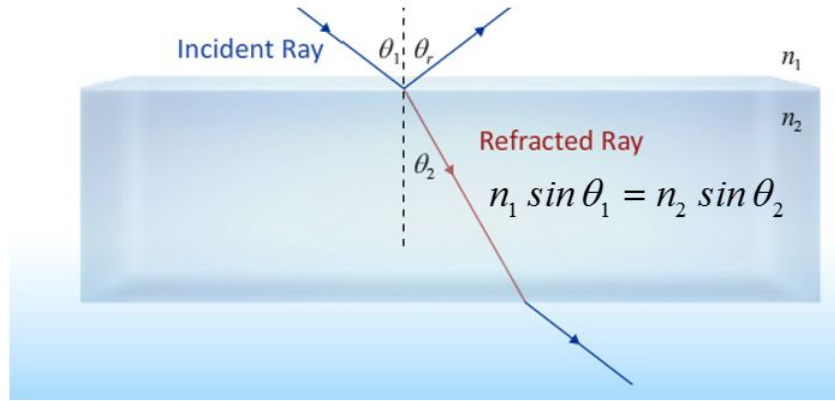


Figure 4.2: The Snell's law [23].

matching condition, determines the so-called guided modes, which are the specific field distribution that propagate unperturbed in the fibre.

For optical fibres, the *acceptance angle* is defined as the maximum angle of entry of a light ray into the fibre for which its propagation in the fibre by total internal reflection is guaranteed (Fig. 4.3). The *numerical aperture* is usually used to assess the acceptance angle of a fibre:

$$\sin \theta = NA = \sqrt{(n_2^2 - n_1^2)} \tag{4.3}$$

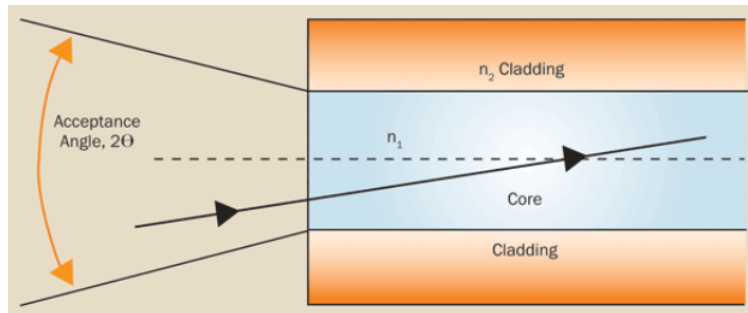


Figure 4.3: Representation of the acceptance angle, 2θ [24].

4.1.3 Optical fibre types and modes

The light beam in the fibre splits into several beams that follow different paths. These paths are called *modes* of propagation. The modes that can propagate in an

optical fibre depend on the refraction index of the fibre materials, its diameter and the wavelength of light.

Optical fibres can be classified into (Fig. 4.4):

- *single mode*: they allow for only one mode of propagation and the light beam propagates through the fibre along an almost straight path. Single mode fibres are characterized by a smaller diameter and a more critical coupling with sources; they are, however, the typical fibers used for FBG sensors;
- *multimode*: they allow for the simultaneous transmission of multiple modes and are characterized by a larger diameter and a much simplified coupling with sources.

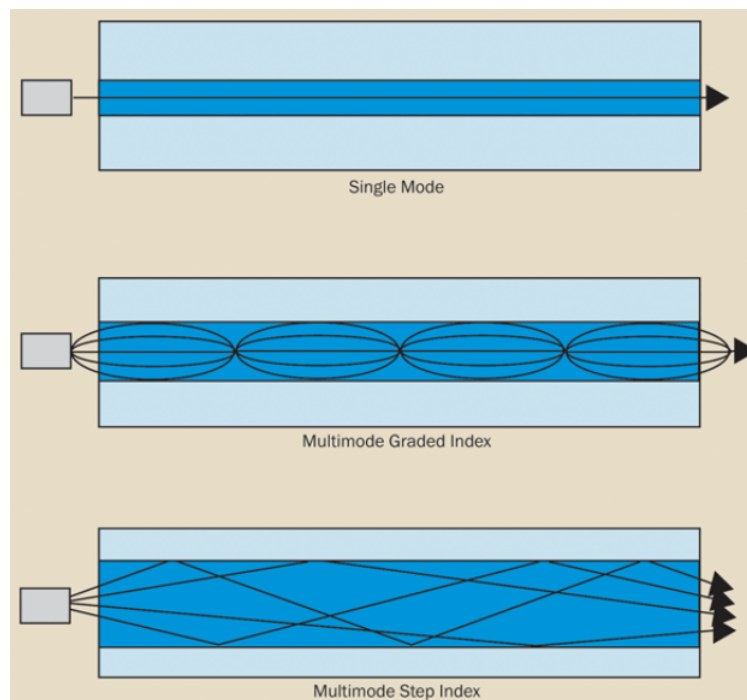


Figure 4.4: Examples of single mode and multimode fibres [24].

Further distinction can be made into (Fig. 4.5):

- *Step-index fibres*: the refractive index of the core and cladding is constant and changes abruptly at their interface;
- *Graded-index fibres* (only for multimode): the refractive index of the core decreases radially from its center to the interface with the cladding;
- *Multi-Core Fibres*: multiple cores are present within the cladding. In these

cores, the signal transmission medium is divided into multiple channels using the *Space Division Multiplexing* (SDM) technique. This enables multiple data to be transmitted simultaneously and therefore with a higher capacity.

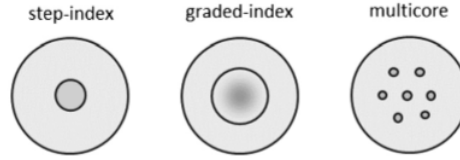


Figure 4.5: Some cross-sections of fibres: step-index, graded-index and multicore [25].

4.2 Fibre Bragg Gratings

Fibre Bragg Gratings are the most widespread type of FOS. They are sensitive to both temperature, T , and strain, ε , which is why they can be used to measure these two quantities.

4.2.1 Physical principle

Fibre Bragg Gratings are fabricated by inducing a periodic refractive index perturbation in the fibre core.

This ensures that, when a broadband light beam propagates in the fibre, the gratings reflect only the spectral component centred around their characteristic wavelength. The characteristic wavelength of a grating is called the ‘*Bragg wavelength*’ and is defined as:

$$\lambda_B = 2 n_{\text{eff}} \Lambda \quad (4.4)$$

where n_{eff} is the effective refractive index of the fibre core and Λ is the periodicity of the gratings.

A change in temperature, ΔT , or strain, $\Delta \varepsilon$, causes a shift in the Bragg wavelength, $\Delta \lambda$. The Bragg wavelength shift, $\Delta \lambda$, with temperature is due to the temperature dependence of n_{eff} and to the thermal expansion of fibre material. While the Bragg wavelength shift with strain is due to the photoelastic effect and to the physical elongation of the fibre. These variations of the Bragg wavelength are described by the following relation:

$$\begin{aligned} d\lambda_B &= \left[\frac{\delta}{\delta\varepsilon} 2n_{\text{eff}}\Lambda \right] d\varepsilon + \left[\frac{\delta}{\delta T} 2n_{\text{eff}}\Lambda \right] dT = \\ &= \left[2n_{\text{eff}} \frac{\delta\Lambda}{\delta\varepsilon} + 2\Lambda \frac{\delta n_{\text{eff}}}{\delta\varepsilon} \right] d\varepsilon + \left[2n_{\text{eff}} \frac{\delta\Lambda}{\delta T} + 2\Lambda \frac{\delta n_{\text{eff}}}{\delta T} \right] dT \end{aligned} \quad (4.5)$$

Dividing both members of the eq. 4.5 by λ_B and using its definition (eq. 4.4), the relative wavelength shift is obtained :

$$\frac{d\lambda_B}{\lambda_B} = \left[\frac{1}{\Lambda} \frac{\delta\Lambda}{\delta\varepsilon} + \frac{1}{n_{\text{eff}}} \frac{\delta n_{\text{eff}}}{\delta\varepsilon} \right] d\varepsilon + \left[\frac{1}{\Lambda} \frac{\delta\Lambda}{\delta T} + \frac{1}{n_{\text{eff}}} \frac{\delta n_{\text{eff}}}{\delta T} \right] dT \quad (4.6)$$

This relation on a macroscopic level becomes:

$$\Delta\lambda_B = k_\varepsilon \cdot \varepsilon + k_T \cdot T \quad (4.7)$$

where

- k_ε is the *strain sensitivity*, which for bare silica optical fibres is approximately equal to $1 \text{ pm } \mu\varepsilon^{-1}$;
- k_T is the *temperature sensitivity*, which for bare silica optical fibres is approximately equal to $10 \text{ pm } ^\circ\text{C}^{-1}$ [26].

4.2.2 Manufacturing methods

Fibre Bragg Gratings are produced by inscribing a periodic perturbation in the core using a light pattern, usually generated by a UV laser or, more recently, a femtosecond laser. Through this process, it is possible to change the refractive index of the fibre core due to its photosensitivity in the case of UV light or nonlinear absorption process in the case of femtosecond lasers. The main fabrication techniques for Fibre Bragg Gratings are:

- *point-by-point* using a *femtosecond* laser: the grating perturbation is defined focusing the laser beam in a sequence of points, allowing an evident flexibility in the spatial shape of the perturbation, which reflects in the spectral response of the grating. The femtosecond laser is a laser that emits pulses with duration in the order of few hundred femtoseconds (Fig. 4.6).

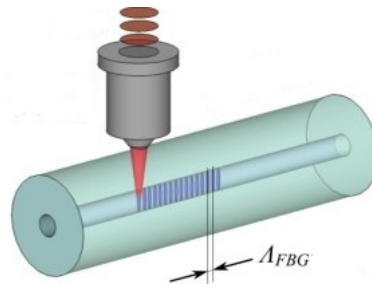


Figure 4.6: Point-by-point manufacturing.

- *phase mask*: in this case, a silica mask is used to create the engraving pattern. The mask is placed between the laser source and the fibre to be engraved. In this way, when the laser light passes through the mask, it transfers its pattern onto the fibre (Fig. 4.7). This technique can be implemented both with UV and femtosecond lasers. Its main advantage is that it produces a “less noisy” spectral response, but it requires a specific phase masks for each FBG with different Bragg wavelength.

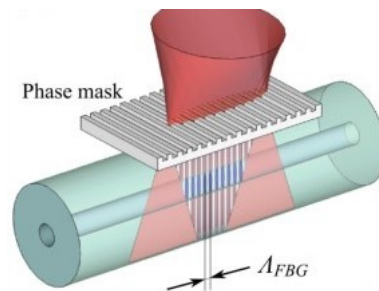


Figure 4.7: Phase mask manufacturing [27].

- *interference lithography (holography)*: this approach is practically used only with UV lasers; the beam is split into two secondary ones, which are then recombined on the fibre. Recombination enables a periodic distribution of light intensity along the fibre. In this way, a variation of the refractive index is realised that follows the pattern of light intensity on the core. The Bragg wavelength of the gratings depends on the angle of incidence of the light and the interference pattern (Fig. 4.8).

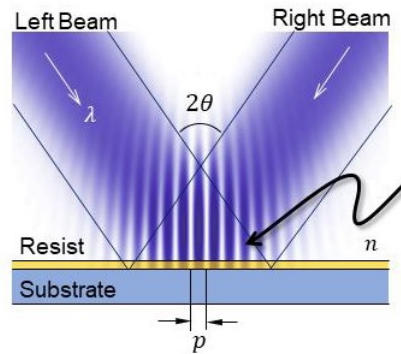


Figure 4.8: Interference lithography [28].

4.2.3 Types of FBGs

Different Bragg gratings can be realised by varying two parameters: the refractive index and the spatial periodicity.

Depending on the spatial periodicity, which is the periodicity of variation of the core refractive index, or the refractive index distribution it is possible to obtain different types of FBGs (Fig. 4.9 and Fig. 4.10):

- *uniform*: constant periodicity of the perturbation over the entire grating length;
- *chirped*: the periodicity gradually increases or decreases along the fibre axis;
- *tilted*: the perturbation is inscribed at an angle with respect to the fibre axis (usually, the variation of the refractive index of each grating is made perpendicular to the core longitudinal axis);
- *array*: a sequence of gratings with different wavelengths is inscribed in the same fibre. In order to realise this type of grating, it is necessary to carefully design the period of the perturbation to prevent their reflection peaks from overlapping. This category of gratings is used to achieve quasi-distributed sensing;
- *apodised*: the amplitude of the refractive index of the gratings is not constant, but changes according to a specific profile. This makes it possible to reduce or completely eliminate the reflection produced by the side lobes. Depending on the profile selected, it is possible to distinguish fibres:
 - *discrete phase shift*: the refractive index profile is not the same along the entire fibre. Two equal profiles are used, but in phase opposition, symmetrical with respect to the Bragg wavelength;

- *gaussian-apodised*: follows a Gaussian profile, with positive offsets;
- *raised cosine-apodised*: the refractive index profile is cosine, with zero offsets.

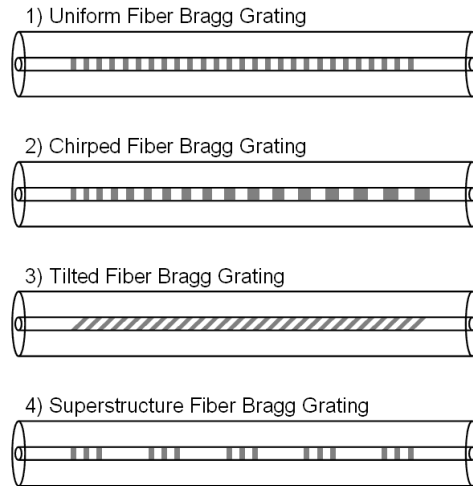


Figure 4.9: FBGs with different spatial periodicity.

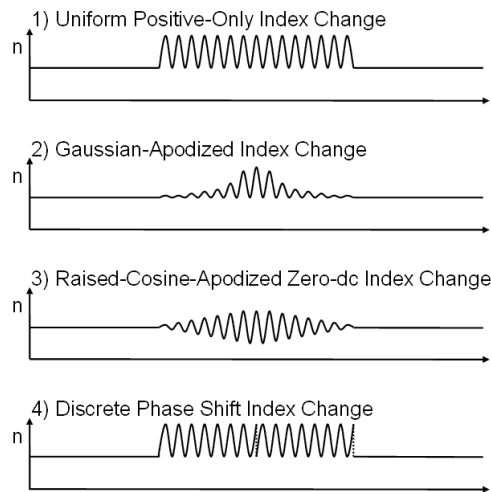


Figure 4.10: FBGs with different refractive index profiles [29].

4.3 Optical Interrogators

Through the evaluation of the wavelength shift of FBGs, temperature and/or strain can be monitored. Optical interrogators are optoelectronic instruments used for reading the wavelength of the FBGs under static and dynamic conditions.

The main components of an optical interrogator are:

- *light source*;
- *optical isolator* and *circulator*: components necessary for the correct guiding of light
- *photodetector*: photodiode for the transduction of the light signal into an analogue signal;
- *filters*: used to select the correct wavelengths of the sensors.

There are two types of optical interrogators, distinguished according to the light source:

- *Broadband source*: the source, LED (light emitted diode) or SLED (superluminescent LED), emits a broadband signal, in the order of several tens of nanometres, which is used to illuminate the FBG; then at the receiver side an optical spectrum analyzer or a spectrometre is used to evaluate the reflected wavelengths and their shifts. In other words, the source is broadband, but the receiver is narrowband. In a simplified implementation the reflected wavelengths are directed towards a bandpass filter, which is necessary to separate the individual components. The filter is followed by a photodiode that transduces the light signal into a corresponding current signal. This current is converted into a proportional voltage value by a transimpedance amplifier and finally into a digital signal by an analogue-to-digital converter.
- *Tunable laser*: in this case the source is narrowband and it is the receiver that is broadband. Indeed, the source is an LD (laser diode) capable of generating a narrow-band beam with variable wavelength. This allows the laser to be tuned to the individual wavelengths of the fibre gratings. In this way, filtering is carried out directly in the emission phase and it is no longer necessary to use the bandpass filter at the receiver, which can be constituted by a simple photodiode. In addition, the intensity of the signal emitted by this source is the same at all wavelengths, allowing for a higher signal-to-noise ratio (Fig. 4.11).

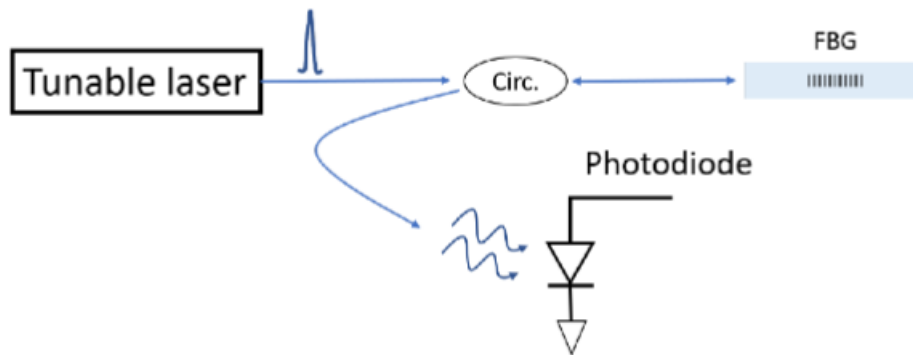


Figure 4.11: Schematic representation of a tunable laser optical interrogator [30].

4.3.1 MICRON OPTICS HYPERION si155

The optical interrogator used in this thesis is the Micron Optics HYPERION si155 from Luna Technologies (Fig. 4.12), which belongs to the category of tunable laser optical interrogators. Its technical specifications are listed below:

- Number of channels: 4 (parallel);
- Reading window: 500 nm-600 nm;
- Wavelength accuracy: 1 pm
- Sensor scan rate: up to 5,000 Hz(80 nm scan)
- Full spectrum measurement included
- Ethernet data interface



Figure 4.12: MICRON OPTICS HYPERION si155.

The reading software used is *ENLIGHT Sensing Analysis*. This software enables data to be saved to text files, the display of the signal spectrum, instant display of peaks detected on selected channels and the temporal display of each peak.

The user interface is shown below:

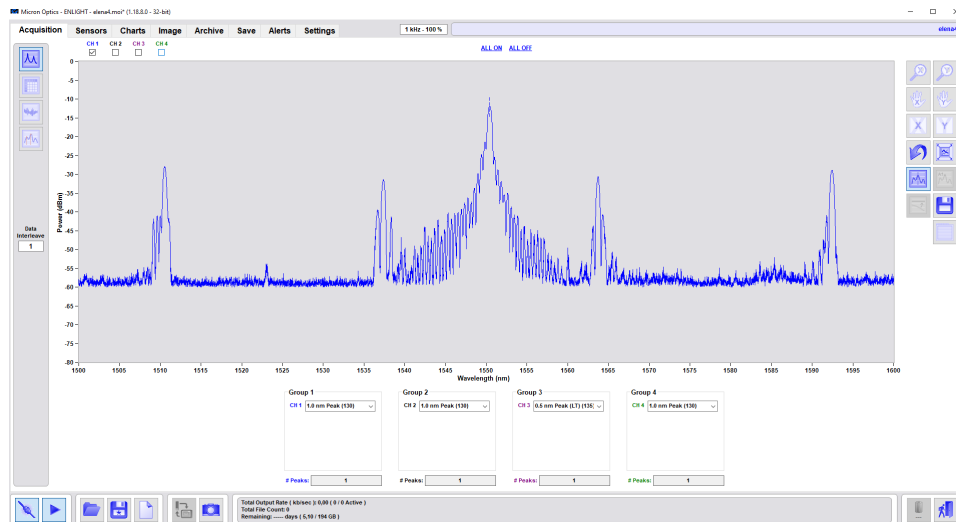


Figure 4.13: ENLIGHT *Sensing Analysis Software* user interface.

Peak detection

The algorithm used first involves filtering the signal to eliminate any noise.

Then a derivative filter is applied in order to determine the position of each peak using the *zero-crossing* technique. The output of the derivative filter is the derivative of the signal. It is therefore possible to locate the peak by looking for the wavelength corresponding to a zero in the derivative of the signal (Fig. 4.14). To correctly locate the peak corresponding to the wavelength of the grating, the user must select the width of the peak search range.

4.3.2 Matlab interface

In this thesis, a Matlab code was written to allow the real-time measurement of the bending radius with the realised fibre optic sensor. In order to get this feedback in real-time, it is necessary to acquire and interpret the Bragg wavelength value instantaneously. The ENLIGHT software does not have direct communication with Matlab software, but it only allows real-time data to be saved for later post-processing in Matlab. For this reason, it was necessary to find a method of direct communication between the Micron Optics HYPERION si155 optical interrogator and the Matlab software. Micron Optics, however, has an API written in Matlab. It is possible to download a package containing the API and some explanatory examples of its use from the official website.

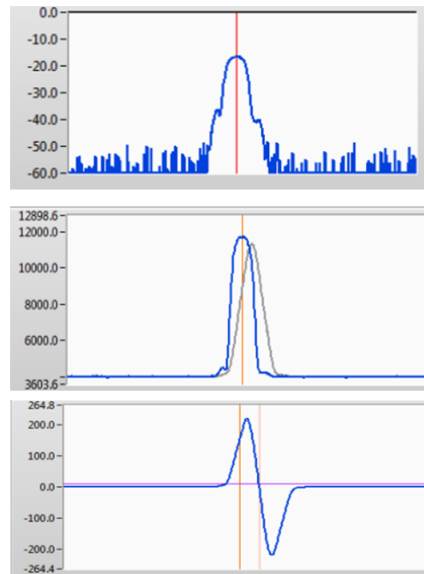


Figure 4.14: Schematisation of the phases of the peak detection algorithm [31].

4.4 3D printers

3D printers belong to the category of *Additive Manufacturing* (AM) systems. The term ‘Additive Manufacturing’ refers to all the techniques used for the creation of 3D objects by adding together material.

The 3D printing process consists of developing a layer-by-layer object. The starting point is always the digital model of the object, which is usually realised with CAD software. The CAD model is converted into a 3D network (*mesh*) of vertices, edges and faces that defines the outer surface of the object using the *triangulation technique* (an STL file is obtained). After that, a *slicing* software is used that divides the object into 3D layers and converts the coordinates of their points into a path that the 3d printer nozzle has to follow. This path is written in the machine language that the 3D printer is able to read and execute called ‘G-code’. Generally, the slicing software is unique to each printer and is supplied with it.

3D printers can be distinguished according to the printing technique:

- *Extrusion*: material is heated and then deposited on the print bed to create the layers of the object from the bottom to the top. The commonly used technique is *Fusion Deposition Modelling* (FDM).
- *Batch polymerisation*: a liquid photopolymer is used. The material is selectively polymerised by a laser beam. *Stereolithography* (SLA) and *Digital Light Processing* (DLP) techniques belong to this category.

- *Powder Bed Fusion*: in this case, the material is in powder form. The material is selectively heated by a laser beam. *Selective laser sintering* (SLS) and *selective laser melting* (SLM) techniques fall into this category.
- *Material jetting* (MJ): the printer head releases a jet of photopolymer resin droplets. The droplets are selectively polymerised by a UV laser light.
- *Binder jetting* (BJ): each layer is produced by the selective release of liquid binder droplets onto a bed of powder;
- *Laminated Object Manufacturing* (LOM): sheets of different materials are cut and glued together to make the object.

Depending on the printing technique used, polymeric, photopolymeric, ceramic or metallic materials can be used [32].

The 3D printing technique enables the production of objects with complex shapes, with lower production times and costs than traditional manufacturing techniques. Creating objects layer by layer allows for the reduction of excess material, making them lighter (where the stresses are lower). However, 3D printing has low accuracy and a maximum limit on the size of objects that can be produced.

4.4.1 ANYCUBIC MEGA X

The Anycubic Mega X 3D printer (Fig. 4.15) was used in this thesis. The printer in question belongs to the FDM category.

Fusion Deposition Modelling (FDM)

The main components of a FDM 3D printer are (Fig. 4.16):

- *print bed*: on which the material is deposited; it can be heated to decrease the thermal shock to which the material is subjected when it leaks out of the nozzle. The strong change in temperature can, in fact, cause torsion deformations in the object.
- *microcontroller*: reads and interprets the printing information contained in a micro SD (offline printing) or sent from a PC via cable (online printing);
- *extruder* and *hot end*: heats and extrudes the material. The tip of the hot end, from which the material is deposited, is called *nozzle*.
- *motor*: moves the head on the print bed; a *step-by-step* motor is generally used because it allows precise and controlled movements;
- *display* and *button panel*: allows the user to interact with the machine.

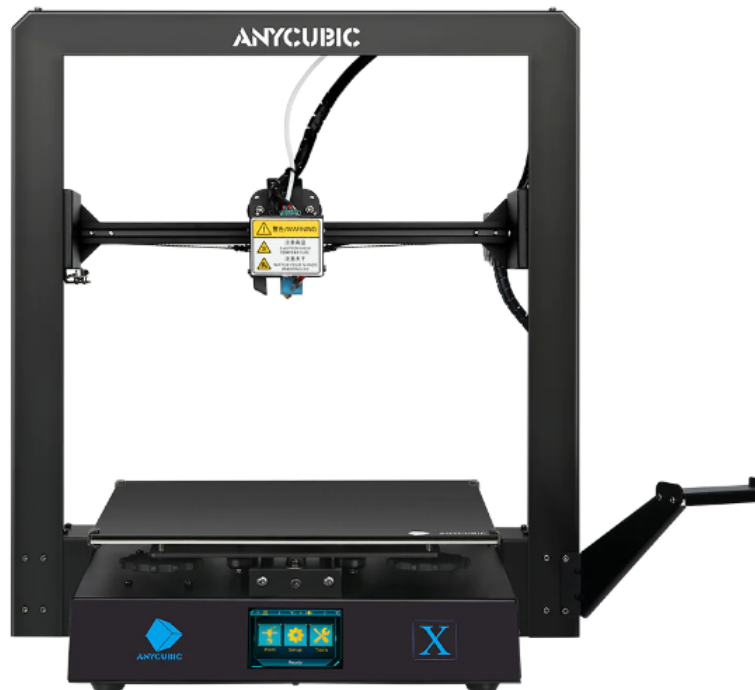


Figure 4.15: Anycubic Mega X 3D printer [33].

Material

The materials that can be used with the Anycubic Mega X printer are: PLA, TPU, HIPS, Wood and PETG.

In this thesis, *Poly Lactic Acid* (PLA) was used, a biodegradable thermoplastic material with low thermal expansion and low printing temperature (extrusion at 160 °C -160 °C).

Technical Specifications

The main technical specifications of the Anycubic Mega X printer are as follows:

- Layer resolution: 0.05 mm - 0.3 mm;
- Position accuracy: X, Y = 0.0125 mm, Z = 0.002 mm;
- Printing speed: 20 mm s⁻¹ to 100 mm s⁻¹;
- Nozzle diameter: 0.4 mm;

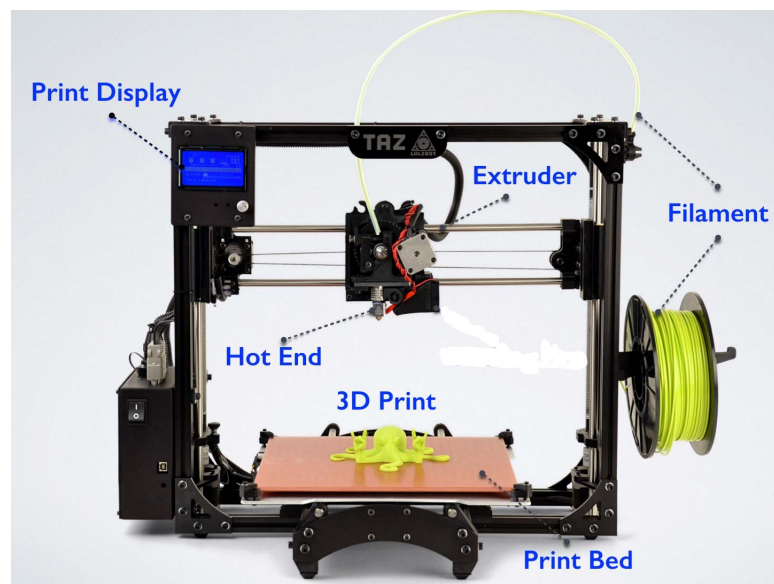


Figure 4.16: The main components of a 3D printer FDM [32].

- Construction dimensions: $300 \times 300 \times 305$ mm;
- Extruder operating temperature: Max. 250 °C;
- Print bed operating temperature: Max 90 °C;
- Printer dimensions: $500 \times 500 \times 553$ mm;
- Slicing software: ‘Cura’

Chapter 5

Separation of temperature and strain effects in FOSs

The aim of the experimental activity is to realise a Fibre Optic Sensor (FOS) for monitoring temperature during operations like laser lipolysis, where the physician continuously moves the laser source under the subject's skin. However, FOSs suffers from cross-sensitivity between temperature and strain. This means that in such applications, the temperature measurements are compromised by errors due to the strain caused by the movement of the cannula. Therefore, to realise this sensor, it is necessary to decouple the two signals, and then remove the one related to strain variations.

Currently, there are several methods for separating temperature and strain signals in FOSs. Some works found in the literature are presented below.

5.1 Seven-Core Fibre sensor for curvature and temperature measurements

Yinggang et al. in their experiment use a Seven-Core Fibre (SCF) to simultaneously measure temperature and curvature. The SCF is a fibre consisting of seven cores arranged according to the profile of a regular hexagon. Looking at the cross-section (Fig. 5.1) of the fibre, one can see that six cores (*outer cores*) are positioned at the vertices of a hexagon, while the seventh is placed in the centre of the cross-section (*central core*). All cores have a diameter of $8\mu\text{m}$ and a mutual distance, l , of $41.5\mu\text{m}$. A grating with a Bragg wavelength of around $1,559\text{nm}$ is inscribed in each core.

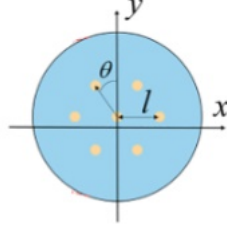


Figure 5.1: SCF cross-section [34].

Since the seven fibres are in the same environment, all their gratings feel the same temperature:

$$\Delta\lambda = t_2 \cdot \Delta T \quad (5.1)$$

where t_2 is the temperature sensitivity of each grating.

However, if the fibre is bent, the gratings of the outer cores are subject to different strains depending on the core in which they are located. On the other hand, the grating of the central core is not affected by any axial deformation, because it is located on the neutral axis of the fibre. For this reason, the grating of the central core can be used to directly measure the temperature. If it is assumed that the fibre is bent in the positive direction of the y-axis, the axial strain suffered by any outer core is given by the following equation:

$$\varepsilon = \frac{l}{R} \cdot \cos \theta = l\rho \cdot \cos \theta \quad (5.2)$$

where:

- R is the fibre radius;
- ρ is the curvature ($\rho = 1/R$);
- l is the distance between an outer core from the central one;
- θ (in the range between -180° and 180°) is the angle formed between the outer core considered and the y-axis.

The relationship between the wavelength shift in an outer core grating and the strain can be expressed as:

$$\Delta\lambda_n - \Delta\lambda_1 = k\lambda_n\varepsilon = k\lambda_n \cdot l \cos(\theta_n) \cdot \Delta\rho \quad (5.3)$$

where:

- $\Delta\rho$ is the curvature variation;
- $\Delta\lambda_1$ is the central-core wavelength shift.

The previous relations allow temperature and curvature to be measured simultaneously with the SCF. The temperature can be measured from the wavelength shift of the core grating with the eq. 5.1. This shift value is equivalent to the *wavelength offset error* caused by temperature in the outer core gratings, $\Delta\lambda_1$. By removing it, it is then possible to derive the curvature value from the wavelength shift of the outer core gratings (Eq. 5.3).

The authors of the article conducted characterization experiments on the sensor to verify the accuracy of their method.

First, they carried out a curvature characterization by placing the sensitive section of the fibre in the bending grooves of an embedded bending test device. The bending was gradually increased from 2.53 m^{-1} to 8.62 m^{-1} by placing the sensor in different grooves. The sensor was left in each groove for approximately 5 min to minimize the effects caused by environmental factors.

Characterization of the sensor with respect to curvature confirmed the linearity of the relationship between Bragg wavelength and curvature. The maximum value of curvature sensitivity obtained was 0.39 nm m^{-1} .

Subsequently, the SCF was characterized with respect to temperature inside a tubular furnace. To characterize the sensor, the temperature was gradually increased in steps of $5\text{ }^\circ\text{C}$ from an initial value of $30\text{ }^\circ\text{C}$ up to a final value of $70\text{ }^\circ\text{C}$, keeping the value of each step constant for about 10 min. This test was repeated under three different curvature conditions.

From these experiments, it was found that the relationship between the Bragg wavelength of the central core grating and temperature remained the same even under different curvature conditions. This confirms that the central core is only sensitive to temperature changes.

Furthermore, the effect of temperature variation is approximately the same for all the cores in the fibre and does not change with curvature. This means that the relationship between the Bragg wavelength of the gratings and temperature is consistent. The temperature sensitivity found in these experiments is around $9.97\text{ pm }^\circ\text{C}^{-1}$ for all the SCF gratings.

These observations confirmed that it is possible to remove the temperature offset error by subtracting the Bragg wavelength shift of the central core from each of the outer cores.

Finally, in the article, the SCF is tested for simultaneous temperature and curvature measurement. In this test, the SCF is subjected to a temperature of 40 °C and a curvature of 5.10 m⁻¹. Temperature is measured by the grating in the central core, while curvature is determined as the average of the curvature values measured by the six outer cores. Both measured values are very similar to the true value of the corresponding quantity, with a relative error of 2.58% for temperature and 2.22% for curvature.

5.2 Shape and temperature sensor based on Bragg Grating Waveguides

As an alternative to Multi-Core Fibres, K.C. Lee et al. propose the use of BGWs (Bragg Grating Waveguides) distributed within a single coreless optical fibre.

The sensor used in this study consists of three parallel waveguides written in a coreless optical fibre with a diameter of 124.7 μm. The three waveguides are positioned to form a triangle in the cross-section of the fibre: one waveguide is located in the centre of the fibre, while the other two are at a radial distance of 40 μm (Fig. 5.2).

In each waveguide, three BGWs of 1 cm are inscribed at a distance of 2 cm from each other. In total, there are nine BGWs, each having a different Bragg wavelength, namely: $\lambda_1 = 1,280$ nm, $\lambda_2 = 1,285$ nm, $\lambda_3 = 1,290$ nm, $\lambda_4 = 1,295$ nm, $\lambda_5 = 1,300$ nm, $\lambda_6 = 1,305$ nm, $\lambda_7 = 1,310$ nm, $\lambda_8 = 1,315$ nm, $\lambda_9 = 1,320$ nm.

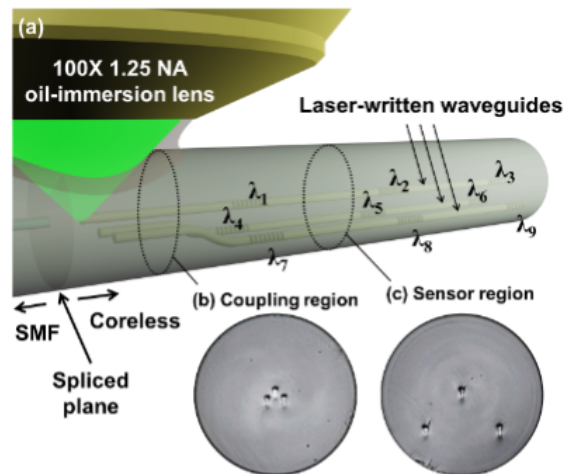


Figure 5.2: (a) Scheme of the sensor based on BGWs; (b) and (c) microscope images of its cross-section, highlighting the positioning of the three waveguides [35].

The Bragg Grating Waveguides are inscribed into the fibre using the procedure described by Grenier et al. of *oil immersion femtosecond direct laser-writing* [36]. The sensor was then spliced to an SMF-28 optical fibre, to allow simultaneous reading of all the BGWs through a single waveguide port. The relationship between the wavelength shifts of the BGWs, temperature variation, ΔT , and strain, ε , is the conventional response of FBGs in SMFs:

$$\frac{\Delta\lambda}{\lambda} = (1 - p_e)\varepsilon + \left(\alpha + \frac{1}{n}\zeta\right) \Delta T \quad (5.4)$$

where:

- p_e is the effective photoelastic coefficient of the fibre;
- α is the thermal expansion coefficient of the fibre;
- n is the refractive index of the fibre
- ζ is the thermo-optic coefficient of the fibre.

The article describes the calibration of the sensor with respect to temperature and strain.

The temperature calibration was performed during a heating process from 24 °C to 250 °C in an oven, resulting in a temperature sensitivity of 9.1 pm °C⁻¹.

The strain calibration, on the other hand, was conducted at room temperature. First, the sensor was wrapped around a 126 mm diameter cylinder, randomly changing its azimuthal orientation. From these tests, the azimuthal angle was determined by exploiting the trigonometric relationships between the three waveguides.

The sensor was then calibrated by bending it along different circumferences with a radius between 40 mm and 117 mm, obtaining a strain sensitivity of $-1.06 \text{ pm } \mu\varepsilon^{-1}$.

The parameters obtained from the calibrations make possible the use of the sensor to simultaneously monitor position and temperature. The temperature is obtained from the wavelength shift suffered by the gratings in the central waveguides. This shift coincides with the temperature offset error of the corresponding gratings on the side waveguides. By removing this error, the strain can be measured from the gratings on the side waveguides.

From these strain values, the corresponding bending radius and azimuthal bending plane values are derived. The finite element method is then applied to these data to reconstruct the shape and position of the sensor.

The sensor demonstrated an accuracy of 0.6 mm in evaluating the position, a precision of $1.1 \times 10^{-3} \text{ mm}^{-1}$ in measuring curvature and of 5 °C in measuring

temperature.

5.3 Temperature, bending and torsion separation with a triangular FBG sensors array

The sensor proposed by Xinhua et al. consists of a rod around which three optical fibres are placed. An SMA (Shape Memory Alloys) rod with a diameter of 0.75 mm is used to construct this sensor. Three SMF-28 optical fibres are bonded around it using AB adhesive at 120° from one another. This increases the size of the entire sensor, bringing the cross-sectional diameter to 1.5 mm.

Fibre Bragg Gratings of 5 mm length, spaced 100 mm apart, are inscribed on each fibre (Fig. 5.3). The Bragg wavelengths of the gratings of each fibre are: 1,524 nm, 1,532 nm, 1,540 nm, 1,548 nm, 1,556 nm.

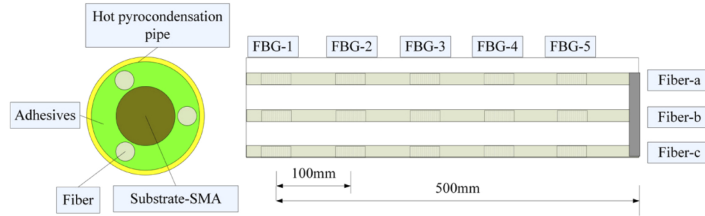


Figure 5.3: Scheme of the sensor structure according to the paper in Ref. [37].

This sensor also allows the separation of temperature and strain effects on the Bragg wavelength of the gratings. In addition, the authors develop a model to distinguish the strain related to a change in bending from that related to a change in torsion.

Therefore, the classical relationship of the wavelength shift of FBGs with temperature and strain becomes:

$$\begin{aligned}\Delta\lambda_i &= k_{\varepsilon,i} \cdot \varepsilon_i + k_{T,i} \cdot \Delta T_i \\ \Delta\lambda_i &= k_{\varepsilon,i} \cdot (\varepsilon_{b,i} + \varepsilon_{t,i}) + k_{T,i} \cdot \Delta T_i\end{aligned}\quad (5.5)$$

Where subscript ‘i’ indicates one of three FBG sensors in the same cross-section, while ε_b and ε_t indicate respectively the *bending strain* and the *torsional strain*.

To define these two quantities, the authors use two models: the *strain-bending model* and the *strain-torsion model*:

- the *strain-bending model* used by the authors is based on the following relationship:

$$\varepsilon_{b,m} = \frac{r_f + r_s}{r_b} \quad (5.6)$$

where:

- $\varepsilon_{b,m}$ is the maximum bending strain;
- r_f is the radius of the fiber;
- r_s is the radius of substrate;
- r_b is the bending radius.

Eq. 5.6 shows the dependence of strain on the bending radius, r_b , and on the distance from the sensor central axis, $r_f + r_s$ (Fig. 5.4(b)).

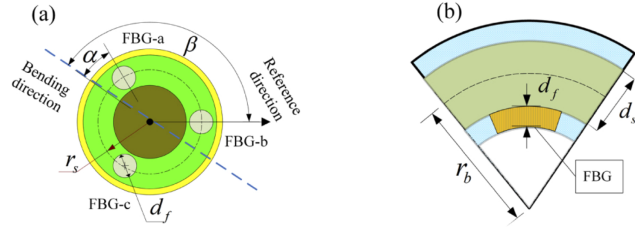


Figure 5.4: (a) Distribution of the FBGs in the same cross-section; (b) The bending effect on one FBG in the sensor.

The gratings, being in different positions with respect to the sensor central axis, feel different strains. In particular, the strains felt by three gratings in the same cross-section are phase-shifted by 120° . According to the diagram shown in Fig. 5.4(a), it is possible to express these three strains with the following expressions:

$$\begin{cases} \varepsilon_b = -1 \cdot \varepsilon_{b,m} \cos \beta \\ \varepsilon_a = -1 \cdot \varepsilon_{b,m} \cos \alpha, \alpha = \beta - 2/3\pi \\ \varepsilon_c = -1 \cdot \varepsilon_{b,m} \cos \psi, \psi = \beta + 2/3\pi \end{cases} \quad (5.7)$$

where subscripts a, b, c denote three FBGs in a cross-section.

- the *strain-torsion model*, instead, is based on the following relationship:

$$\varepsilon_t = \sqrt{1 + \sin \alpha \frac{\phi^2 r^2}{s^2} + \sin(2\alpha) \frac{\phi r}{s}} - 1 \quad (5.8)$$

In this equation, two angles appear: the twist angle, ϕ , and the packaging angle, α .

The twist angle multiplied by the factor r/s (where r is the distance between the central axis of the substrate and the central axis of the fibre and s is the length of the shaft) expresses the shear strain.

Instead, the packaging angle corresponds to the helix angle that the fibres follow along the length of the rod. The fibres, in fact, are glued to the rod following a helical profile because it allows better measurement of the strain suffered from twist (Fig. 5.5).

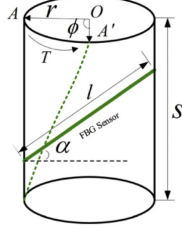


Figure 5.5: FBG sensor packaging diagram.

Applying these two models to Eq. 5.5, the following relationship is obtained:

$$\begin{bmatrix} \Delta\lambda_1 \\ \Delta\lambda_2 \\ \Delta\lambda_3 \end{bmatrix} = \begin{bmatrix} -1 \cdot \varepsilon_{b,m} \cos \beta - 2/3\pi \\ -1 \cdot \varepsilon_{b,m} \cos \beta \\ -1 \cdot \varepsilon_{b,m} \cos \beta + 2/3\pi \end{bmatrix} + \begin{bmatrix} k_\varepsilon \cdot \varepsilon_t \\ k_\varepsilon \cdot \varepsilon_t \\ k_\varepsilon \cdot \varepsilon_t \end{bmatrix} + \begin{bmatrix} k_T \cdot \Delta T \\ k_T \cdot \Delta T \\ k_T \cdot \Delta T \end{bmatrix} \quad (5.9)$$

Where it can be seen that FBGs in the same cross-section feel an equal temperature and suffer an equal strain under twist. Joining these two terms together in the parameter $\Delta\lambda_{\tau t}$, the relationship becomes:

$$\begin{bmatrix} \Delta\lambda_1 \\ \Delta\lambda_2 \\ \Delta\lambda_3 \end{bmatrix} = \begin{bmatrix} -1 \cdot \varepsilon_{b,m} \cos \beta - 2/3\pi \\ -1 \cdot \varepsilon_{b,m} \cos \beta \\ -1 \cdot \varepsilon_{b,m} \cos \beta + 2/3\pi \end{bmatrix} + \begin{bmatrix} \Delta\lambda_{\tau t} \\ \Delta\lambda_{\tau t} \\ \Delta\lambda_{\tau t} \end{bmatrix} \quad (5.10)$$

To solve this non-linear matrix (Eq. 5.10), the authors use the *non-linear least squares method*. In this way, the values of some characteristic parameters such as the bending direction, β , the maximum bending strain, $\varepsilon_{b,m}$, and the wavelength shift induced by temperature and torsion, $\Delta\lambda_{\tau t}$, are derived from the matrix.

In order to distinguish the temperature-induced wavelength shift from the torsion-induced wavelength shift, the strain-torsion model is discretized. The sensor is represented as a set of discrete points, for each of which two local coordinate systems are defined: a fixed and a moving one carried by the sensor bending.

In this way, discrete torsion, τ_i , can be defined as a function of the moving coordinates of two adjacent points of the sensor. Consequently, the strain under torsion can also be discretized as:

$$\varepsilon_{t,i} = \sqrt{1 + \sin^2 \alpha \cdot \tau_i^2 \cdot r^2 + \sin(2\alpha) \cdot \tau_i \cdot r} - 1 \quad (5.11)$$

where the subscript i indicates one of the discrete points.

Substituting a helix angle of 90° into Eq 5.11 gives:

$$\varepsilon_{t,i} = \sqrt{r^2 \cdot \tau_i^2 + 1} - 1 \quad (5.12)$$

At this point, it is possible to distinguish the effects of temperature, curvature and twisting on the Bragg wavelength of the gratings.

The curvature and torsion values obtained, when used in the *discrete Frenet-Serret formula*, allow a shape model of the sensor in 3D or 2D space to be obtained.

To verify the correctness of these analytical models, the authors conducted several experiments.

First of all, the sensor was calibrated against curvature and torsion.

For the curvature calibration, the sensor was forced to bend according to known curves. By applying linear fitting to the data obtained from these tests, the authors derived a sensitivity value of $0.328 \text{ nm } \mu\text{m}^{-1}$. The strain felt by the sensor was found to be underestimated due to the use of AB adhesive, which causes transmission losses.

The analytical model described was then applied to reconstruct the shape of the sensor in both a 2D and a 3D case.

In the 2D case, the sensor is bent around an arc of radius 260 mm.

Instead, a platform consisting of three stepper motors is used to give the sensor a predetermined helical shape. This structure is used both to derive the coefficient relating torsion and wavelength shift and to test the analytical model in reconstructing a 3D shape of the sensor. In this case, the sensor is bent following a helical profile, varying the twist angle from 0° to 100° .

In both the 2D and 3D cases, the maximum error in the spatial reconstruction of the sensor shape is calculated. The maximum error obtained in the 2D case is 3.79 mm, while in the 3D case the error reaches 6.75 mm. In spite of this, the experiments conducted by Xinhua et al. demonstrate the feasibility of their proposed method.

Chapter 6

Strain and associated curvature detection with optical fibres

The methods described in the previous chapter have a common feature: they all exploit the different orientations of the sensing parts of the sensor to produce different strain readings but a common temperature reading.

Inspired by these methods, in this thesis, a sensor consisting of a combination of Fibre Bragg Grating (FBG) sensors, positioned differently around a substrate, was chosen.

First of all, the case of two-dimensional movement is analysed, i.e. where the source moves only in one plane. To study this case, a sensor was constructed embedding two FBGs respectively positioned on the top and on the bottom of a miniaturised cantilever.

Bending the cantilever, it is possible to simulate a two-dimensional movement of the laser source (to the right or to the left). When the cantilever is flexed, the two FBGs positioned on either side of the cantilever will be affected by an opposite strain and by the same temperature. From this relation, it will later be possible to extract from the two sensors measurements, a temperature value compensated for the error due to strain.

Before it can be used, however, the sensor must be characterised with respect to the two physical quantities involved: temperature and strain. This will make possible to extract two relationships for the Bragg wavelength changes, one with

the temperature and one with the strain.

This chapter presents the analyses performed with respect to strain only.

It describes:

- the characterisation procedure of the individual Bragg gratings inscribed in the two optical fibres that will make up the two-dimensional sensor;
- the characterisation procedure of the two-dimensional sensor;
- a two-dimensional curvature measurement test, under constant temperature and variable curvature conditions;

6.1 Characterisation of Bragg gratings with respect to strain

Before realising the sensor, a characterisation of the individual Bragg gratings written in the two optical fibres that will make up this sensor was carried out. The aim is to relate the Bragg wavelength, that is the quantity acquired, to the physical quantity of interest which, in this case, is the strain.

The Bragg wavelength of each grating inscribed in the two fibres is assumed to vary with the strain following a linear relationship:

$$\lambda = \lambda_B + k_s \cdot \varepsilon \quad (6.1)$$

where:

- λ is the Bragg wavelength at room temperature when a certain strain, ε , is applied;
- λ_B is the Bragg wavelength at room temperature and in the absence of deformation forces;
- k_s is the strain sensitivity in pm/ $\mu\varepsilon$;
- ε is the strain applied.

According to Jincong Yi et al., considering Fibre Bragg Grating sensor as a flexible beam with a circular cross-section, it is possible to associate a given strain value with the radius of the sensor curvature [38]. Fig. 6.1 shows a simplified diagram of a FBG sensor portion under pure bending.

When a beam is bent, axial deformation forces are generated inside it that depend on the bending radius, ρ , and the distance from its *neutral layer*, y , according to

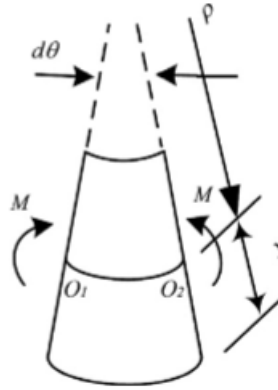


Figure 6.1: Diagram of a FBG sensor portion under pure bending; it also represents the *neutral layer*, O_1O_2 , that is the locus of the fibre points that are unstressed during its bending [38].

the following formula:

$$\varepsilon = \frac{(\rho \pm y)d\theta - \rho d\theta}{\rho d\theta} = \pm \frac{y}{\rho} \quad (6.2)$$

In particular, the equation 6.2 shows that the maximum tension force will act on the convex surface of the fibre, while the maximum compression force will act on the concave one.

The gratings inscribed in the two sensor fibres were characterised using the *bending beam theory* described above. By bending the fibres on curves with different, well-defined radii, their gratings will be affected by different strains, the value of which can be calculated using the equation 6.2.

6.1.1 First characterization test

For a first characterisation test, the fibres were wrapped around different circular grooves of a bottle as in Fig. 6.2.

In particular, three different grooves were used, with radii of curvature of 61.5 mm, 45 mm and 25 mm respectively. However, this method proved to be difficult from the first attempt. The fibres, in fact, did not maintain their position around the bottle throughout the entire test, tending to unravel instead. Sometimes, they did not adhere perfectly to the surface of the bottle, thus assuming a greater radius of curvature than hypothesised. These factors made the characterisation very imprecise and unreliable.

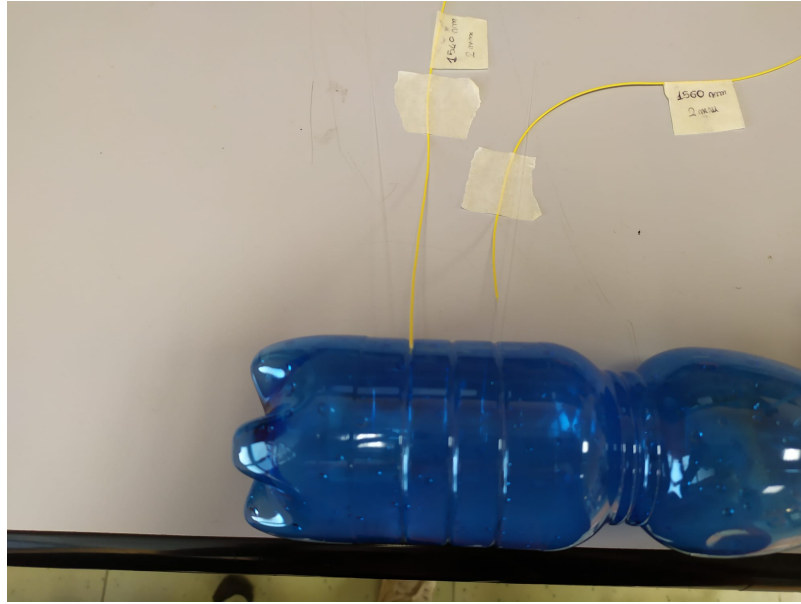


Figure 6.2: Strain characterization of the FBG using the grooves of a bottle.

6.1.2 Construction of the calibration board

The issues encountered during the first characterization test (6.1.1) highlighted the need for a new set of curvatures, on which the fibres adhere perfectly and do not move during the tests. Therefore, it was decided to create a calibration board with a customized design using 3D printing.

In order to characterise the sensor, it is necessary to have a set of curvatures, each with a constant radius different from the others and with a known value. For this reason, a calibration board was chosen with a design in the shape of a quarter cylinder, with a base radius of 210 mm and a height of 10 mm, within which there are eight curves of different and constant radius (Fig. 6.3). The radii of the eight curves are listed in Tab 6.1.

Furthermore, to avoid the issues encountered in the first calibration attempt, it was decided to create the eight curves as grooves with a trapezoidal cross-section. This shape allows the fibre to be inserted into the groove, adhere to the base surface of the groove and maintain its position in that way. In detail, observing the lateral surface of the calibration board (Fig. 6.4), it can be noticed that all eight grooves have the shape of an isosceles trapezoid with the larger base of 8 mm, the smaller base of 1 mm and the height of 7 mm, and they are spaced 25 mm apart from each other.

This design was realised using FreeCAD software. First, the base solid was created,

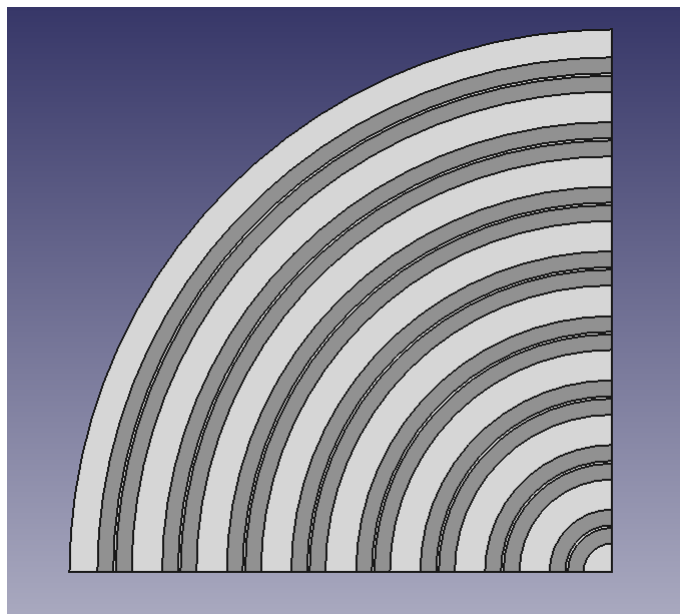


Figure 6.3: Top view of the calibration board.

Table 6.1: Radius of the curves in the calibration board.

Curve	Radius [mm]
1	17.5
2	42.5
3	67.5
4	92.5
5	117.5
6	142.5
7	167.5
8	192.5

which had the shape of a quarter cylinder. Next, the shape of the eight curves was created. To do this, the ‘*sketch*’ of the eight trapezoidal grooves was first created; then, using the *revolution* operation in the software’s *part design* menu, eight arcs with a trapezoidal cross-section and 90° amplitude were generated.

Finally, to create the calibration board design, the boolean *cut* operation was used between the base solid and the eight curves. In this way, eight grooves with the shape of the curvatures previously created were made in the base solid, resulting in the final design shown in Fig. 6.5.

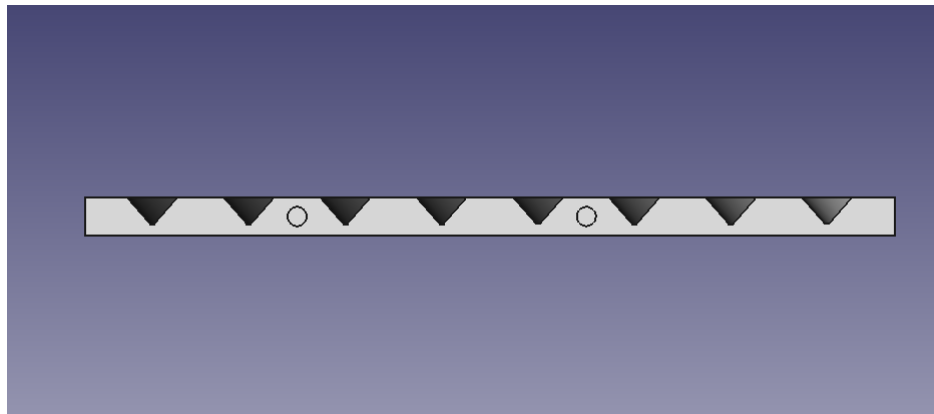


Figure 6.4: Side view of the calibration board.

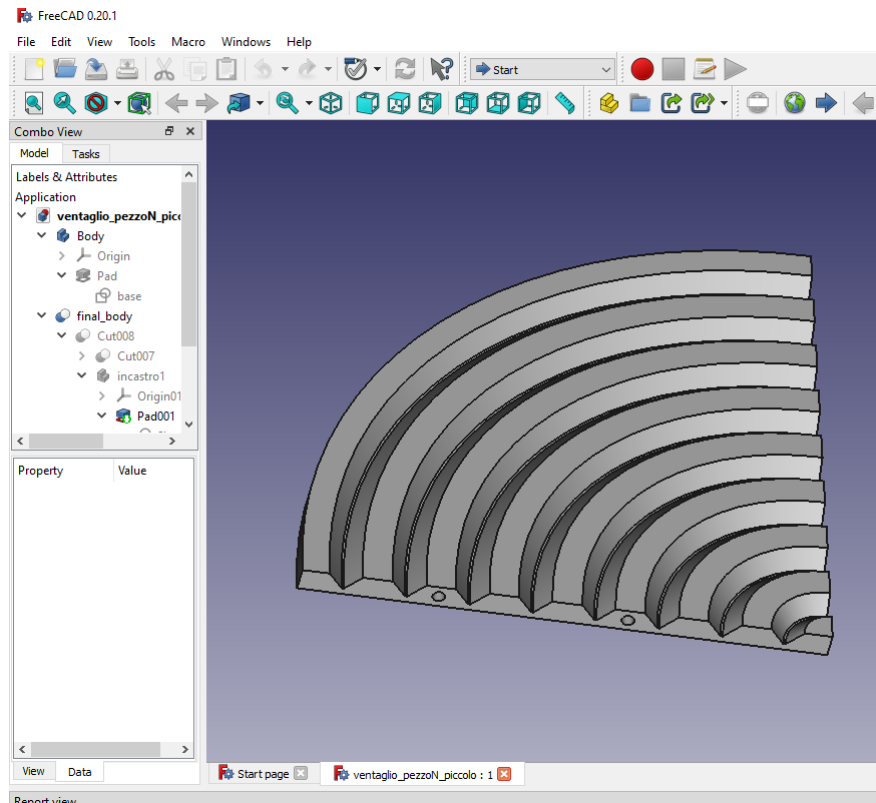


Figure 6.5: The final design of the calibration board.

Once the 3D design was realised, it was fabricated in white PLA using the ANY-CUBIC MEGA X 3D printer (Fig. 6.6). In order to reduce production time and achieve a sufficiently robust calibration board for the intended purposes, the print

parameters *bottom thickness* and *top thickness* were reduced to 0.4 mm and 0.6 mm respectively, and the *number of bottom layers* and *top layers* were set to 2 and 3 respectively.



Figure 6.6: The realised calibration board in white PLA.

6.1.3 Characterisation with the calibration board

The calibration board created was used to characterise the individual Bragg gratings inscribed in the two optical fibres that will make up the sensor. In detail, two SMF-28 Ultra optical fibres were characterised. Both fibres have a single Bragg grating with a length of 2 mm and a Bragg wavelength of 1,540 nm and 1,550 nm respectively. For convenience, the FBG with a Bragg wavelength of 1,550 nm has been labelled ‘FBG A’, while the other with a Bragg wavelength of 1,540 nm has been labelled ‘FBG B’.

Setup and instrumentation

The setup used is that shown in Fig. 6.7.

The instruments used during the trial are:

- the optical interrogator Micron Optics HYPERION si155 and the related software Enlight:
 - acquisition rate: 1 kHz;
 - data saving interval in a text file 1 s;

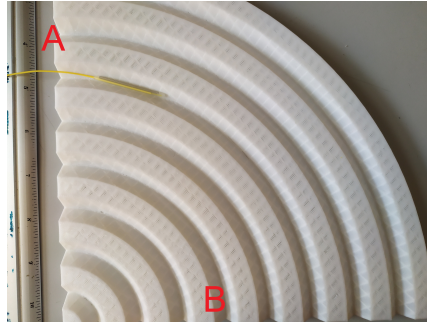


Figure 6.7: The setup used for the FBG characterization: A) optical fibre bent in one of the grooves, B) the calibration board.

- the calibration board.

The procedure adopted is the same for both FBGs. The FBG is connected to the optical interrogator Micron Optics HYPERION si155. The latter is controlled, via an Ethernet connection, by a PC equipped with Enlight software, which allows data to be recorded and saved in a text file. The file is structured in rows, each representing an acquisition sample and containing the sampling time, the number of FBGs detected on each channel of the optical interrogator and the value of the wavelengths recorded for each FBG detected.

During each trial, the FBG is placed in the centre of a bending groove of the calibration board and data are acquired for approximately one minute. This acquisition is repeated for each bending groove of the calibration board, except for the first, smaller one, as it was inconvenient to place the FBG inside it. In addition, a further test was carried out by placing the FBG on the work table, along a rectilinear trajectory, to simulate the condition of no axial deformation forces. All the trials were performed in the same laboratory, at a constant temperature of 20 °C.

The acquired data were post-processed using a Matlab code. The acquired wavelengths are averaged over each curvature trial in order to reduce the noise caused by other external factors. After that, the *polyfit* function is used to extract the linear relationship between FBG wavelength and strain. This function takes as input the degree of the desired polynomial, wavelength and strain values, and provides as output the coefficients of the polynomial that best fits the data, using the *least squares* method. In this case, a first-degree polynomial, the mean wavelengths of each bending trial and the associated strain (calculated using the equation 6.2) is used. In this way, the strain sensitivity values k_s (corresponding to the angular coefficient of the straight line which describes the FBG's behaviour) and the constant λ_B (the intercept of this straight line) are obtained.

The strain estimation error is calculated as the maximum difference (in absolute value) between the analytically calculated strain and that obtained from the interpolation line. Instead, the λ_B estimation error is calculated as the difference (in absolute value) between the λ_B obtained from the interpolation line and the average value of the wavelengths recorded during the strain-free trial.

Results

Tab 6.2 lists the analytically calculated strain values for each curvature of the calibration board.

Table 6.2: Strain associated with the curvatures in the model.

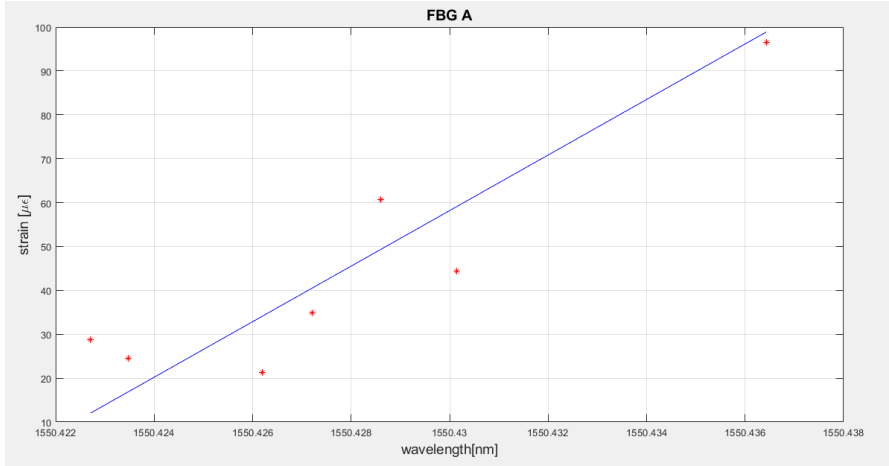
Curve	Strain [$\mu\epsilon$]
1	(not considered)
2	96.47
3	60.74
4	44.32
5	34.89
6	28.77
7	24.48
8	21.30

The average wavelength values of the two FBGs associated with each curvature of the calibration table and those associated with the ‘rectilinear case’ (no axial deformation forces) are reported in Tab 6.3.

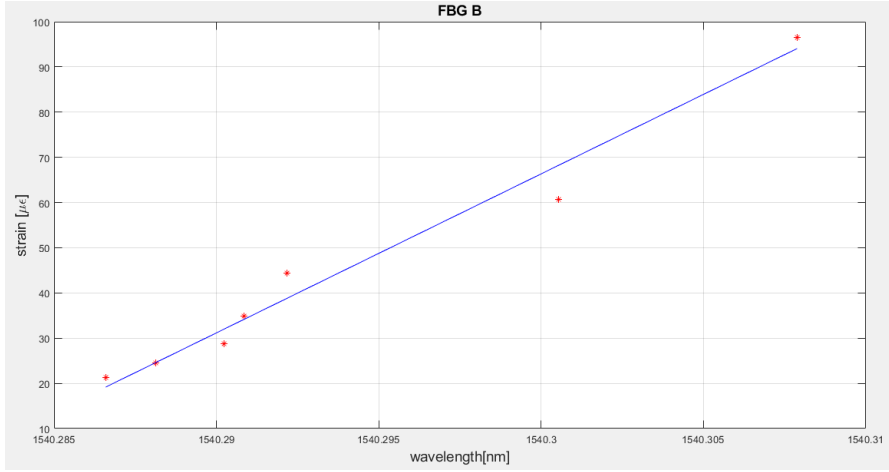
Table 6.3: Average wavelength of the two FBGs for each trial.

Trial	FBG A [nm]	FBG B [nm]
curve 2	1,550.436	1,540.308
curve 3	1,550.429	1,540.301
curve 4	1,550.430	1,540.292
curve 5	1,550.427	1,540.291
curve 6	1,550.423	1,540.290
curve 7	1,550.424	1,540.288
curve 8	1,550.426	1,540.287
rectilinear	1,550.421	1,540.286

The interpolation lines and the average wavelengths of the various trials for both FBGs are shown in Fig. 6.8.



(a) FBG A calibration.



(b) FBG B calibration.

Figure 6.8: The interpolation lines and the average wavelengths of the various trials for both FBGs.

The tables 6.4 and 6.5 report the values of k_s , λ_B , the strain estimation error and the λ_B estimation error of the two calibration lines.

Table 6.4: Parameters of the FBG A calibration line.

$$\begin{aligned} k_s &= 0.158 \text{ pm } \mu\epsilon^{-1} \\ \text{error estimation} &= 0.156 \text{ pm} \end{aligned}$$

Table 6.5: Parameters of the FBG B calibration line.

$k_s = 0.284 \text{ pm } \mu\epsilon^{-1}$
$\lambda_B = 1,540.281 \text{ nm}$
max strain error = $7.465 \mu\epsilon$
max λ_B error estimation = 4.723 pm

Observations

Tab. 6.2 shows that as the radius of curvature increases (from curve 2 to curve 8), the strain decreases. Due to the linear relationship described in the eq. 6.1, the Bragg wavelength of the gratings should also decrease from one curve to the next (of larger radius). This behaviour is evident for FBG B (Tab. 6.3), but not for FBG A. Indeed, in Tab. 6.3, it can be seen that overall, the average wavelength of FBG A decreases from curve 2 to curve 8. Its trend, however, is not strictly decreasing: in some cases, between one curve and the next, its average wavelength increases instead of decreasing (for example, from curve 7 to 8). This could indicate that, during the characterisation of FBG A, greater fluctuations, due to external factors, have occurred. Therefore, the data averaging performed was not sufficient to eliminate their effect from the measurements. This behaviour of FBG A is also the reason why its calibration line has a strain estimation error twice as large as that of FBG B.

The estimation error of λ_B is evaluated as the difference between the λ_B estimated with the calibration line and that measured experimentally. This error is most relevant in the case of FBG B, because it is of the same order of magnitude as the wavelength variation measured between one curvature trial and the next ($\Delta\lambda = 8.36 \text{ pm}$). Whereas in the case of FBG A, this error is an order of magnitude smaller than this wavelength variation ($\Delta\lambda = 7.83 \text{ pm}$).

As for the obtained strain sensitivity values, k_s , they are both an order of magnitude lower than the value indicated in the literature [26]. This also suggests that the trials conducted were affected by errors due to external factors that were not taken into account and therefore corrupted the results.

6.2 Characterisation of the sensor with respect to strain

6.2.1 Construction of the two-dimensional sensor

The choice of realising the sensor by interposing a miniaturised cantilever between the two fibres, instead of joining them directly to each other, is motivated by the results obtained in previous tests (6.1.3). The fibres attached to the cantilever are forced to move with it. This prevents them from being affected by external factors, which could lead them to warp in a different way than that taken into account in the analysis conducted. Therefore, this arrangement allows knowing with greater certainty the deformation to which the sensor is subjected.

Specifically, the two fibres were attached to the opposite faces of the cantilever and positioned so that the two gratings were one next to the other. In this way, when the cantilever is bent to the right or left, the two gratings suffer an equal strain in modulus but in the opposite direction. This is because each grating is affected by the same strain undergone by the face of the cantilever to which it is attached.

This deformation can be evaluated based on the *bending beam theory*, as in section 6.1. However, in this case, the ‘beam’ is no longer the optical fibre, but the cantilever embedded in the sensor. Therefore, the strain of the two faces of the cantilever can be calculated using equation 6.2, where the distance from the neutral axis, y , is equal to $\frac{s}{2}$ for one face, while for the other is equal to $-\frac{s}{2}$:

$$\begin{aligned}\varepsilon_A &= +\frac{\frac{s}{2}}{\rho} = \frac{s}{2} \cdot C \\ \varepsilon_B &= -\frac{\frac{s}{2}}{\rho} = -\frac{s}{2} \cdot C = -\varepsilon_A\end{aligned}\tag{6.3}$$

where s is the thickness of the cantilever and C is the curvature $C = \frac{1}{\rho}$.

The cantilever was made using a thin layer of PLA 0.2 mm thick, 225 mm long and 8 mm wide. In order to be able to recognise the two fibres more easily, it was labelled with ‘face A’ the side of the cantilever to which the FBG A, with a Bragg wavelength of 1,550 nm, was pasted and with ‘face B’ the side of the cantilever to which the FBG B, with a Bragg wavelength of 1,540 nm, was pasted.

Norland Optical Adhesive 61 resin, a liquid photopolymer that cures when exposed to ultraviolet light, was used to glue the fibres to the cantilever. The realised sensor is shown in Fig. 6.9.



Figure 6.9: Picture of the sensor built to study the case of a two-dimensional strain.

6.2.2 Setup and instrumentation

The setup and instruments used during this trial are the same as those used in the 6.1.3: the optical interrogator Micron Optics HYPERION si155 and the calibration board.

The procedure and conditions are also the same, the only difference being that, in this case, the various tests were conducted by wedging the sensor (the cantilever with the two FBGs) into the different bending grooves of the calibration board (Fig. 6.10). Therefore, in this case, two channels of the Micron Optics interrogator have been used, so that the wavelengths of both FBGs of the sensor could be recorded simultaneously during each test. To characterise the sensor, the trials were conducted by bending it along the various curves of the calibration board, excluding, as before and for the same reason, the first curve. Again, the data from each trial was acquired for approximately one minute.

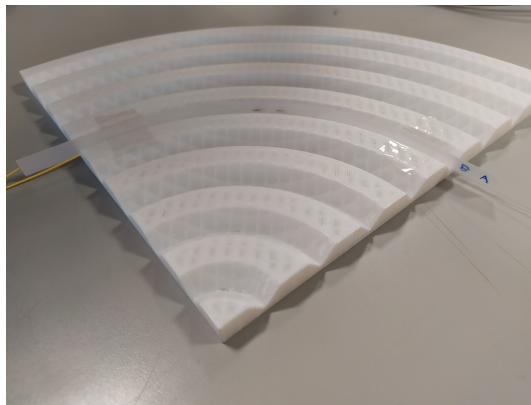


Figure 6.10: Picture of the sensor bent in one of the grooves of the calibration board.

This time, however, the trials on each curvature (from curve 2 to curve 8) were not carried out only once but were repeated six times in order to assess the repeatability of the sensor measures. Specifically, the trials of each curvature were repeated

three times with the sensor ‘bent to the right’ (face B in traction and face A in compression), and then three more times with the sensor ‘bent to the left’ (with face A in traction and face B in compression). The ‘rectilinear case’, used to assess the condition of no axial deformation forces, was also repeated six times. Each of the six repetitions of the curvature tests was used to graph the trend of the deformation felt by the sensor as the curvature, C , changed.

The data from each repetition was analysed on Matlab in the same way. Therefore, the procedure is described considering the data of only one repetition. This provides the wavelengths of FBG A and FBG B acquired in each of the seven curvature trials (from curve 2 to curve 8 of the calibration table) and in the ‘rectilinear case’. These are averaged over each test, for both FBGs. In this way, an average wavelength value is obtained for both FBGs, in each of the eight trials (seven of curvature and the rectilinear case).

Since the sensor has not yet been characterised and qualitative analysis of the sensor behaviour is to be conducted at this first stage, the strain sensitivity, k_s , of the two FBGs was assumed to be equal to the value indicated in the literature of $1 \text{ pm } \mu\epsilon^{-1}$. At this point, the inverse formula to eq. 6.2 is used to calculate the strain felt by the two gratings. In the equation, the average wavelength obtained in the ‘rectilinear case’ is used as λ_B and those obtained in the seven bending tests is used as λ . Thus, for both FBGs, obtaining seven deformation values, one for each bending groove tested. These have been graphed to verify that the strain felt by the two gratings during each test was equal in modulus and opposite in direction.

After this preliminary analysis, the data from each FBG were used to extract the linear relationship between FBG wavelength and strain using the *polyfit* function and the same procedure used and described in the section 6.1.3.

6.2.3 Results

The graphs in Fig. 6.11 represent the strain trend felt by the two gratings embedded in the sensor when it is bent to the right. While the graphs in Fig. 6.12 represent the strain trend felt by the two gratings embedded in the sensor when it is bent to the left. In these graphs, each curve represents the points obtained from one repetition.

The interpolation lines and the average wavelengths of the various trials for both FBGs are shown in Fig. 6.13.

The tables 6.6 and 6.7 report the values of k_s , λ_B , the strain estimation error and the λ_B estimation error of the two calibration lines.

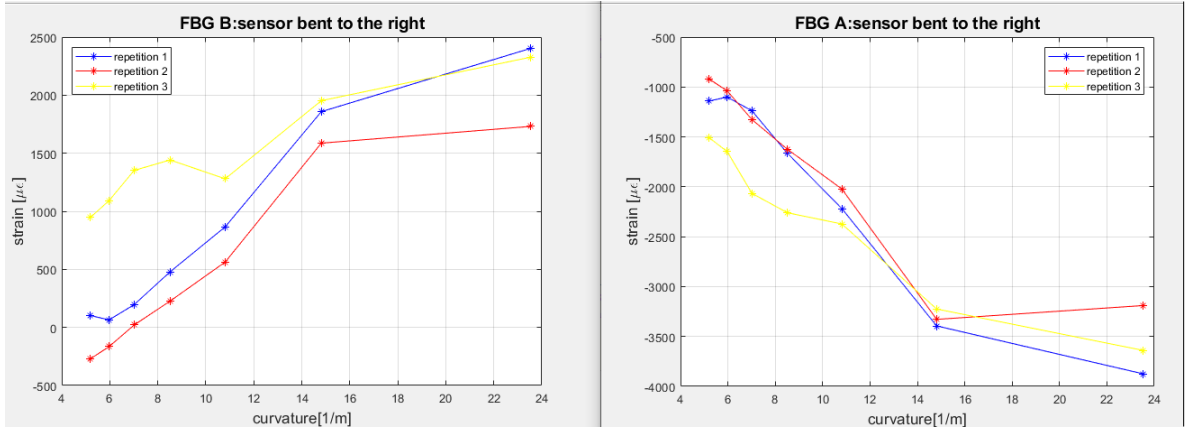


Figure 6.11: Sensor bent to the right.

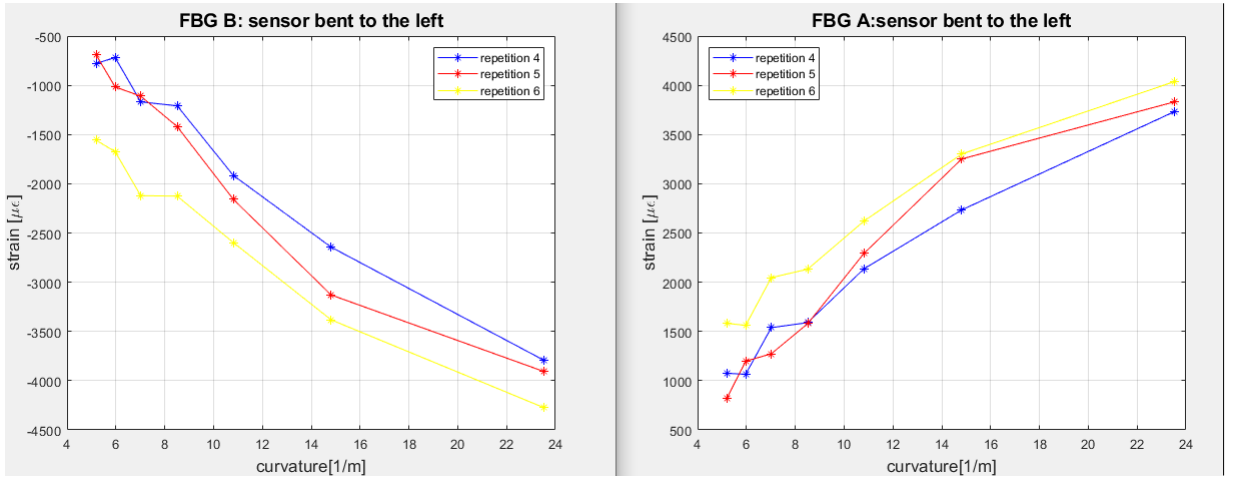


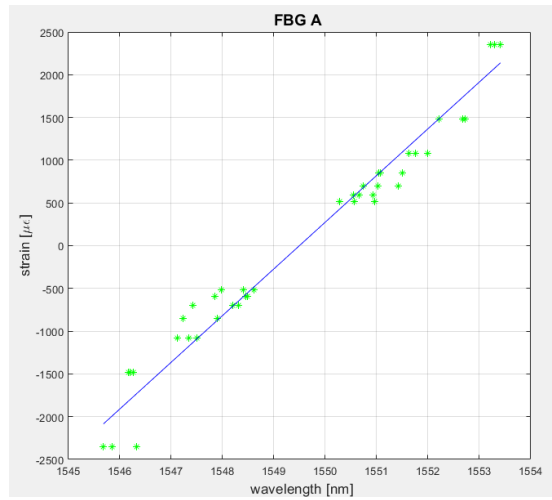
Figure 6.12: Sensor bent to the left.

Table 6.6: Parameters of the FBG A calibration line.

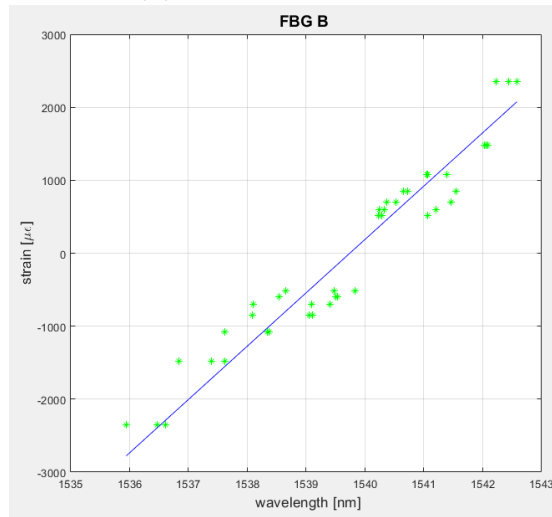
$k_s = 1.830 \text{ pm } \mu\epsilon^{-1}$
$\lambda_B = 1,549.495 \text{ nm}$
max strain error = $624.521 \mu\epsilon$
max λ_B error estimation = 0.014 nm

6.2.4 Observations

It can be seen from Fig. 6.12 that the strain felt by the sensor when it is bent to the left follows the expected trends. In fact, in the graphs of both the gratings, the strain modulus appears to follow a linear trend, increasing as the bending



(a) FBG A calibration.



(b) FBG B calibration.

Figure 6.13: The interpolation lines and the average wavelengths of the various trials for both FBGs.

Table 6.7: Parameters of the FBG B calibration line.

$k_s = 1.368 \text{ pm } \mu\epsilon^{-1}$
$\lambda_B = 1,539.741 \text{ nm}$
max strain error = $643.022 \mu\epsilon$
max λ_B error estimation = 0.556 nm

increases. Furthermore, the strain modulus ranges felt by the two gratings are similar: $4,038 \mu\epsilon$ – $817 \mu\epsilon$ for grating A, $4,274 \mu\epsilon$ – $693 \mu\epsilon$ for grating B. This means that, even if the strain moduli felt by the two gratings do not have exactly the same value during the individual bending trials, they still fall within the same range of values.

However, looking at the direction of deformation, it is clear that the grating A feels a traction strain, in fact only positive values are present in its graph. Instead, the curves of the grating B only pass through negative strain values, so it always feels a compression strain. It can, therefore, be concluded that the two gratings feel a strain that is equal in modulus and opposite in direction, as predicted in the analytical analysis above.

In the case of the sensor bent to the right (Fig. 6.11), however, this behaviour is less evident. First of all, the strain pattern in the two gratings does not always seem to follow a linear trend, increasing with bending. This is most evident in the ‘*Repetition3*’ curve, whose first four points take on greater values than those of the other two curves. Furthermore, the ranges of values of the strain modulus felt by the two gratings are not equal. While the values recorded by grating A are similar to those found in the previous case (i.e. the sensor bent to the left), the values recorded by grating B are lower. Looking at the direction of the strain, it can be seen that the strain felt by the grating A always takes on negative values, therefore feels a compression strain, as expected. In contrast, the grating B at the first two points of the ‘*Repetition2*’ curve feels a negative strain, when this should always be positive since, during these trials, the grating B is always subjected to a traction strain.

The different behaviour of the grating B found in tests where the sensor is bent to the right affects the parameters of its calibration line. In fact, the calibration line of FBG B has a strain estimation error and a estimation error of λ_B greater than those of the curve of FBG A.

The strain sensitivity, k_s , assumes values similar to those found in the literature. This shows that gluing the FBGs to the cantilever proved efficient in limiting the effects caused by external factors. However, the k_s values for the two gratings are slightly higher than the value given in the literature and slightly different from each other. This may be due to the use of resin to bond the two fibres to the cantilever. In fact, the mechanical properties change depending on the thickness of the resin layer used on each side of the cantilever.

6.3 Use of the sensor for two-dimensional deformation measurements

In order to conclude the two-dimensional strain analysis, it was tested the ability of the sensor to measure the curvature. To do this, it would have been sufficient to use only one of the sensor gratings. Here, both sensor gratings were tested individually under conditions of constant room temperature and varying curvature.

6.3.1 Setup and instrumentation

The setup and instruments used during this trial are the same as those used in the previous trials (section 6.1.3 and 6.2.2): the optical interrogator Micron Optics HYPERION si155 and the calibration board.

The only difference is that in this case, a real-time acquisition of the Bragg wavelength of the gratings was used. Therefore, instead of the text file created by the Enlight software (used in previous tests), direct communication between the optical interrogator and the Matlab software is used. The realised code reads the Bragg wavelength of one of the sensor gratings when prompted to do so. The user can also decide to continue the acquisition or to stop it.

For each acquisition, the code evaluates the position of the sensor: whether the sensor is straight or is flexed to the right or to the left. This evaluation is done by comparing the value of the acquired Bragg wavelength, λ , with the λ_B obtained from the grating calibration line. In addition, when the sensor is bent (to the right or left), the code also estimates its radius of curvature using the inverse formulas to the equations 6.1 and 6.2.

This code was tested with both grating A and grating B by bending the sensor over some of the curves in the calibration table. The code can be used by bending the sensor on any curve. For these tests, it was preferred to use the curves of the table because, having a known radius, they allow the radius estimation error to be evaluated.

6.3.2 Results

Table 6.8 shows the results obtained by measuring the radius of curvature of the sensor using grating A. Each row in the table represents the results of one test. Each row contains the Bragg wavelength instantaneously acquired from grating A, the radius of the curve on which the test was performed, and the direction and radius of curvature estimated by the sensor. Finally, the last column of the table contains the radius estimation error calculated on each test as the maximum

deviation between the ‘estimated radius’ and the ‘real radius’.

Table 6.8: Estimation of the bending radius with the grating A.

λ read	Real radius [mm]	Estimated radius [mm]	Direction	error [mm]
1548.34579	67.5	159.235	right	91.735
1551.45055	92.5	93.615	left	1.115
1551.23236	117.5	105.374	left	12.127
1551.06335	142.5	116.731	left	25.769
1549.48919	x	x	straight	x

Instead, Table 6.9 shows the results obtained by measuring the radius of curvature of the sensor using grating B. Each row in the table represents the results of one test. Also here, each row in the table represents the results of a test. Each row contains the instantaneously acquired Bragg wavelength from grating B, the radius of the curve on which the test was performed, the direction and radius of curvature estimated by the sensor, and the error in estimating the radius of curvature.

Table 6.9: Estimation of the bending radius with the grating B.

λ read	Real radius [mm]	Estimated radius [mm]	Direction	error [mm]
1538.09763	67.5	83.227	left	15.727
1538.71586	92.5	133.416	left	40.916
1538.98964	117.5	182.026	left	64.526
1539.05204	142.5	198.510	left	56.01
1541.61067	67.5	73.158	right	5.658
1540.88391	117.5	119.681	right	2.181
1540.85400	167.5	122.897	right	44.603

6.3.3 Observations

Looking at Tab. 6.8 and Tab. 6.9, it can be seen that the deviation between the ‘estimated radius’ and the ‘real radius’ is smaller when the grating feels a traction strain, that is when the sensor is bent to the left for FBG A and when the sensor is bent to the right for FBG B. This is observed in both cases: when grating A is used and when grating B is used.

The radius estimation errors are an order of magnitude smaller than the value of the measured quantity (the radius of the curve). An exception is the case of grating A in compression (i.e. when it is bent to the right) along the curve of radius 67.5 mm, which has a larger error than all other cases. Whereas in the case of grating A in traction (i.e. when it is bent to the left) along the curve of radius

92.5 mm and in the case of grating B in traction (i.e. when it is bent to the right) along the curve of radius 117.5 mm, the error is two orders of magnitude less than the radius considered.

Chapter 7

Temperature detection with optical fibres

The previous chapter described the analyses done with respect to two-dimensional strain. This chapter, on the other hand, describes the analyses made with respect to temperature. In detail, this chapter presents:

- the characterisation procedure of the individual Bragg gratings of the two-dimensional sensor;
- the characterisation procedure of the two-dimensional sensor;
- the temperature and curvature measurement test, under variable temperature and constant curvature conditions.

7.1 Characterisation of Bragg gratings with respect to temperature

In this section, a characterisation of the individual Bragg gratings written in the two optical fibres that will make up the final sensor was carried out. The aim is to relate the Bragg wavelength, that is the quantity acquired, to the physical quantity of interest which, in this case, is the temperature.

The Bragg wavelength of each grating inscribed in the two fibres varies with the temperature according to the linear relationship:

$$\lambda = \lambda_0 + k_T \cdot T \tag{7.1}$$

where:

- λ is the Bragg wavelength at the temperature T ;
- λ_0 is the Bragg wavelength at a temperature of $0\text{ }^\circ\text{C}$;
- k_T is the temperature sensitivity in $\text{pm}/^\circ\text{C}$;
- T is the temperature applied.

7.1.1 Setup and instrumentation

The temperature characterisation of the two fibres labelled FBG A and FBG B in Section 6.1.3 is described here.

The instruments used are:

- optical interrogator Micron Optics HYPERION si155;
- temperature sensor Pt1,000, coefficients:
 - $A = +3.9083 \times 10^{-3} \text{ }^\circ\text{C}^{-1}$
 - $B = -5.775 \times 10^{-7} \text{ }^\circ\text{C}^{-2}$
 - $R_0 = 1,000 \text{ } \Omega$
- multimeter, to read the resistance, R_M of the platinum thermoresistor;
- PTC1/M Temperature-Controlled Breadboard by THORLABS (Fig 7.1), capable of controlling its surface temperature in the range from $5\text{ }^\circ\text{C}$ to $45\text{ }^\circ\text{C}$;
- hollow cube in PLA with a metal cylinder inside: this structure is used to keep the temperature uniform and protect the sensors.



Figure 7.1: PTC1/M Temperature-Controlled Breadboard by THORLABS.

The setup is shown in Fig. 7.2.

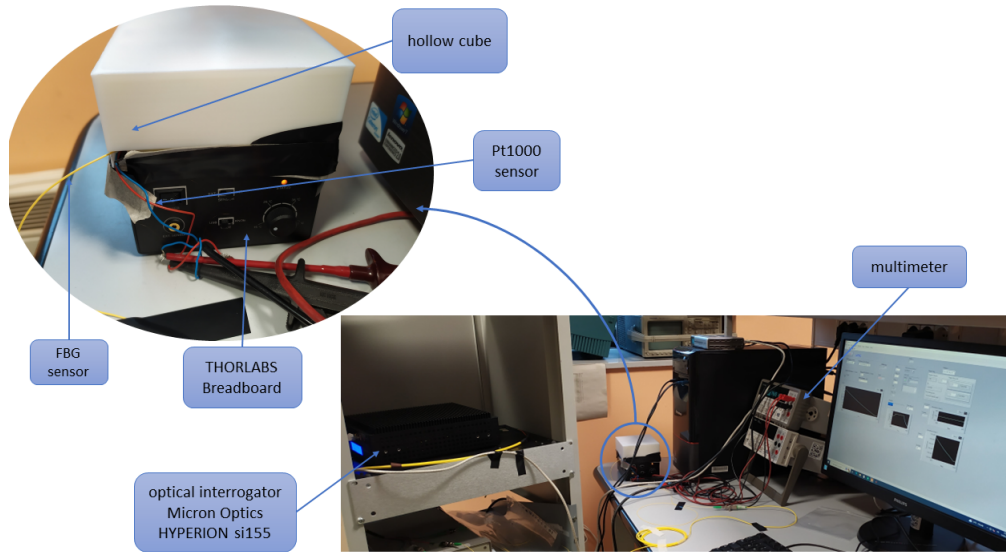


Figure 7.2: The setup used for the trial.

The characterisation was conducted in the same way for both fibres. The sensors are analysed during a heating process with a stepped profile.

The fibre to be characterised and the reference sensor (Pt1,000) are inserted into the appropriate hole of the cube. Data acquisition and storage are handled by a labVIEWTM programme. This programme allows the user to switch on the THORLABS breadboard and set the temperature range and the step variation. It is set an initial temperature of 15 °C, an end temperature of 45 °C and a temperature variation between one step and the next of 5 °C. Each temperature level is maintained for approximately 10 minutes (*stationary phase*), after which the breadboard temperature switches to the next level (*transient phase*). Data are acquired at a frequency of 1 kHz and saved in a text file. Each line of the file represents a sample and contains the sampling time, the set temperature, the temperature read from the reference sensor and the Bragg wavelength of the grating.

The data were then processed by Matlab code. Both the temperature measured by Pt1,000 and the Bragg wavelength of the grating to be characterised follow the step profile imposed by the THORLABS breadboard. The sensor is characterised during the *stationary* phase since the temperature and sensors are stable during this phase. For each step, a window of 10 samples is selected, starting from the last sample belonging to the step. In each window, the average of the temperature values measured by Pt1,000 and the average of the Bragg wavelength values of the grating are calculated.

The profile used to characterise the sensors has seven steps, so seven pairs $(\bar{\lambda} - \bar{T})$ are obtained. These are given as input to the *polyfit* function. With this function, requiring a first-order polynomial, the coefficients of the grating calibration line, k_T (the angular coefficient of the line) and λ_0 (the intercept) are obtained.

Finally, the temperature estimation error is calculated as the maximum difference (in absolute value) between the temperature measured by the reference sensor and that obtained from the interpolation line.

7.1.2 Results

Below are reported first the results of the characterisation of FBG B and then of FBG A.

Fig. 7.3 shows the temperature profile set on the THORLABS breadboard and the temperature profile measured with the reference sensor (Pt1,000) during the characterisation of FBG B.

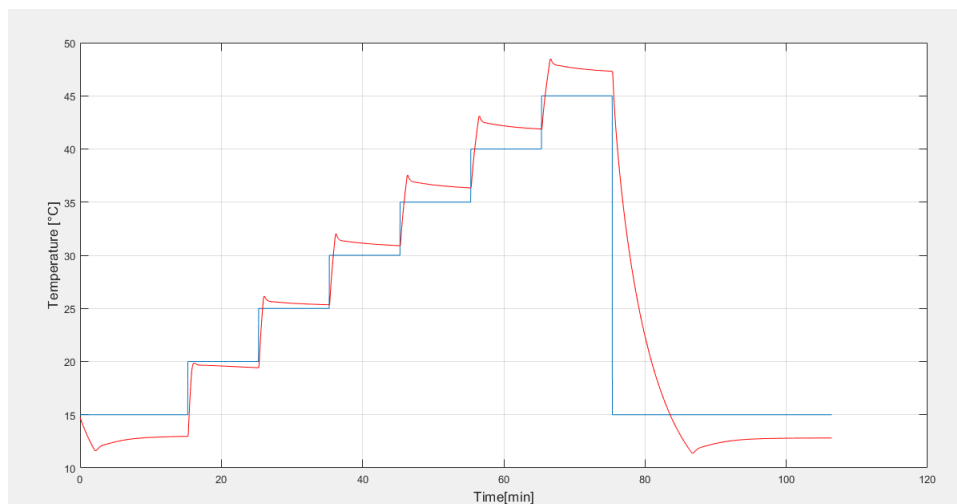


Figure 7.3: The temperature profile set on the THORLABS breadboard in blue and the temperature profile measured with the reference sensor in red.

Tab 7.1 reports the set temperature on the THORLABS breadboard and the real temperature measured with the reference sensor (Pt1,000) during the characterisation of FBG B.

Fig. 7.4 shows the Bragg wavelength profile of the grating during the trial. The figure also highlights the seven steps considered for the characterisation of FBG B.

The average Bragg wavelength values of FBG B during the seven temperature steps are shown in Tab. 7.2.

Table 7.1: Set and real temperature during the trial.

Set temperature [°C]	Real temperature [°C]
15	12.964
20	19.425
25	25.343
30	30.904
35	36.335
40	41.876
45	47.315

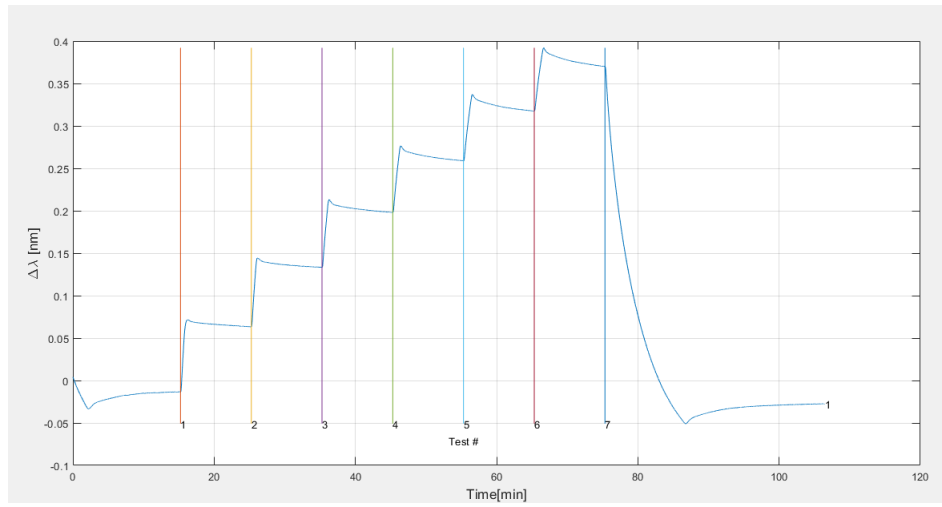


Figure 7.4: The Bragg wavelength profile of the grating B during the trial.

Table 7.2: Set temperature and average Bragg wavelength in the seven steps.

Set temperature [°C]	Average Bragg wavelength of FBG B [nm]
15	1,540.236
20	1,540.313
25	1,540.383
30	1,540.447
35	1,540.508
40	1,540.567
45	1,540.619

The obtained interpolation lines and the seven pairs $(\bar{\lambda} - \bar{T})$ used with *polyfit* function are shown in Fig. 7.5.

Fig. 7.6 shows the linearity error of the FBG B calibration line, that is the difference between the temperature measured by the reference sensor and that obtained from the interpolation line.

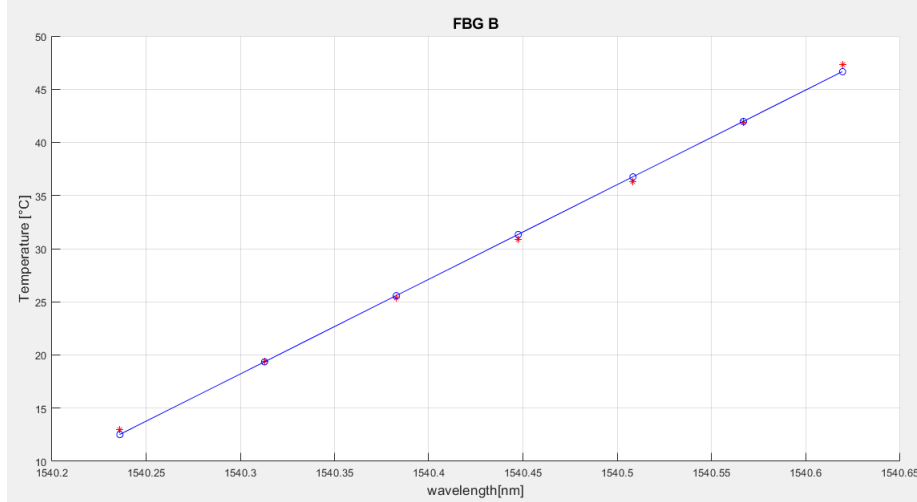


Figure 7.5: FBG B calibration line.

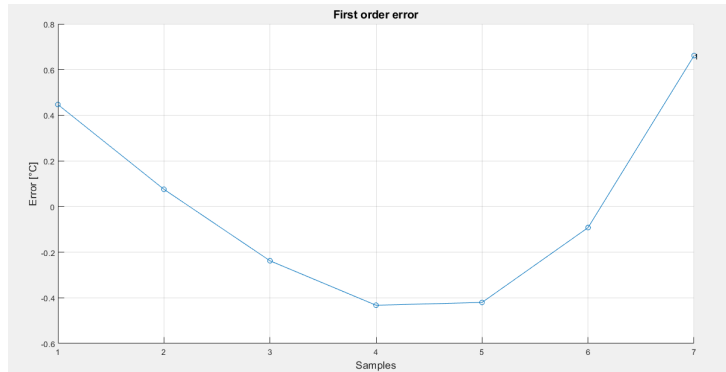


Figure 7.6: The linearity error of the FBG B calibration line.

The table 7.3 report the values of k_T , λ_0 and the temperature estimation error of the calibration line.

Table 7.3: Parameters of the FBG B calibration line.

$k_T = 11.234 \text{ pm } ^\circ\text{C}^{-1}$
$\lambda_0 = 1,540.095 \text{ nm}$
temperature estimation error = $0.661 \text{ } ^\circ\text{C}$

Below are reported the results of FBG A characterisation.

Fig. 7.7 shows the temperature profile set on the THORLABS breadboard and the temperature profile measured with the reference sensor (Pt1,000) during the characterisation of FBG A.

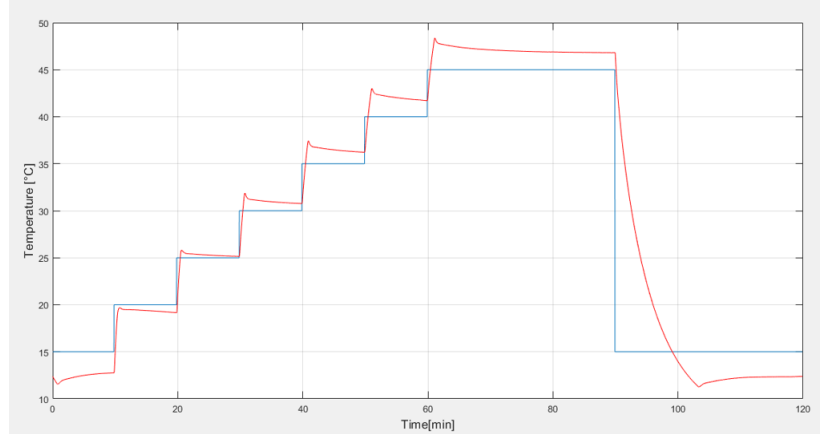


Figure 7.7: The temperature profile set on the THORLABS breadboard in blue and the temperature profile measured with the reference sensor in red.

Tab 7.4 reports the set temperature on the THORLABS breadboard and the real temperature measured with the reference sensor (Pt1,000) during the characterisation of FBG A.

Table 7.4: Set and real temperature during the trial.

Set temperature [°C]	Real temperature [°C]
15	12.756
20	19.169
25	25.151
30	30.765
35	36.223
40	41.717
45	46.818

Fig. 7.8 shows the Bragg wavelength profile of the grating during the trial. The figure also highlights the seven steps considered for the characterisation of FBG A.

The average Bragg wavelength values of FBG A during the seven temperature steps are shown in Tab. 7.5.

The obtained interpolation lines and the seven pairs $(\bar{\lambda} - \bar{T})$ used with *polyfit* function are shown in Fig. 7.9.

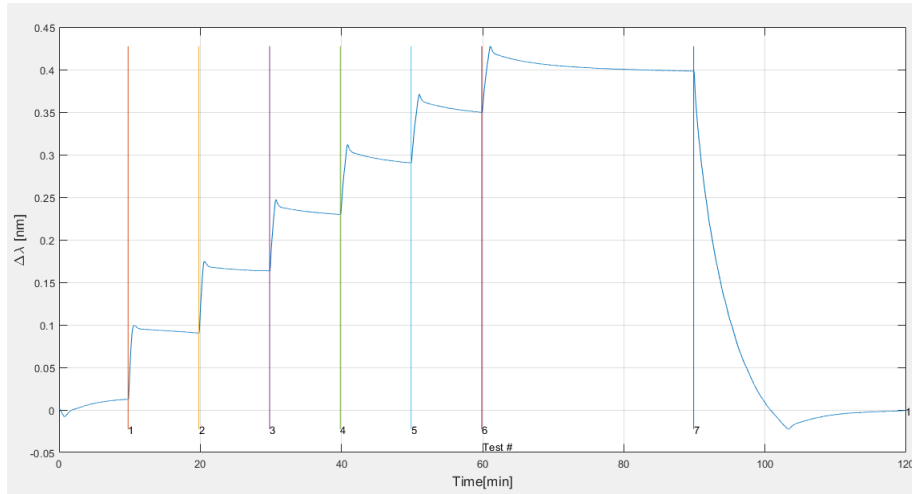


Figure 7.8: The Bragg wavelength profile of the grating A during the trial.

Table 7.5: Set temperature and average Bragg wavelength in the seven steps.

Set temperature [°C]	Average Bragg wavelength of FBG A [nm]
15	1,550.027
20	1,550.348
25	1,550.421
30	1,550.488
35	1,550.548
40	1,550.608
45	1,550.656

Fig. 7.10 shows the linearity error of the FBG A calibration line, that is the difference between the temperature measured by the reference sensor and that obtained from the interpolation line.

The table 7.6 report the values of k_T , λ_0 and the temperature estimation error of the calibration line.

Table 7.6: Parameters of the FBG A calibration line.

$k_T = 11.400 \text{ pm } ^\circ\text{C}^{-1}$
$\lambda_0 = 1,550.131 \text{ nm}$
temperature estimation error = 0.743 °C

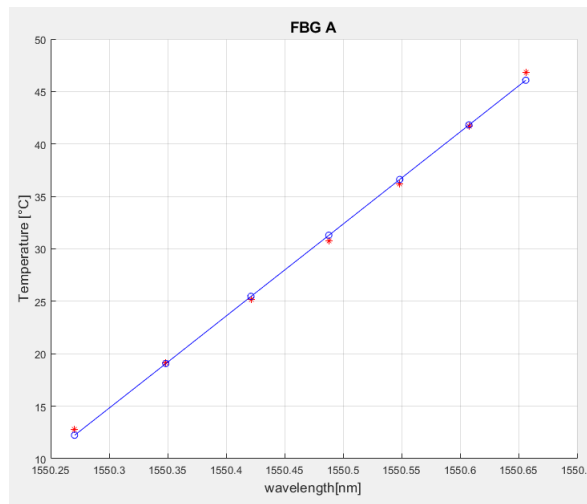


Figure 7.9: FBG A calibration line.

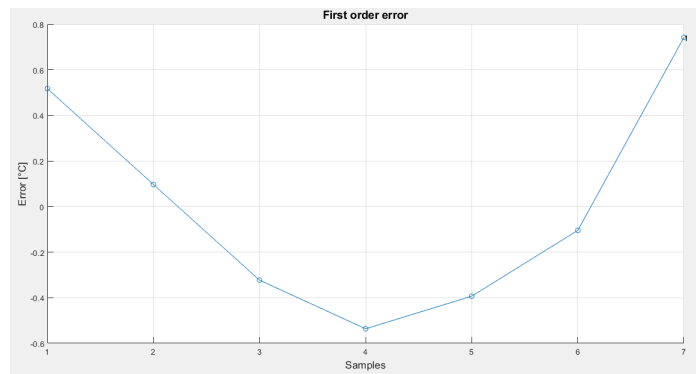


Figure 7.10: The linearity error of the FBG A calibration line.

7.1.3 Observations

The temperature sensitivity values, k_T , of FBG A and FBG B, obtained from the characterisations conducted, are consistent with the value indicated in the literature [26].

For both gratings, the temperature estimation errors are less than a degree.

7.2 Characterisation of the sensor with respect to temperature

Once the two fibres have been attached to the cantilever, as described in section 6.2.1, their characterisation was redone. The linear relationship that links the Bragg wavelength of the gratings to temperature remains the one described in the equation 7.1.

However, the sensor is not shaped to fit into the hole of the PLA cube used in the previous characterisation setup. For this reason, the characterisation of the sensor was conducted in a climate chamber.

7.2.1 Setup and instrumentation

The setup is shown in Fig. 7.11.

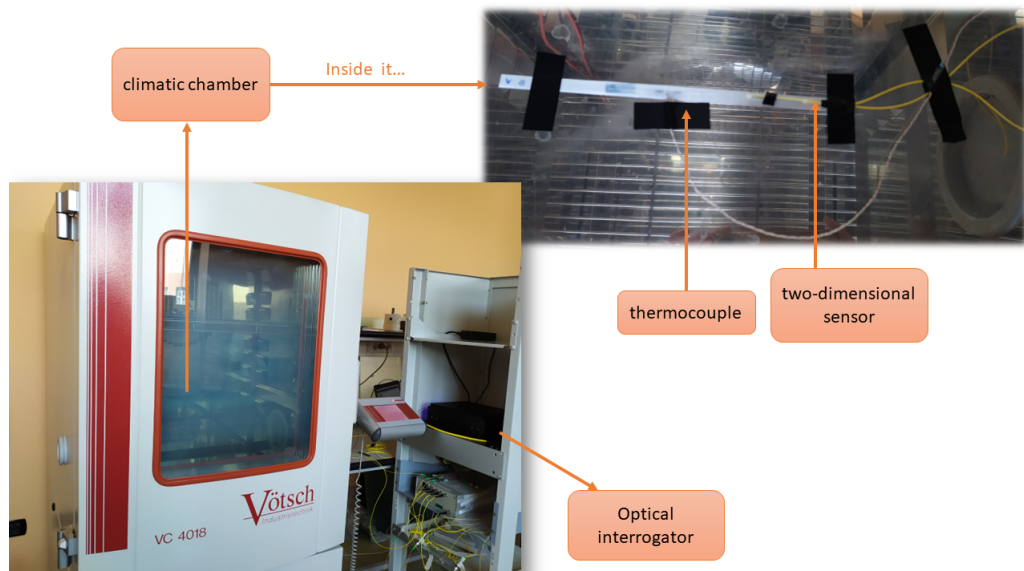


Figure 7.11: The setup for the trial.

The instruments used in this case are:

- optical interrogator Micron Optics HYPERION si155 and the related software Enlight;
- Climatic chamber Vötsch VC 4018;
- National instrument T-type exposed-junction thermocouple with the measurement device NI USB-TC01: the USB port powers up the device and transfers

data to the self-launched software for graphical view and data saving.

The two FBG of the two-dimensional sensor are connected to channels 4 and 3 of their optical interrogator. The latter is controlled, via an Ethernet connection, by a PC equipped with Enlight software, which allows data to be recorded with an acquisition rate of 1 kHz and saved in a text file. The file is structured in rows, each representing an acquisition sample and containing the sampling time, the number of FBGs detected on each channel of the optical interrogator and the value of the wavelengths recorded for each FBG detected.

In the climate chamber, the set temperature is reached and maintained by the air flow generated by a big fan. In order to prevent the air flow from moving the two-dimensional sensor, causing unwanted strain effects, the sensor is fixed to the lower shelf of the chamber with adhesive tape.

Then, the thermocouple is fixed to the lower shelf too, close to the sensitive part of the two-dimensional sensor. The thermocouple is connected to the related reading software via the PC's USB port and its data are recorded with an acquisition rate of 1 Hz.

During the characterisation, the temperature in the climate chamber changes following a stepped profile. The climate chamber is turned on and the temperature values of each step are set and changed manually every 20 min. The temperature is subsequently set to: 20 °C, 25 °C, 30 °C, 35 °C, 40 °C and after it returns back to 20 °C.

The data were then processed by Matlab code. The temperature measured by the thermocouple and the Bragg wavelength of the gratings to be characterised follow the step profile of the temperature in the climate chamber.

For each step, a window of 100 samples (approximately one and a half minutes) is selected in which the temperature measured by the thermocouple remains stable. In each window, the average of the temperature values measured by the thermocouple and the average of the Bragg wavelength values of the sensor gratings (the gratings previously labelled as grating A and grating B) are calculated. The profile used to characterise the two-dimensional sensor has six steps, so six pairs $(\bar{\lambda}_A - \bar{T})$ and six pairs $(\bar{\lambda}_B - \bar{T})$ are obtained. These are given as input to the *polyfit* function. With this function, requiring a first-order polynomial, the coefficients of the sensor gratings calibration lines (the calibration line of FBG A and the calibration line of FBG B), k_T and λ_0 are obtained.

For both the calibration lines, the temperature estimation error is calculated as the maximum difference (in absolute value) between the temperature measured by the reference sensor (thermocouple) and that obtained from the interpolation line,

during the heating phase (i.e. the first five steps). The temperature error obtained during the cooling phase until the initial temperature (i.e. the transition from the fifth to the last step) is the hysteresis.

7.2.2 Results

Fig. 7.12 shows the temperature profile measured with the reference sensor (thermocouple) in the climatic chamber during the characterisation of the two-dimensional sensor. While Fig. 7.13 shows the variation of the Bragg wavelength of the gratings A and B during the test. In both figures, the seven windows selected for the characterisation of the two-dimensional sensor are also highlighted.

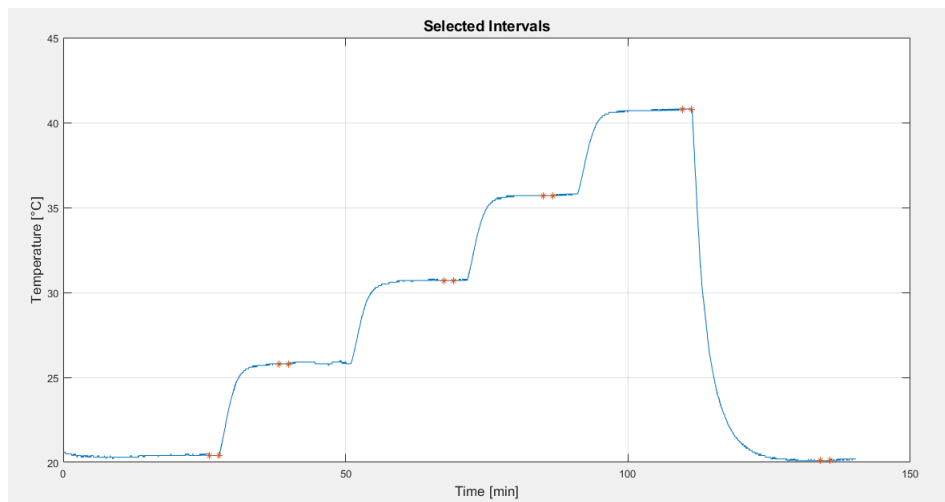


Figure 7.12: The temperature profile measured with the thermocouple. The stars indicate the start and end points of the six selected windows.

Tab 7.7 reports the set temperature in the climatic chamber and the real temperature measured with the reference sensor (thermocouple) during the characterisation of the two-dimensional sensor.

Table 7.7: Set and real temperature during the trial.

Set temperature [°C]	Real temperature [°C]
20	20.4
25	25.8
30	30.7
35	35.7
40	40.8
20	20.1

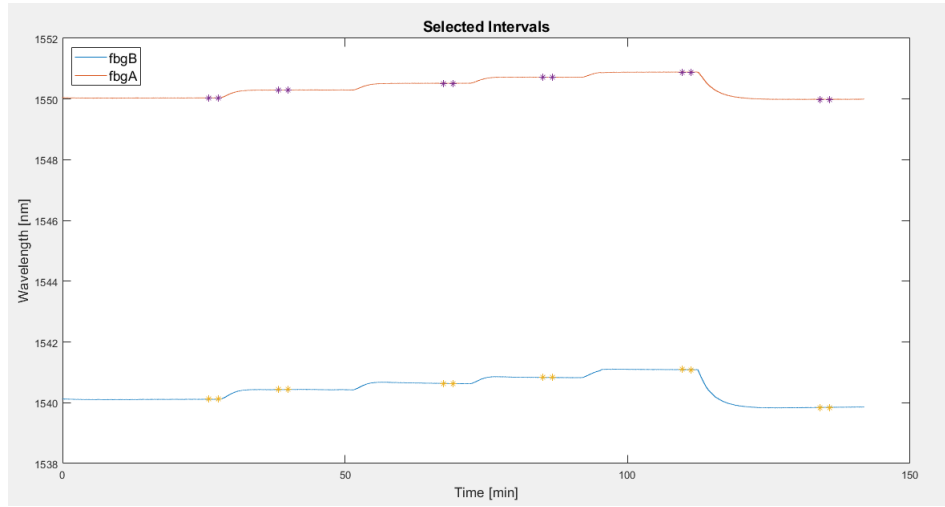


Figure 7.13: The Bragg wavelength variation for the grating A (red) and B (blue) during the test. The stars indicate the start and end points of the six selected windows.

The average Bragg wavelength values of FBG A and FBG B during the six temperature steps are shown in Tab. 7.8.

Table 7.8: Set temperature and average Bragg wavelengths in the six steps.

Set temperature [°C]	FBG A [nm]	FBG B [nm]
20	1,540.114	1,550.039
25	1,540.433	1,550.296
30	1,540.634	1,550.519
35	1,540.831	1,550.719
40	1,541.089	1,550.888
20	1,539.847	1,549.990

Fig. 7.14 compares the temperature trend measured by the gratings A and B with that measured by the thermocouple.

Fig. 7.15 shows the linearity error of FBG A and FBG B calibration lines, calculated as the difference between the temperature measured by the reference sensor and that obtained from the interpolation line in the six steps.

The tables 7.9 and 7.10 report the values of k_T , λ_0 , the temperature estimation error and the hysteresis of both calibration lines.

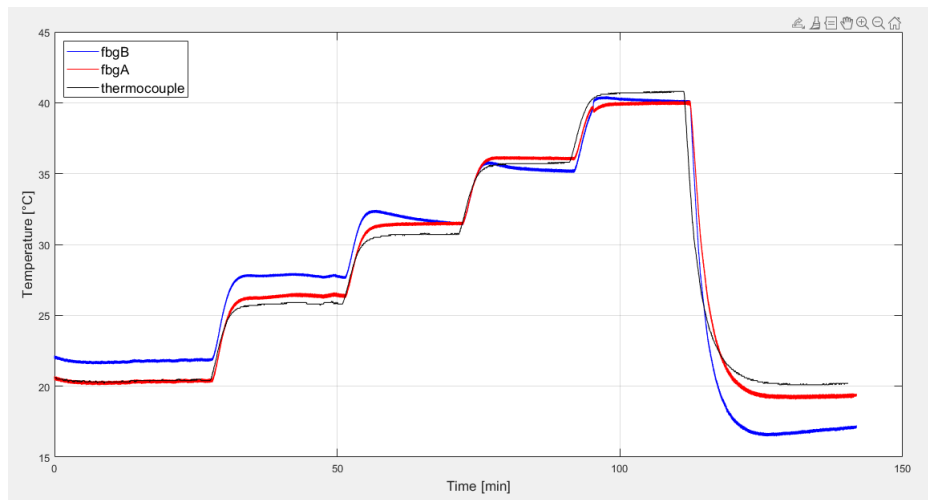


Figure 7.14: The temperature profile measured with the thermocouple (black), with the grating A (red) and the gratings B (blue).

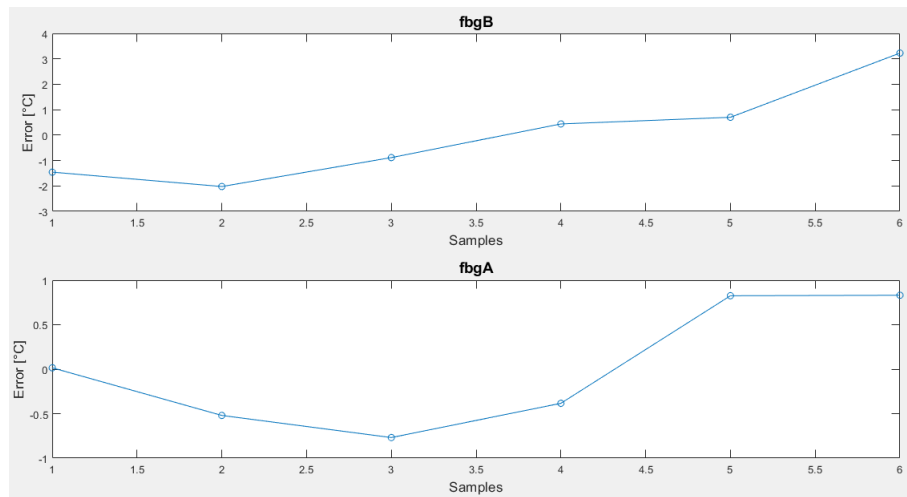


Figure 7.15: The linearity error of the FBG B (above) and of the FBG A (below) calibration lines.

Table 7.9: Parameters of the FBG A calibration line.

$k_T = 43.339 \text{ pm } ^\circ\text{C}^{-1}$
$\lambda_0 = 1,549.155 \text{ nm}$
temperature estimation error = $0.826 \text{ } ^\circ\text{C}$
hysteresis = $0.831 \text{ } ^\circ\text{C}$

Table 7.10: Parameters of the FBG B calibration line.

$k_T = 53.492 \text{ pm } ^\circ\text{C}^{-1}$
$\lambda_0 = 1,538.945 \text{ nm}$
temperature estimation error = $2.024 \text{ } ^\circ\text{C}$
hysteresis = $3.227 \text{ } ^\circ\text{C}$

7.2.3 Observations

In Fig. 7.14, it can be seen from the figure that FBG A and FBG B read slightly different temperature values. This deviation is more pronounced at low temperatures, while at high temperatures it is less and the two FBGs read an almost equal temperature. The temperature profile measured with FBG A deviates less from the real temperature profile (the one measured with the thermocouple) than that measured with FBG B.

This is also confirmed by the value of the temperature estimation error (in Tab. 7.9 and Tab. 7.10), which is $0.826 \text{ } ^\circ\text{C}$ for FBG A, while it is $2.024 \text{ } ^\circ\text{C}$ for FBG B. The temperature estimation error values for the two gratings are lower than their respective hysteresis values, as expected.

The temperature sensitivity values, k_T , of FBG A and FBG B, obtained from the characterisations conducted, are slightly higher than the value indicated in the literature [26]. This could be an effect of the used resin to glue the two fibres to the cantilever.

7.3 Temperature measurement when the sensor is bent

At this point, both fibres embedded in the sensor (FBG A and FBG B) were characterised with respect to both strain (section 6.2) and temperature (section 7.2).

The sensor can, therefore, be used to distinguish and separate the signal related to a change in two-dimensional strain from that related to a change in temperature.

This section describes a test in which the two-dimensional sensor is used to simultaneously measure temperature and curvature to which it is subjected.

Since there were no instruments available to simulate a simultaneous change in temperature and curvature, during the test described here, the sensor is subjected to the effect of constant curvature and variable temperature.

7.3.1 Separation of temperature and strain

In the previous chapters, it is demonstrated that when the sensor is bent, the two gratings are subjected to an opposite strain effect; whereas when the sensor is exposed to a change in temperature, the effect on the two gratings is the same. Therefore, if the sensor is subjected to a simultaneous change in strain and temperature, the following relationships apply for the two gratings (FBG A and FBG B):

$$\begin{aligned} T_B &= T_A = T \\ \varepsilon_B &= -\varepsilon_A = \varepsilon \end{aligned} \quad (7.2)$$

In general, when an FBG is subjected to a simultaneous change in strain and temperature, assuming that the shifts of the wavelength in strain and temperature are linear, its Bragg wavelength will vary according to the relationship:

$$\Delta\lambda = k_\varepsilon \cdot \Delta\varepsilon + k_T \cdot \Delta T \quad [39] \quad (7.3)$$

Using this relationship to describe the behaviour of FBG A and FBG B in the sensor, the following system of two equations is obtained:

$$\begin{cases} \Delta\lambda_A = k_{\varepsilon,A} \cdot \Delta\varepsilon_A + k_{T,A} \cdot \Delta T_A \\ \Delta\lambda_B = k_{\varepsilon,B} \cdot \Delta\varepsilon_B + k_{T,B} \cdot \Delta T_B \end{cases} \quad (7.4)$$

Considering the change in temperature and strain from an initial condition in which both temperature and strain are zero ($T = 0, \varepsilon = 0$), the system becomes:

$$\begin{cases} \lambda_A - \lambda_{0,A} = k_{\varepsilon,A} \cdot \varepsilon_A + k_{T,A} \cdot T_A \\ \lambda_B - \lambda_{0,B} = k_{\varepsilon,B} \cdot \varepsilon_B + k_{T,B} \cdot T_B \end{cases} \quad (7.5)$$

Using the relationships 7.2, the system is further simplified:

$$\begin{cases} \lambda_A - \lambda_{0,A} = k_{\varepsilon,A} \cdot (-\varepsilon) + k_{T,A} \cdot T \\ \lambda_B - \lambda_{0,B} = k_{\varepsilon,B} \cdot \varepsilon + k_{T,B} \cdot T \end{cases} \quad (7.6)$$

Since the sensor can only be used in the case of two-dimensional deformation, we can substitute the relations between deformation and curvature described in the equation 6.3 into the system 7.6:

$$\begin{cases} \lambda_A - \lambda_{0,A} = k_{C,A} \cdot (-C) + k_{T,A} \cdot T \\ \lambda_B - \lambda_{0,B} = k_{C,B} \cdot C + k_{T,B} \cdot T \end{cases} \quad (7.7)$$

where k_C is the curvature sensitivity ($k_C = k_\epsilon \cdot \frac{s}{2}$).

This leads to a system of two equations in two unknowns that can be solved. The system solution is:

$$\begin{cases} C = \frac{k_{T,A} \cdot \Delta\lambda_B - k_{T,B} \cdot \Delta\lambda_A}{k_{T,A} \cdot k_{C,B} + k_{T,B} \cdot k_{C,A}} \\ T = \frac{\Delta\lambda_A + k_{C,A} \cdot C}{k_{T,A}} \end{cases} \quad (7.8)$$

The relationship 7.8 allows the curvature and temperature to be measured at any time.

7.3.2 Setup and instrumentation

The instruments used in this case are:

- optical interrogator Micron Optics HYPERION si155 and the related software Enlight;
- Climatic chamber Vötsch VC 4018;
- National instrument T-type exposed-junction thermocouple with the measurement device NI USB-TC01: the USB port powers up the device and transfers data to the self-launched software for graphical view and data saving;
- calibration board.

In order to simulate the temperature variation, the test was conducted in a climatic chamber.

The temperature in the climatic chamber changes following a stepped profile in which the temperature values are changed every 20 minutes. The temperature is subsequently set to: 20 °C, 25 °C, 30 °C and after it returns back to 20 °C.

For keeping the sensor bent throughout the test, the calibration board was placed in the climatic chamber.

The two-dimensional sensor is attached to the curve 4 of the calibration board, with a radius of 92.5 mm.

Then, a thermocouple is fixed on the calibration board too, close to the sensitive

part of the two-dimensional sensor (Fig. 7.16). The thermocouple is connected to the related reading software via the PC USB port and its data are recorded with an acquisition rate of 1 Hz.

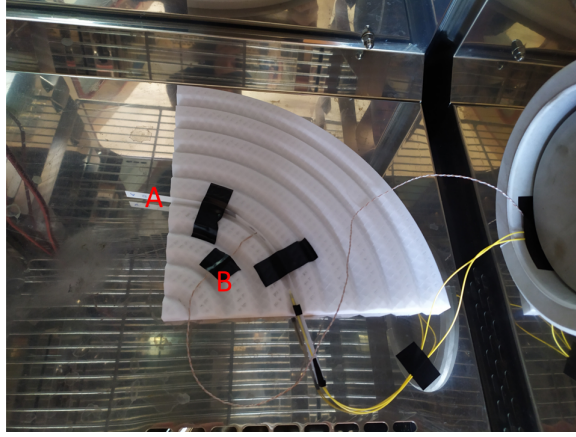


Figure 7.16: A) the two-dimensional sensor; B) the thermocouple.

As in the previous setup (section 7.2), the two FBGs of the two-dimensional sensor are connected to channels 4 and 3 of their optical interrogator. The latter is controlled, via an Ethernet connection, by a PC equipped with Enlight software, which allows data to be recorded with an acquisition rate of 1 kHz and saved in a text file. The file is structured in rows, each representing an acquisition sample and containing the sampling time, the number of FBGs detected on each channel of the optical interrogator and the value of the wavelengths recorded for each FBG detected.

The data were then processed by Matlab code.

Temperature and curvature are calculated for each sample acquired using eq. 7.8 and the parameters of the calibration straight lines ($\lambda_{0,A}$, $\lambda_{0,B}$, $k_{\varepsilon,A}$, $k_{\varepsilon,B}$, $k_{T,A}$, $k_{T,B}$) obtained during the sensor characterisations described above.

In order to assess the estimation errors, windows are selected in which temperature and curvature are constant. The temperature follows a step profile as in the previous test (section 7.2). Therefore, windows are selected on these steps. For each step, a window of 100 samples (approximately one and a half minutes) is selected in which the temperature measured by the thermocouple remains stable.

In each window, the average of the temperature values measured by the thermocouple and the average of the temperature values measured by the two-dimensional sensor are calculated. The maximum temperature estimation error is calculated as the maximum difference (in absolute value) between the temperature measured

by the reference sensor (thermocouple) and that measured by the two-dimensional sensor in these four windows.

In these same windows, the curvature estimation error is calculated as the maximum difference (in absolute value) between the real curve (i.e., that of the breadboard) and the curvature measured by the two-dimensional sensor (i.e., the average of the curvature values in each window).

7.3.3 Results

Fig. 7.17 shows the temperature profile measured with the reference sensor (thermocouple) in the climatic chamber during this test, while Fig. 7.18 shows the Bragg wavelengths of the gratings A and B.

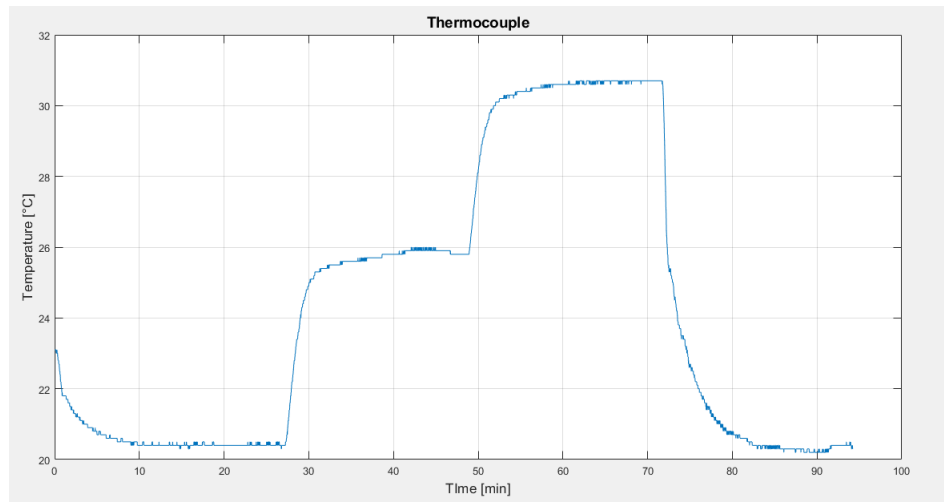


Figure 7.17: The temperature profile measured with the thermocouple.

Fig. 7.19 compares the temperature trend measured by the two-dimensional sensor with that measured by the thermocouple.

Fig. 7.20 shows the temperature estimation error of the two-dimensional sensor, calculated as the difference between the temperature measured by the reference sensor and that measured by the two-dimensional sensor in the four windows considered.

Fig. 7.21 compares the curvature measured by the two-dimensional sensor with the real one.

Fig. 7.22 shows the curvature estimation error of the two-dimensional sensor, calculated as the difference between the real curvature and that measured by the two-dimensional sensor in the four windows considered.

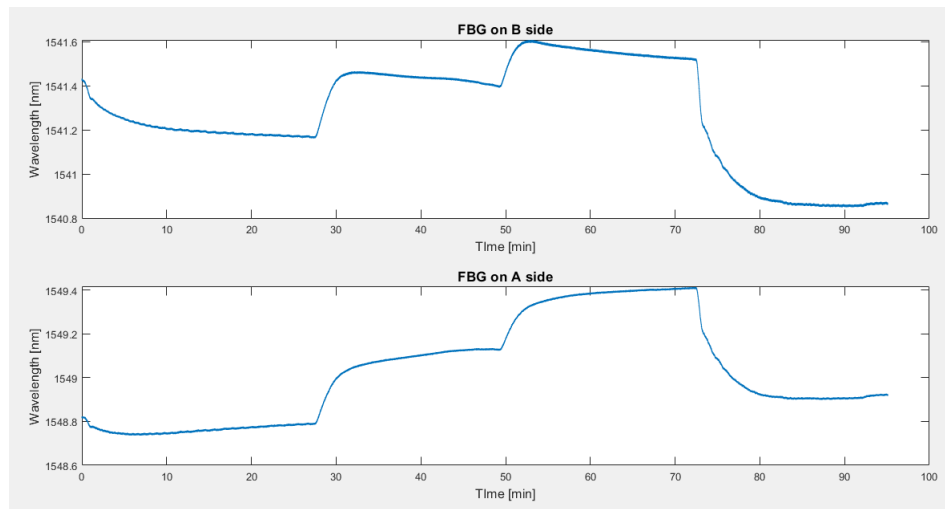


Figure 7.18: The Bragg wavelength changes for the gratings B (above) and A (below).

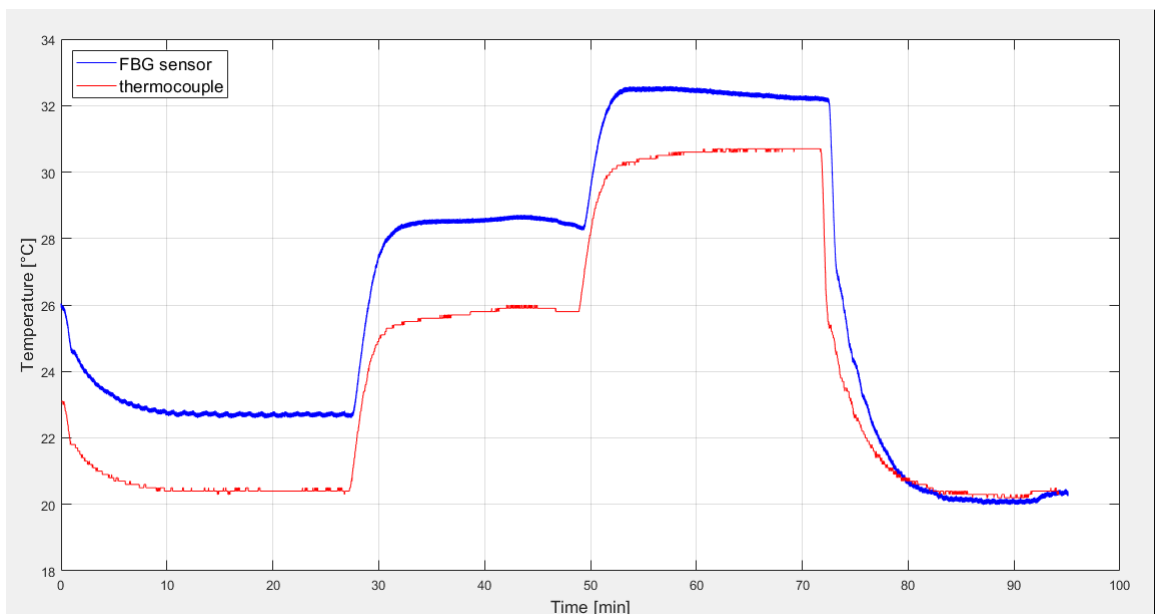


Figure 7.19: Comparison of the temperature profile measured with the thermocouple (red) and with the two-dimensional sensor (blue).

Table 7.11 reports the values of the estimation errors of the two-dimensional sensor.

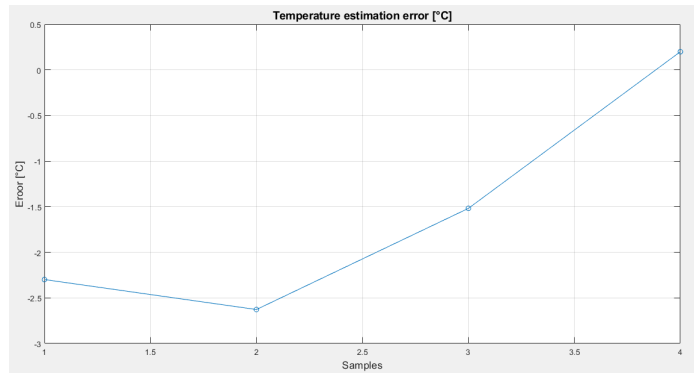


Figure 7.20: The temperature estimation error of the two-dimensional sensor.

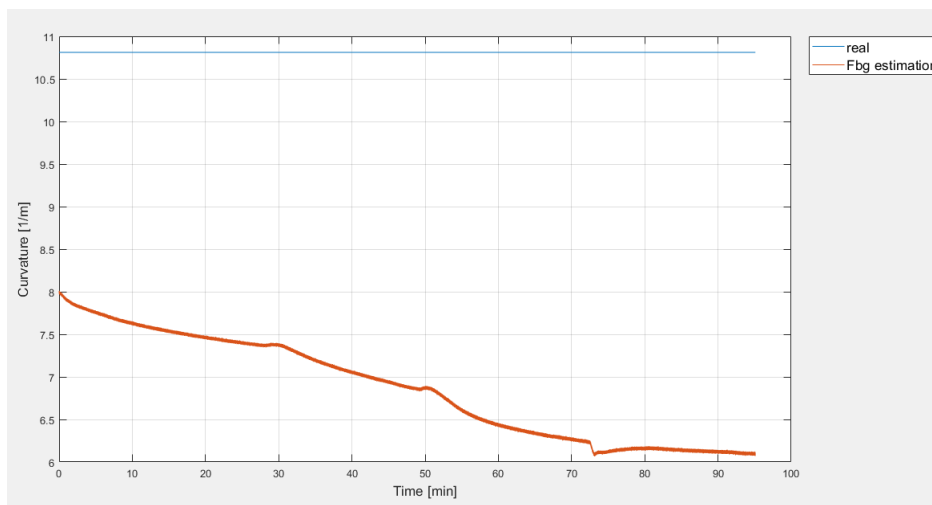


Figure 7.21: Comparison of the curvature profile measured with the two-dimensional sensor (red) with the real curvature (blue).

Table 7.11: Estimation errors.

maximum temperature estimation error = 2.628 °C
maximum curvature estimation error = 4.701,2 m ⁻¹

7.3.4 Observations

Observing the curves in Fig. 7.19, it can be seen that the temperature measured by the two-dimensional sensor follows the real temperature profile (the one measured by the thermocouple). During the heating phase, however, the temperature measured by the two-dimensional sensor exhibits an offset error which leads to an overestimation of the temperature of a few degrees. During the cooling phase, this

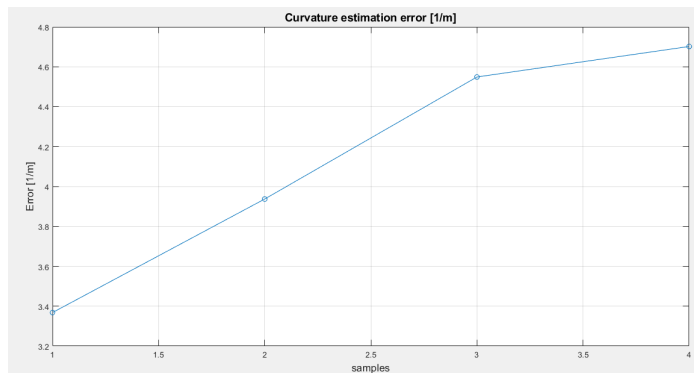


Figure 7.22: The curvature estimation error of the two-dimensional sensor.

error tends to decrease instead of increase as one would expect.

The value of the curvature measured by the two-dimensional sensor, on the other hand, does not follow the profile of the real curvature. In Fig. 7.21 it can be seen that also in this case, there is an offset error which leads the sensor to underestimate the curvature. The curvature estimation error, however, does not remain constant but tends to increase over time. Only in the last phase, the cooling phase, the error remains almost constant.

Chapter 8

The first steps towards three-dimensional strain detection

In the previous chapters, the analysis was described considering the case of two-dimensional movement.

During a laser lipolysis operation, however, the laser source is moved in the tissue in any direction. Consequently, FBG sensors undergo both bending and torsion strain. The sensor used in the previous analysis is not suitable for this case study. In fact, the previous sensor consisted of two optical fibres which, being fixed on a cantilever, were forced to undergo only bending strains.

Therefore, in order to continue the analysis, it is necessary to modify the structure of the sensor.

8.1 Sensor prototyping

8.1.1 First attempt: fixing only the ends of the gratings to the substrate

The structure designed for the sensor is always based on a combination of Fibre Bragg Grating (FBG) sensors positioned differently around a substrate. In this way, the strain experienced by each grating is different and depends on its position, while the temperature effect remains the same. This makes it possible to separate the two effects.

However, in the three-dimensional case, a further distinction must be made between bending and torsion strains. To be able to do this, two FBG sensors are no longer sufficient, but at least three are required. In this thesis, a configuration using four FBG sensors was chosen.

The substrate for the optical fibres was also changed. Something was chosen that could better approximate the shape of the cannula used for laser lipolysis. In order to make the sensor easier to realise, the chosen substrate is slightly larger than that of a laser lipolysis cannula and its cross-section is not circular. The selected substrate is a nylon wire with a square cross-section of 3 mm side. Choosing a wire with a larger square cross-section allows the fibres to be positioned around the substrate with greater facility and precision.

An optical fibre was fixed on each side of the substrate. Specifically, four SMF-28 Ultra optical fibres were used, all having a single Bragg grating with a length of 2 mm and a Bragg wavelength of 1,550 nm. The four fibres were bonded to the substrate using the two-component epoxy glue *Pattex*. To avoid compromising the sensitivity of the gratings to deformation, the glue was applied to the two ends of each grating, avoiding applying it on top of them, as illustrated in Fig. 8.1.

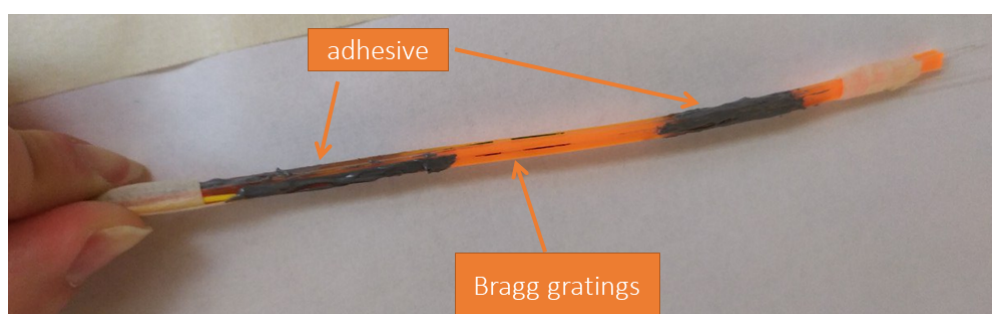


Figure 8.1: The gratings are bonded only at the ends.

Once the fibres were bonded, the manufactured system was coated with a heat-shrink to better protect and secure the optical fibres to the substrate (Fig. 8.2).

Sensor sensitivity evaluation

Once realised, the sensor was tested to verify that it functioned properly. Initially, the sensitivity of the sensor to bending was assessed. For this purpose, the sensor was bent within the bending grooves of the calibration board used in the previous tests (6.1.3).

Since the four FBG sensors are positioned on each face of the substrate, it is expected to observe a change in the Bragg wavelength only in the two gratings

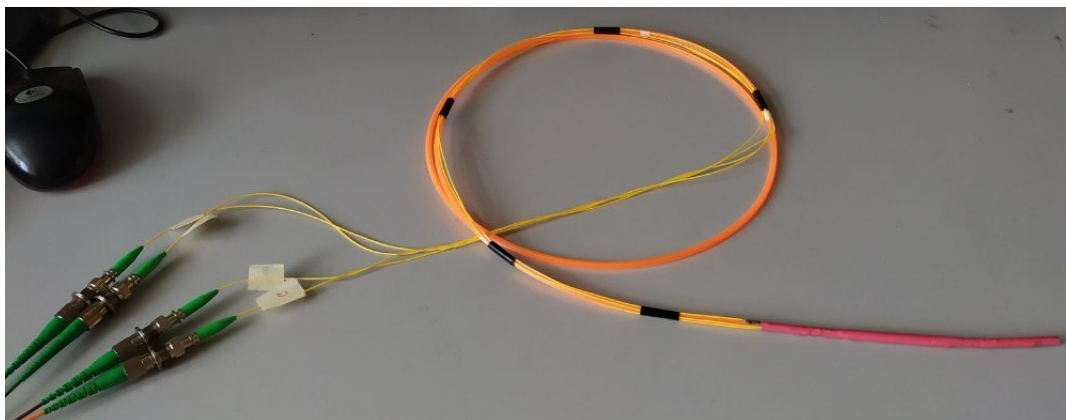


Figure 8.2: The final sensor, coated with red heat-shrink tubing.

positioned on the two faces subject to bending strain.

What was observed instead is that only one of the four FBG sensors is affected by the bending effect and it is always the one subject to tension force.

For explanatory purposes, an example of one of the four sensor gratings during a deformation test is shown. In Fig. 8.3, the top shows the grating peak when it is not subjected to strain, while the bottom shows the same peak when the grating is subjected to tension by bending it in one of the bending grooves. In the figure, it is evident how the grating peak shifts towards longer wavelength values due to the effect of tension force.

In Fig. 8.4, the peak conditions in the top image are the same as before, while the bottom image shows the peak when the grating is subjected to compression. In this case, the grating should shift to shorter wavelengths, but as can be seen in figure 8.4, the peak remains unchanged.

This behaviour is probably related to the method used to attach the fibres to the substrate. The four FBG sensors were glued to the substrate by applying glue only to the ends of each grating, rather than along their entire length.

A grating on a face subject to tension is squeezed between the face of the substrate and the coating layer. Therefore, even if the grating is not bonded to the substrate along its entire length, it still adheres to the face of the substrate and undergoes the same deformation.

When a grating is on a face subject to compression, however, a gap is created between the substrate and the coating layer. The lattice, having a larger movement space, is no longer forced to adhere to the substrate face and, consequently, does not undergo the same deformation.



Figure 8.3: Effect of traction on one of the sensor gratings.

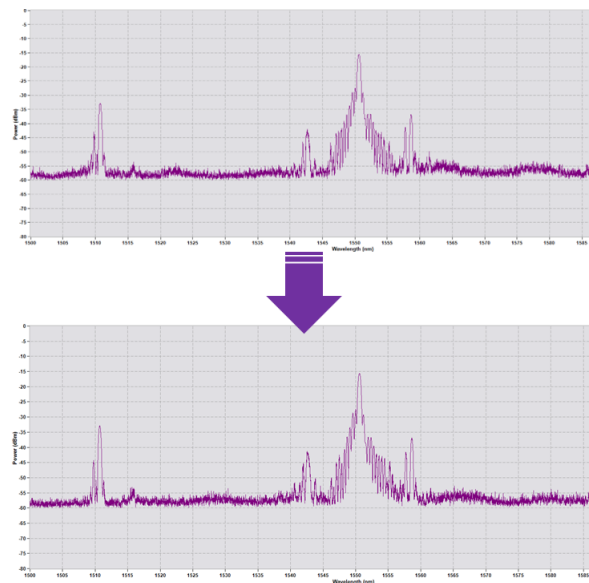


Figure 8.4: Effect of compression on one of the sensor gratings.

8.1.2 Second attempt: embedding the gratings in the silicone substrate

Since the problems encountered in the first prototype appear to be related to the method of attaching the fibres to the substrate, alternatives to this method were

analysed and evaluated.

A second prototype was constructed, incorporating four optical fibres into a silicon substrate. The four optical fibres used to construct this sensor have the same characteristics as those used in the previous prototype. The shape of the sensor remains unchanged, but the dimensions are larger: the side of the square section measures approximately 1 cm.

To construct this prototype, two-component liquid silicone was poured in two separate steps into a parallelepiped mould. Initially, one fibre was placed in the centre of the bottom face of the mould, after which silicone was poured in, filling the mould halfway. Subsequently, two more fibres were placed on the surface of the silicone. After a short waiting period to allow the silicone to harden slightly, more silicone was poured into the mould until it was completely filled and finally, a further fibre was placed on the surface of the mould. In this way, a silicone substrate was created incorporating four optical fibres positioned in the centre of each of its faces (Fig. 8.5).



Figure 8.5: Silicone prototype.

After complete drying, the silicone substrate was removed from the mould and its sensitivity to bending was tested. Unfortunately, during this step, it was found that some of the fibres within the substrate had become damaged or broken. The probable cause of this problem is the high flexibility of the silicone combined with the choice of a very elongated shape for the sensor. This causes the fibres to be subjected to mechanical stresses that exceed their breaking point.

8.1.3 Third attempt: attachment of the gratings to a substrate along their entire length

Considering the problems encountered in using silicon, it was decided to continue the study using the nylon wire as a substrate with which the first prototype was made, but modifying the technique for attaching the optical fibres. A further

prototyping attempt was conducted, this time pasting the gratings to the substrate along their entire length (Fig. 8.6). The four FBG sensors were attached to the nylon wire using Norland Optical Adhesive 68 resin.



Figure 8.6: The sensor obtained pasting the gratings to the substrate along their entire length.

8.2 Sensor sensitivity evaluation

Once realised, this sensor was tested, like the previous ones, in order to assess its sensitivity to bending.

8.2.1 Setup and instrumentation

To do this, the sensor was placed on a metal board and, by wedging it with three screws, was forced to assume a predefined curvature as shown in Fig. 8.7.

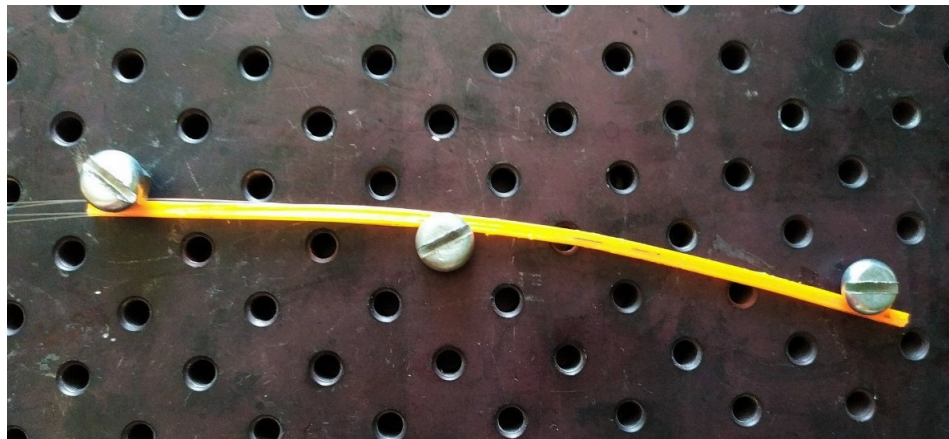


Figure 8.7: setup for sensor curvature sensitivity evaluation tests.

The sensor was tested by bending it between the screws in the same way but varying the direction of bending between tests. In order not to create confusion during the tests, the sensor faces were labelled clockwise with the letters 'A', 'B', 'C' and 'D'.

The sensor was bent in the direction of each of its four faces (directions A, B, C and D) and in the four intermediate directions between two of them (directions AB, BC, CD and DA), for a total of eight bending trials.

The four FBG sensors are connected to the optical interrogator Micron Optics HYPERION si155 and the data of each test is acquired with Enlight software for approximately 5 minutes. Thereafter, the wavelengths of the four gratings acquired during each test were averaged and compared with their respective characteristic wavelengths to verify that the four sensors were correctly affected by the bending strains.

8.2.2 Results and observations

By bending the sensor in the direction of one of the four faces of its substrate, the grating positioned on that face undergoes a compressive strain, while the one positioned on the opposite face undergoes a tensile strain. Indeed, there is a shift towards shorter wavelengths of the grating placed on the face in compression, a shift towards longer wavelengths of the grating placed on the face in tension, while the position of the other two sensor gratings remain almost unchanged. Tab. 8.1 shows the average wavelength values assumed by the four sensor gratings when it is bent in the direction of each of its faces.

Table 8.1: The average wavelength values assumed by the sensor gratings when it is bent.

Bending direction	A [nm]	B [nm]	C [nm]	D [nm]
none	1,549.397	1,549.885	1,548.942	1,549.270
towards A	1,547.075	1,549.896	1,551.115	1,549.567
towards B	1,548.637	1,548.328	1,549.340	1,551.078
towards C	1,550.726	1,549.351	1,547.734	1,549.494
towards D	1,549.155	1,551.487	1,549.567	1,547.313

on the other hand, when the sensor is bent in an intermediate direction between two of its faces, all four gratings shift. The gratings on the two faces in compression move towards shorter wavelengths, while those on the faces in tension move towards longer wavelengths. Tab. 8.2 shows the average wavelength values assumed by the four gratings of the sensor when it is bent in each of the intermediate directions between its faces.

The sensor, therefore, appears to be sensitive to bending in all directions of three-dimensional space and, therefore, suitable for the purpose of this thesis.

For this reason, it was decided to continue the analysis using the latter prototype.

Table 8.2: The average wavelength values assumed by the sensor gratings when it is bent.

Bending direction	A [nm]	B [nm]	C [nm]	D [nm]
none	1,549.397	1,549.885	1,548.942	1,549.270
towards AB	1,547.426	1,548.742	1,550.339	1,550.079
towards BC	1,549.960	1,547.696	1,547.733	1,550.926
towards CD	1,550.615	1,550.577	1,547.461	1,546.621
towards DA	1,547.247	1,550.994	1,551.056	1,547.345

8.3 Detection of sensor movement direction

Previous evaluation tests have shown that the sensor can provide a qualitative assessment of the direction of movement over time.

Indeed, during these tests, it was possible to distinguish eight different directions of movement, based on which gratings underwent tensile deformation and which underwent compressive deformation.

Assuming, therefore, that the sensor is moved in any direction in a range of 360° , the data obtained in the previous tests allow discrimination of the sensor movement direction with a resolution of 45° .

Based on these observations, a Matlab code was written with which it is possible to determine the displacement direction of the sensor with a resolution of 45° . Specifically, a direct communication between the Micron Optics HYPERION si155 optical interrogator and the Matlab software was exploited in order to acquire the Bragg wavelengths of the four sensor gratings in real-time. Subsequently, the acquired wavelengths are compared in the code with the characteristic wavelengths of each grating in order to identify which of them have shifted to shorter wavelengths, which to longer wavelengths, and which have not undergone significant peak shifts. Based on this assessment, the sensor direction of movement is determined. This is finally provided to the user through an explanatory graph in which the direction is represented as a green dot moving along a circumference. Fig. 8.8 shows some examples of the graph that the code provides at different instants of time.

8.3.1 Observations

These tests confirmed that the sensor is able to correctly assess the direction of movement when it is bent.

It is confirmed that each of the four gratings can correctly detect the bending of the face of the substrate to which it has been pasted

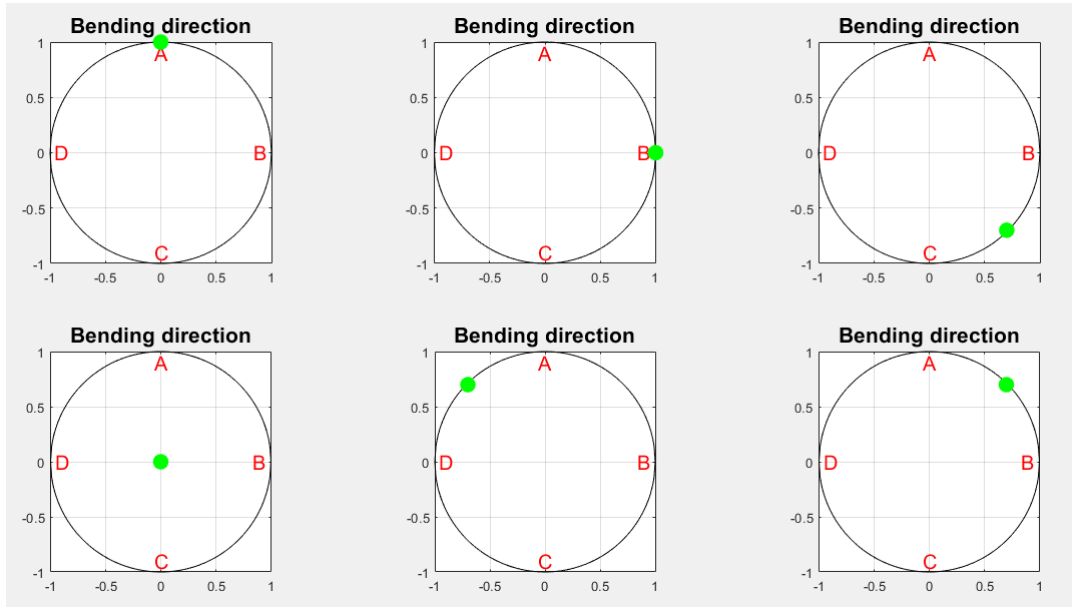


Figure 8.8: Graphic representation of sensor movement in different instants of time.

8.4 Graphic representation of sensor movement

In reality, the sensor curvature information provided by its four gratings is redundant.

The four gratings are arranged in pairs on opposite faces of the substrate and, for this reason, each pair detects an equal, but opposite bending in direction.

This redundancy of information is intentional because it allows a further distinction to be made between effects due to a change in curvature and those due to a change in torsion or temperature.

In order to demonstrate the actual redundancy of the information, a Matlab code was realised that allows the movement of the sensor to be tracked using only two of the sensor gratings, assuming they are placed on two adjacent faces of the substrate.

Again, direct communication between the Micron Optics HYPERION si155 optical interrogator and the Matlab software is used to acquire the Bragg wavelengths of the sensor gratings in real-time. The wavelength of the grating on face A and the wavelength of the grating on face B are respectively represented on the x-axis and y-axis of a Cartesian plane.

The code was tested while the sensor was moved following the profile of some simple

geometric figures. Fig. 8.9 shows an example of the graph obtained at the end of a test in which the sensor was moved by following the profile of a circumference in the air.

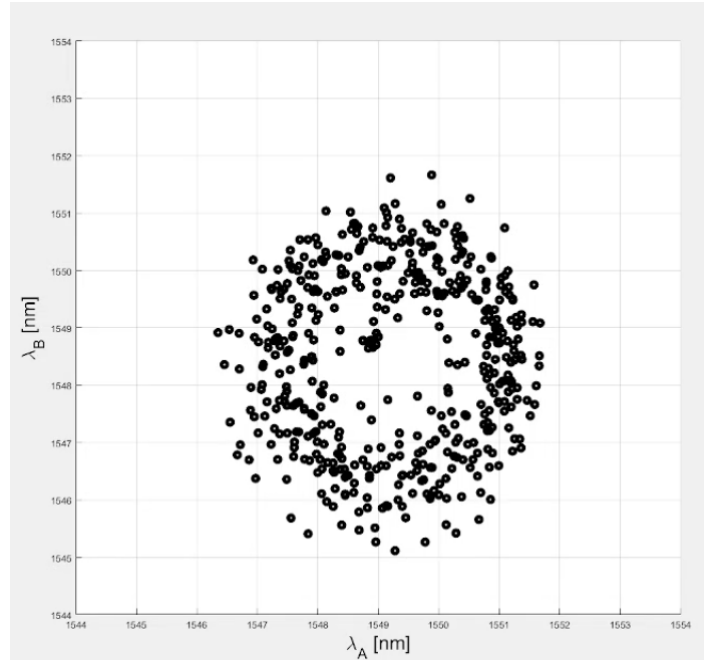


Figure 8.9: The graph obtained by moving the sensor along the profile of a circle in the air.

The resulting graph provides a first approximation of the movement of the sensor during acquisition. By carefully characterising the sensor, a more accurate representation can be obtained.

Chapter 9

Conclusions

This thesis is aimed at the development of a laser lipolysis applicator that, in addition to supplying the energy required for the operation, is able to detect the temperature at the source level. Temperature monitoring allows the physician to have more accurate control of the operation, optimising the results and reducing the risk of burning tissue.

The solution examined in this thesis involves integrating the laser source with FBG sensors. The use of such sensors in minimally invasive thermal therapies is widespread due to their small size, flexibility and lack of artefacts due to interaction with the laser beam. In FBG sensors, however, the wavelength variation depends on both temperature and strain. This characteristic becomes problematic in the application under consideration. During laser lipolysis, in fact, the continuous movement of the laser applicator causes an error in the reading of the built-in FBG sensors. The aim of this thesis is to compensate for this error. The method underlying the analyses conducted involves the realisation of an FBG sensor configuration that allows discrimination of the effects of temperature and strain.

The studies conducted in this thesis begin with the analysis of the two-dimensional case, where the FBG sensors are subject to bending strain only. In order to discriminate the effect of temperature from that of bending strain, two FBG sensors are sufficient.

Initially, these sensors were characterised. From the temperature characterisation of the two FBG sensors, sensitivity values, k_T , consistent with those reported in the literature were obtained. The sensitivities obtained for the two sensors are $11.400 \text{ pm } ^\circ\text{C}^{-1}$ and $11.234 \text{ pm } ^\circ\text{C}^{-1}$. To characterise the sensors with respect to bending strain, a calibration board was fabricated from a series of bending grooves with different curvatures. During these characterisation tests, the wavelength

variation of the gratings increased as the curvature to which they were subjected increased, as expected. However, the sensitivity obtained at the end of the characterisation was about an order of magnitude lower than that reported in the literature. These results suggest the possible presence of external factors leading to a different sensor deformation than expected.

To know with greater certainty the deformation to which the sensors are subjected, the two gratings were pasted to opposite sides of a miniaturised cantilever. In this way, when the cantilever is bent, the gratings are forced to move coherently. Once realised, the system was subjected to characterisation. The sensitivity values, k_s , obtained from the characterisation with respect to bending strain are $1.830 \text{ pm } \mu\epsilon^{-1}$ and $1.368 \text{ pm } \mu\epsilon^{-1}$. The congruence of these results with those found in the literature highlights the effectiveness of the new system in ensuring that the two gratings only perceive the strain experienced by the two faces of the cantilever.

Subsequently, the system was also subjected to a temperature characterisation inside a climatic chamber. The temperature sensitivity values obtained from this characterisation were higher than those obtained in the characterisation of the individual gratings. This difference is presumably attributable to the use of resin to bond the optical fibres to the cantilever.

The parameters obtained from the characterisations were used to develop a Matlab code that manages the sensor and makes it possible to distinguish between temperature and strain readings. The resulting system was tested under varying temperature and constant bending conditions. In order to verify the accuracy of temperature monitoring, a thermocouple was used as a reference sensor during the test. From the comparative analysis between the two measurements, it was observed that the temperature profile detected by the developed sensor follows the trend of that of the reference sensor. However, it has an offset error that causes an overestimation of the temperature by a few degrees.

In the last part of this thesis, the analysis of the three-dimensional case was undertaken. After various prototyping attempts, a new sensor was developed that simulates the shape of a laser cannula. This sensor consists of four FBG sensors pasted, using Norland Optical Adhesive 68 resin, to a substrate with a square section of 3 mm side.

Subsequently, the sensor was tested to assess its sensitivity to bending. The test results showed that each of the four FBG sensors is affected by the same bending strain experienced by the face of the substrate to which it is glued. At this point, a Matlab code was created that, based on the bending strain perceived by the gratings, provides an approximate graph of the sensor movement. Finally, this code was tested and validated during tests where the sensor was moved following

the profile of some elementary geometric figures.

The sensor is capable of correctly tracking movement, however, accurate characterisation would allow for more reliable results and greater accuracy in the graphical representation of movement.

The ultimate purpose of the sensor remains to correctly monitor temperature. The choice of a configuration with four FBG sensors is necessary for correct discrimination between temperature and strain in three-dimensional space. In this thesis, initial evaluations were conducted on the effect of bending strain on the sensor. However, a complete characterisation of the sensor with respect to bending strain, torsion strain and temperature is necessary to achieve the final goal.

The characteristic parameters obtained from these characterisation will allow for the correction of errors caused by deformation in the sensor readings, thereby enabling accurate temperature monitoring.

Once the sensor has been validated, it can be miniaturised. This could be achieved by replicating the same configuration of the four FBG sensors on a substrate of the same size as the laser lipolysis cannula. An alternative to be considered could be the use of a multicore fibre where a grating is inscribed in each individual core within the same section.

Further analysis could be conducted by simulating the movement of the laser cannula within ex-vivo tissue using the sensor to verify its proper functionality.

Bibliography

- [1] URL: <https://my.clevelandclinic.org/health/treatments/21525-body-countouring> (cit. on p. 1).
- [2] Matija Milanic, Blaz Tasic Muc, Matija Jezersek, and Matjaz Lukac. «Experimental and numerical assessment of hyperthermic laser lipolysis with 1,064nm Nd:YAG laser on a porcine fatty tissue model». In: *Lasers in Surgery and Medicine* 50.2 (2018), pp. 125–136. DOI: <https://doi.org/10.1002/lsm.22743> (cit. on pp. 1, 4).
- [3] URL: <https://www.who.int/news/item/04-03-2022-world-obesity-day-2022-accelerating-action-to-stop-obesity> (cit. on p. 1).
- [4] URL: <https://www.epicentro.iss.it/obesita/report-obesita-oms-2022> (cit. on p. 1).
- [5] Hannah Ritchie and Max Roser. «Obesity». In: *Our World in Data* (2017). <https://ourworldindata.org/obesity> (cit. on pp. 1, 2).
- [6] URL: <https://www.humanitas.it/news/obesita-quando-si-puo-ricorrere-a-un-intervento-di-chirurgia-bariatrica/> (cit. on p. 2).
- [7] Saleh M. Aldaqal, Ahmad Mohammad Makhdoum, Ali M. Turki, Basim A. Awan, Osama A. Samargandi, and Hytham Jamjom. «Post-bariatric surgery satisfaction and body-contouring consideration after massive weight loss». In: *North American Journal of Medical Sciences* 5 (4 Apr. 2013), pp. 301–305. ISSN: 22501541. DOI: 10.4103/1947-2714.110442 (cit. on p. 2).
- [8] Serge Mordon and Eric Plot. *Laser lipolysis versus traditional liposuction for fat removal*. 2009. DOI: 10.1586/erd.09.50 (cit. on pp. 4, 9, 15).
- [9] Oriete Gerin Leite Sandra Tagliolatto Vanessa Barcellos Medeiros. «Laser-lipolysis: update and literaturereview». In: (2012) (cit. on pp. 4–7).
- [10] MD Jason C. McBean MD; Bruce E. Katz. «Laser Lipolysis: An Update». In: (2011) (cit. on pp. 5, 7).

- [11] Bin Chen, Yue Zhang, and Dong Li. «Numerical Investigation of the Thermal Response to Skin Tissue during Laser Lipolysis». In: *Journal of Thermal Science* 27 (5 Oct. 2018), pp. 470–478. ISSN: 1993033X. DOI: 10.1007/s11630-018-1042-z (cit. on p. 6).
- [12] Riadh WY Habash, Rajeev Bansal, Daniel Krewski, and Hafid T Alhafid. «Thermal therapy, part 1: an introduction to thermal therapy». In: *Critical ReviewsTM in Biomedical Engineering* 34.6 (2006) (cit. on p. 8).
- [13] Daniel Mazzoni, Matthew J. Lin, Danielle P. Dubin, and Hooman Khorasani. *Review of non-invasive body contouring devices for fat reduction, skin tightening and muscle definition*. Nov. 2019. DOI: 10.1111/ajd.13090 (cit. on pp. 10, 14).
- [14] Laura Schilling, Nazanin Saedi, and Robert Weiss. *SPECIAL TOPIC 1060 nm Diode Hyperthermic Laser Lipolysis: The Latest in Non-Invasive Body Contouring*. 2017 (cit. on p. 11).
- [15] Kristel D. Polder and Suzanne Bruce. *Radiofrequency: Thermage*. May 2011. DOI: 10.1016/j.fsc.2011.04.006 (cit. on pp. 11, 12).
- [16] Lindsay R Sklar, Abdel Kader El Tal, and Leonard Y Kerwin. «Use of transcutaneous ultrasound for lipolysis and skin tightening: a review». In: *Aesthetic plastic surgery* 38.2 (Apr. 2014), pp. 429–441. ISSN: 0364-216X. DOI: 10.1007/s00266-014-0286-6. URL: <https://doi.org/10.1007/s00266-014-0286-6> (cit. on pp. 12, 13).
- [17] Paola Saccomandi, Emiliano Schena, and Sergio Silvestri. *Techniques for temperature monitoring during laser-induced thermotherapy: An overview*. 2013. DOI: 10.3109/02656736.2013.832411 (cit. on pp. 16–18, 21, 22).
- [18] URL: <https://www.sensoriditemperatura.it/la-termoresistenza/> (cit. on p. 19).
- [19] Ginu Rajan, B Gangadhara Prusty, and Krzysztof Iniewski. «Structural Health Monitoring of Composite Structures Using Fiber Optic Methods Introduction to Optical Fiber Sensors». In: (). DOI: 10.1201/9781315369815-4. URL: <https://www.routledgehandbooks.com/doi/10.1201/9781315369815-4> (cit. on p. 19).
- [20] Emiliano Schena, Daniele Tosi, Paola Saccomandi, Elfed Lewis, and Taesung Kim. *Fiber optic sensors for temperature monitoring during thermal treatments: An overview*. July 2016. DOI: 10.3390/s16071144 (cit. on pp. 20, 21).
- [21] Éric Pinet, Sébastien Ellyson, and F. Borne. «TEMPERATURE FIBER-OPTIC POINT SENSORS: COMMERCIAL TECHNOLOGIES AND INDUSTRIAL APPLICATIONS». In: 2010 (cit. on pp. 22, 23).

- [22] URL: <https://www.comefunziona.net/arg/fibraottica/3/> (cit. on p. 25).
- [23] URL: <http://sites.science.oregonstate.edu/~hadlekat/COURSES/ph212/rayOptics/snell-s-law.html> (cit. on p. 26).
- [24] URL: https://www.photonics.com/Articles/Fiber_Optics_Understanding_the_Basics/a25151 (cit. on pp. 26, 27).
- [25] Govind P. Agrawal. *Multimode fibers*. 2019. DOI: 10.1016/b978-0-12-817042-7.00021-x (cit. on p. 28).
- [26] Andreas Othonos, Kyriacos Kalli, David Pureur, and Alain Mugnier. «Fibre Bragg gratings». In: *Springer Series in Optical Sciences* 123 (2006), pp. 189–269. ISSN: 03424111. DOI: 10.1007/3-540-31770-8_6 (cit. on pp. 29, 59, 77, 83).
- [27] Alexandr V. Dostovalov, Alexey A. Wolf, Mikhail I. Skvortsov, Sofia R. Abdullina, Aleksey G. Kuznetsov, Sergey I. Kablukov, and Sergey A. Babin. «Femtosecond-pulse inscribed FBGs for mode selection in multimode fiber lasers». In: *Optical Fiber Technology* 52 (2019), p. 101988. ISSN: 1068-5200. DOI: <https://doi.org/10.1016/j.yofte.2019.101988>. URL: <https://www.sciencedirect.com/science/article/pii/S1068520019301932> (cit. on p. 30).
- [28] URL: https://www.ushio.co.jp/en/feature/functional_device/trust/interference_lithography.html (cit. on p. 31).
- [29] URL: https://www.wikiwand.com/en/Fiber_Bragg_grating#Media/File:Fbg4.GIF (cit. on p. 32).
- [30] Virginia Sampognaro. *Caratterizzazione e applicazioni di sensori con reticoli di Bragg per applicazioni biomedicali = Characterization and applications of fiber Bragg grating sensors for biomedical applications*. Tesi di laurea. 2022 (cit. on p. 34).
- [31] *Optical Sensing Instrumentation and Software*. 2017. URL: www.micronoptics.com (cit. on p. 36).
- [32] URL: <http://my3dconcepts.com/explore/main-components-of-desktop-3d-printers/> (cit. on pp. 37, 39).
- [33] «MOT025-MEGA X-English-20191218-V0.0.5». In: () (cit. on p. 38).
- [34] Yinggang Liu, Yanpei Feng, Junliang Wen, Liang Huang, and Jingfei Dong. In: *Optical Fiber Technology* 75 (Jan. 2023). ISSN: 10685200. DOI: 10.1016/j.yofte.2022.103197 (cit. on p. 41).

- [35] Kenneth K.C. Lee, Adrian Mariampillai, Moez Haque, Beau A. Standish, Victor X.D. Yang, and Peter R. Herman. «Temperature-compensated fiber-optic 3D shape sensor based on femtosecond laser direct-written Bragg grating waveguides». In: *Optics Express* 21 (20 Oct. 2013), p. 24076. ISSN: 10944087. DOI: 10.1364/oe.21.024076 (cit. on p. 43).
- [36] Jason R. Grenier, Luís A. Fernandes, Paulo V. S. Marques, J. Stewart. Aitchison, and Peter R. Herman. «Optical circuits in fiber cladding: Femtosecond laser-written Bragg Grating Waveguides». In: *CLEO: 2011 - Laser Science to Photonic Applications*. 2011, pp. 1–2. DOI: 10.1364/CLEO_SI.2011.CMZ1 (cit. on p. 44).
- [37] Xinhua Yi, Xiangyan Chen, Hongchao Fan, Fei Shi, Xiaomin Cheng, and Jinwu Qian. «Separation method of bending and torsion in shape sensing based on FBG sensors array». In: *Opt. Express* 28.7 (Mar. 2020), pp. 9367–9383. DOI: 10.1364/OE.386738. URL: <https://opg.optica.org/oe/abstract.cfm?URI=oe-28-7-9367> (cit. on p. 45).
- [38] Jincong Yi, Xiaojin Zhu, Hesheng Zhang, Linyong Shen, and Xiaoping Qiao. «Spatial shape reconstruction using orthogonal fiber Bragg grating sensor array». In: vol. 22. Elsevier Ltd, 2012, pp. 679–687. DOI: 10.1016/j.mechatronics.2011.10.005 (cit. on pp. 50, 51).
- [39] K. T. V. Grattan and B. T. Meggitt. *Optical fiber sensor technology*. Chapman Hall, 1995, p. 499. ISBN: 0412782901 (cit. on p. 84).